

DISSERTATION TEMPLATE FOR PRINCETON UNIVERSITY

WENJIE LEI

A DISSERTATION
PRESENTED TO THE FACULTY
OF PRINCETON UNIVERSITY
IN CANDIDACY FOR THE DEGREE
OF DOCTOR OF PHILOSOPHY

RECOMMENDED FOR ACCEPTANCE
BY THE DEPARTMENT OF
GEOSCIENCES
ADVISER: PROFESSOR JEROEN TROMP

FEB 2019

© Copyright by Wenjie Lei, 2019.

All rights reserved.

Abstract

Using GLAD-M15 as our starting model, we conducted 10 quasi-Newton iterations to bring the second generation model, GLAD-M25. It pushes the resolution of global model to 17s and the number of earthquakes to 1,480. To achieve such goals, we work from several aspects to overcome computational challenges. The Adaptable Seismic Data format, was designed to store the seismic data, to meet the requirements and standards of modern data containers. GPU acceleration is introduced in the solver to facilitate the forward and adjoint simulations. Workflow management tools were used to help us automate the inversion workflow, reducing human interference and speed up the iterations. To balance the uneven distribution of earthquakes and seismic stations, we introduced the geographical weightings to be applied to construction of misfit functions and facilitate the convergence rate. Our model was evaluated in various ways, including the misfit and histogram. We also used 360 earthquakes as held-out data, to assess the quality of our new model. All the above showed our model has significant improvements over the starting model. Our model is also demonstrated and compared with various global and regional models. We observed notable features in our model, in Europe, Asia, North America and South America. The comparison shows our model reaches unprecedented resolution for models at global scale, reaching similar resolution to regional and continental ones at upper mantle. Our model also shows prominent features in plumes and subduction zones, resolving deep structure in great details. We believe such improvements in the interior of the Earth could provide us new insights into the dynamics and evolution of the Earth.

Acknowledgements

I want to first give thanks to my advisor, Jeroen Tromp. It is one of my best experience to work with him for the past six years. The more I worked with him, the more I realized he is such a talented, knowledgeable and easy-going person. He is also willing to help his students anytime. Whenever I got a question, I just go and knock his door. He will do his best to help me. If it is a questions related to my research, he would go from the very basic to explain my questions in very details. There are times when we have difficulties and chanllenges during the past six years. Jeroen is also has a personality to encourage us and go back to the right track. He has a great vision and always dedicated to achieve the goal, and he is willing to share his optimisum and courage with others.

I also want to give thanks to my committee members: Allan Rubin, Frederik Simons and Jessica Irving. They provide me a lot of help during my generals and let me pass it saftely. In my global projects, they also provide my numerous suggestions and insights that help me to better undetstand the model and create new ideas.

I would like to acknowledge my colleagues in seismology group: Hom Nath Gharti, Matthieu Levebfre, James Smith, Ryan Modrak, Yanhua Yuan, Uno B. Vaaland, David Luet... Hom Nath Gharti has been my office mate since four years ago. He is such a knowledgable and friendly person. It was my best memories to stay at Room 309 and I feel that is my "home". It is hard to image if we didn't have Matthieu in our group for the past six years. I learned so much technique knowledge from him . He is always the first person I could go to ask for help if I had a technique problem. It is also great to work with James Smith and Ryan Modrak on the same global projects and many associated sub-projects. They are the person I can always rely on.

I would also like to take this chance to acknowledge all previous members in our group: Ebru Bozdag, Hejun Zhu, Qinya Liu, Min Chen, Carl Tape, Dimitri Komatitsch Daniel Peter...Their work built the foundation of adjoint tomography

workflow. I also want to give special thanks to Ebru, Hejun and Min. They provided me with their models, so I can compare my models with theirs. I also had numerous discussion with them in AGU and other occassions, which provide me with new insights into our model and bring the GLAD-M25 to final fruition. Just before the submission of our GLAD-M25 model, I was shocked to hear that Dimitri Komatitsch passed away unexpectedly. He is a computational geophysicist extraordinaire who built the family of SPECFEM software together with Jeroen.

I want to thank students and friends in the Geoscience departments: Yajun Peng, Wenbo Wu, Pathikrit Bhattacharya, Farhan Nuruzzaman, Cara Magnabosco. It is always joyful to talk with you. I gave my best wishes to our administrative assistants: Mary Rose Russo, Sheryl Robas. It is their work and efforts to make it possible for us to focus on research.

I want to thank my former advisor at USTC, Xiaofei Chen. I did a summer project with him and it is him who introduced me into geophysics. From him and Jeroen, I feel their passion and dedication to geophyscis research. They are my role models in my future career.

I give final thanks to my parent, Jinfu Lei and Shenglan Lou, and my girlfriend Qizhi Xu. It is your support, love and care that make my life so meaningful and joyful, and make me become who I am today.

To my parents.

Contents

Abstract	iii
Acknowledgements	iv
List of Tables	xi
List of Figures	xii
1 Introduction	1
2 An Adaptable Seismic Data Format	3
2.1 Summary	3
2.2 Introduction	4
2.2.1 Motivation	4
2.2.2 Scope	6
2.2.3 Benefits	7
2.3 Overview of the Format	9
2.3.1 Container	10
2.3.2 Seismic Event Information	11
2.3.3 Waveforms and Station Meta Information	12
2.3.4 Auxiliary Data	14
2.3.5 Provenance	15
2.3.6 Data Relations	17
2.4 Comparison to Existing Formats	18

2.4.1	MiniSEED	18
2.4.2	SAC	19
2.4.3	SEG Y and PH5	20
2.5	Implementations	21
2.6	Demonstrations and Use Cases	21
2.6.1	Dataset Building	22
2.6.2	Storage, Exchange, and Archival of Processed or Synthetic Waveforms	22
2.6.3	(Parallel) Large Scale Data Processing	23
2.6.4	Active Source Industry Dataset	24
2.6.5	Further Uses	24
2.7	Conclusions and Future Directions	25
3	Data & Workflow Management for Exascale Global Adjoint Tomog- raphy	29
3.1	Introduction	29
3.2	Scientific Methodology	31
3.3	Solver: SPECFEM3D_GLOBE	34
3.3.1	Overview and programming approach	34
3.3.2	Scalability and Benchmarking results	36
3.4	Optimizing I/O for computational data	40
3.4.1	Parallel file formats and I/O libraries for scientific computing .	41
3.4.2	Integrating parallel I/O in adjoint-based seismic workflows .	44
3.5	A Modern Approach to Seismic Data: Efficiency and Reproducibility	45
3.5.1	Legacy	46
3.5.2	The Adaptable Seismic Data Format	48
3.5.3	Data Processing	50
3.6	Bringing the Pieces Together: Workflow Management	52

3.6.1	Existing solutions	53
3.6.2	Adjoint tomography workflow management	55
3.6.3	Moving toward fully managed workflows	57
3.6.4	Additional challenges	58
3.7	Software Practices	59
3.8	Conclusion	62
4	Balancing Unevenly Distributed Data in Seismic Tomography: A Global Adjoint Tomography Example	77
4.1	summary	77
4.2	summary	78
4.3	Introduction	78
4.4	Weighting strategy	80
4.4.1	Measurements and Misfit Function	80
4.4.2	Category-weighting strategy	81
4.4.3	Geographical-weighting strategy	84
4.5	Numerical Validation: 2D Global Adjoint Tomography	90
4.6	Application to 3D Global Adjoint Tomography: Misfit Statistics	93
4.7	Conclusion	99
5	Global Adjoint Tomography – Model GLAD-M25	101
5.1	Summary	101
5.2	Introduction	102
5.3	Starting model GLAD-M15	105
5.4	Earthquakes	105
5.5	Seismic data	109
5.5.1	Adaptable Seismic Data Format	109
5.6	Misfit function	111

5.7	Model parameterization	113
5.8	Adjoint tomography workflow	114
5.8.1	Forward simulations	114
5.8.2	Seismic data processing	116
5.8.3	Adjoint Simulations	119
5.8.4	Postprocessing	121
5.8.5	Workflow management	122
5.9	Misfit evolution	122
5.9.1	Stage I: Iterations 15–17	122
5.9.2	Stage II: Iterations 18–21	124
5.9.3	Stage III: Iterations 22–25	124
5.9.4	Misfit assessment	124
5.9.5	Histogram comparisons	125
5.10	Model evaluation	127
5.10.1	Point-spread function analysis	127
5.10.2	Held-out data set	128
5.11	Model GLAD-M25	131
5.11.1	Global structure	131
5.11.2	Plumes	143
5.11.3	Subduction zones	145
5.12	Discussion	147
5.13	Conclusion	149
A	Spherically symmetric average model	152
B	Spherical harmonic model expansion	155
	Bibliography	160

List of Tables

4.1 Measurement categories in global adjoint tomography [12, 67]. Seismic waves are categorized in terms of complementary period bands on three components of motion.	81
5.1 Changes in fit in the twelve measurement categories between the new model, GLAD-M25, and its starting model, GLAD-M15, and, in parentheses, between GLAD-M25 and model S362ANI combined with CRUST2.0, which was the starting model for the GLAD-M15 inversion.	125
5.2 Changes in fit for 360 earthquakes not used in the inversion in the twelve measurement categories between the new model, GLAD-M25, and its starting model, GLAD-M15, and, in parentheses, between GLAD-M25 and model S362ANI combined with CRUST2.0, which was the starting model for the GLAD-M15 inversion.	129

List of Figures

- 2.1 The general structure of an ASDF file in its HDF5 container — it has four distinct parts: (1, yellow) Information about an arbitrary number of earthquakes (or other seismic events) is stored in a single QuakeML document, the most complete earthquake description format currently available. (2, green) Seismic waveforms are stored per station together with the necessary meta information in the form of an FDSN StationXML document. (3, red) Anything that cannot be regarded as a seismic waveform is hierarchically stored in the auxiliary data section. (4, blue) Provenance information is stored as a number of SEIS-PROV documents, an extension to W3C PROV. Background colors in the attributes (rectangular boxes) denote relations to other sections in an ASDF file. Examples of this are relations of a waveform to a certain event or a provenance record for a piece of auxiliary data. . . . 26

2.2 Simple example to illustrate the key concepts of storing provenance information with SEIS-PROV and W3C PROV. It describes a single waveform trace that has been lowpass filtered to create a filtered waveform trace. The arrows in this graphical representation mostly point backwards in the process towards the origin of something. The yellow ellipses are called entities, and here they represent a waveform trace at two different points in time. The blue rectangle is an activity that can use and generate entities. It denotes a lowpass filter and uses the first waveform trace to generate a new, filtered waveform trace. The orange house shape symbolizes an agent who is responsible for something. In this case it stands for the software that performed the filtering operation. Finally, the white rectangles are attributes with more details about any node. Please note that this figure shows only one possible graphical representation of the underlying data model and more or less detailed ones can be employed as appropriate.

27

2.3 Compression efficiency of the ASDF format using algorithms available in HDF5 for a number of typical seismological datasets. Please keep in mind that the efficiency and I/O speed of these algorithms are heavily dependent on the actual data and hardware, and thus your mileage may vary. The columns represent the file size relative to the uncompressed case, the numbers inside are the achieved compression ratios. The small boxes above the columns denote the relative writing duration in red and the relative reading duration in green compared to the uncompressed case. The left plot shows the efficiency for a dataset containing 500 StationXML documents adding up to 120 MiB. I/O speed differences are irrelevant as the cost for parsing and generation of the XML documents is constant and dominates the total run time. The middle plot shows the compression efficiency for a bandpass filtered waveform dataset stored as 32-bit floating point numbers. It consists of 3,466 waveform traces taking up 282 MiB on disk. The red bar compares it to the uncompressed SAC format. The rightmost plot shows the efficiency for storing 3,346 raw waveform files stored as 32-bit integers taking up 2,340 MiB. The red bars here show the efficiency for the same dataset of the STEIM1 and STEIM2 special purpose compression algorithms defined for the SEED format measured by writing them as MiniSEED files. 28

3.1 General adjoint tomography workflow. The focus is on the data involved in each step. Seismic data are depicted by red boxes and for each of the N_s seismic events they are recorded by N_{sr} receivers. Computational data are represented by green and blue boxes. The amount of elementary data varies depending on the workflow stage and can eventually be grouped into a smaller number of files. 65

3.2 Strong scaling for the spherically symmetric PREM Earth model on Titan for a minimum seismic period of 9 s. The mesh is comprised of $\sim 1.667 \times 10^8$ million elements for this resolution. Values are plotted against the number of MPI processes.	66
3.3 Weak scaling for the PREM Earth model on Titan. Performance is measured as the averaged mean time for each time step. The same work load is applied to each MPI process in different cases.	67
3.4 Strong scaling for the PREM Earth model on Titan for a minimum seismic period of 27 s with full attenuation. Values are plotted against the number of MPI processes.	68
3.5 Strong scaling for the PREM model on Titan for a minimum seismic period of 27 s in the case of without <i>full attenuation</i> . Values are plotted against the number of MPI processes.	69
3.6 Strong scaling for the PREM model on Titan for a minimum seismic period of 17 s in the case of with <i>full attenuation</i> . Values are plotted against the number of MPI processes.	70
3.7 Strong scaling for the PREM model on Titan for a minimum seismic period of 17 s in the case of without <i>full attenuation</i> . Values are plotted against the number of MPI processes.	71
3.8 Strong scaling for the PREM model on Titan for a minimum seismic period of 9 s in the case of without <i>full attenuation</i> . Values are plotted against the number of MPI processes.	72

3.9 I/O pattern with full attenuation. The forward simulation (left bar) produces snapshots at regular intervals. During the kernel simulation (right bars) these snapshots are read in reverse order to piece-wise reconstruct the forward wavefield for a number of time steps. The interaction of this reconstructed wavefield with the adjoint wavefield yields to the so-called event kernels, the sum of which is the misfit gradient. Solid arrows depict computation order, dashed arrows represent I/O. Bars shade from black to light gray jointly with forward time.	73
3.10 Layout of the Adaptable Seismic Data Format, including earthquake event information, waveforms and station meta information, auxiliary data and provenance. In such layout, different types of data are grouped into one file and ready for later retrieval.	74
3.11 Workflow of seismic data processing using ASDF. First, time series analysis is applied to raw observed and synthetic data to ensure a comparable spectral content at a later stage. Then, time windows are selected for pairs of processed observed and synthetic data, inside which measurement are made. Finally, adjoint sources are generated as the final pre-processing output. ASDF speeds up these tasks by using parallel processing (MPI). For each step, processing information is added to the provenance.	75

3.12 Steering process of the workflow management system. Two objects (DB manager and Job Manager) serve as an interface between the database and the workflow engine. The job manager requests data from the DB manager (1), which polls an SQLite database (2). Once the request is served (3), executables, parameters, and inputs are formatted (4) to feed the workflow engine (5). The workflow engine transparently launches the job and monitors its status, which is then returned (6). The status is used to update the database (7, 8) in order to keep track of the inversion status. This process is repeated (9), until everything has been processed.	76
4.1 Condition number of the diagonal weighting matrix defined by eqn. (5.2) as a function of the reference distance Δ_0 . The chosen value, indicated by the green star, is about one third of the largest possible value. Since evaluation of eqn. (5.2) for different reference distances adds negligible computational expense, it is possible (and recommended) to repeat this type of analysis for each iteration.	87
4.2 Example of receiver weights for an event C201604131355A at 40–100 s period band and vertical component determined based upon eqn. (5.2), and normalized according to eqn. (4.25). The weights are in logarithmic scale. Note the difference between USArray stations and ocean island stations. . .	88
4.3 Example of source weights determined based upon eqn. (5.2), and normalized according to eqn. (4.24). Note the difference between dense subduction zone earthquakes and sparse transform fault earthquakes.	88
4.4 Source-receiver geometry used in synthetic inversions. GSN stations are labeled by green triangles, USArray stations by blue triangles, and sources by magenta asterisks.	91

4.5	Target model used in the synthetic inversions. Wavespeeds are determined by the 40 s Rayleigh wave phase speed model of [131].	91
4.6	With the category weighting defined in Section 4.4.2, convergence is extremely slow. With the geographical weighting discussed in Section 4.4.3, convergence is much faster. Diagonal model-space preconditioning, it turns out, is not an effective alternative to weighting when dealing with extremely lopsided source-receivers distributions.	92
4.7	Percentage of data (window count) in each of the twelve categories (see Table 4.1). Period band and wave type are labeled in the upper right corner of each panel. Note the dramatic differences between body-wave (top) and surface-wave data (bottom). The large variations in data count from category to category illustrate the need for balancing.	93
4.8	Percentage of the misfit in each of the twelve categories (see Table 4.1) using the category-weighting strategy (orange), and geographical-weighting strategy (black). The percentage contribution in each category is labeled above the bars. Note that each category's contribution to the misfit barely changes with geographical weighting, because weight re-balancing only happens within each category.	94
4.9	Percentage of the misfit of GSN stations (II, IU) and USArray stations (TA) in each category using category-weighting (left wedges in each panel) and geographical-weighting strategies (right wedges in panel). Compared with the category-weighting strategy, the geographical-weighting strategy assigns more weight to GSN stations and down weights USArray stations in all categories.	96

4.10	Smoothed gradient contributions using data from 42 earthquakes without (Left Column) and with source & receiver weighting (Right Column) in three period bands: 17–40 s (Top Row), 40–100 s (Middle Row), and 90–250 s (Bottom Row). The top center map shows the cross section with red line for reference. The isotropic smoothing length scale is 100 km.	98
4.11	Example of a smoothed misfit gradient (weighted summation of the contributions of the three period bands shown in Fig. 4.10) using data from 42 earthquakes without (Left) and with source & receiver weighting (Right). The isotropic smoothing length scale is 100 km.	99
5.1	Source corrections for 1,040 out of 1,480 events used in the structural inversion. (a) Map view of depth changes. (b) Distribution of seismographic stations used for source inversions. (c) Depth change relative to the original global CMT Catalog depth. (d)–(f) Histograms of depth, origin time, and scalar moment changes relative to the CMT Catalog.	106
5.2	The 1,480 earthquakes used in this study. (a) Distribution of earthquakes. The color of each beach ball reflects its depth range, where blue designates events shallower than 50 km, green events between 50 km and 300 km, and red events deeper than 300 km. (b) & (c) Histograms of earthquake moment magnitudes and depths.	109
5.3	Distribution of the 11,800 seismographic stations used in this study. Colors denote the number of events for which a given station contributes waveforms to the structural inversion. Stations with a number of event responses < 400 are plotted in smaller size; these are usually temporary arrays deployed over a short period of time, frequently ocean bottom seismometers. The maximum number of event responses comes from ANMO, in Albuquerque, New Mexico, which contributed to 1,442 out of 1,480 earthquakes in the data set.	110

5.4	Adjoint tomography workflow.	115
5.5	Sub-workflow workflow for preprocessing seismic data.	116
5.6	Time-distance plot for vertical component 17–40 s body waves showing a measurement window density map. A total of 4,363,719 time windows were discretized into 1 degree epicentral distance and 1 s time bins. The maximum window count is 9,931 in the 85–86° distance and 1,375–1,376 sec time bin. Major traveltimes are labeled. Note that the plot contains data from events with a wide variety of depths, so the branches are for identification purposes only.	117
5.7	Same as Fig. 5.6, except for radial component 17–40 s body waves. A total of 2,868,252 time windows were discretized into 1 degree epicentral distance and 1 s time bins. The maximum window count is 7,542 in the 86–87° distance and 1,378–1,379 s time bin.	119
5.8	Same as Fig. 5.6, except for transverse component 17–40 s body waves. A total of 2,151,856 time windows were discretized into 1 degree epicentral distance and 1 s time bins. The maximum window count is 7,208 in the 89–90° distance and 1,398–1,399 s time bin. Only SH traveltimes are labeled.	120
5.9	Evolution of the misfit function from GLAD-M15 to GLAD-M25. Each color denotes different stages of the inversion, as discussed in Sections 5.9.1–5.9.3. (a) Evolution of the total misfit. (b)–(j) Misfit in each period band (rows) on three components (columns). (e)–(g) Since iteration 18, we split the 40–100 s period band into two measurement categories: body waves (diamonds) and surface waves (squares).	123

5.10 Histograms of phase measurements in all twelve measurement categories for S362ANI combined with CRUST2.0 (M00, Black), GLAD-M15 (M15, Green), and GLAD-M25 (M25, Red). Each column represents one component and each row corresponds to a period band. The numbers above the top right of each panel denote the number of measurements in the corresponding category. The total number of measurements is 18.2 million. The mean and standard deviations of the phase measurements for the three models are displayed in the top right corner of each panel.	126
5.11 Histograms of 17–40 s traveltimes anomalies of P (vertical and radial), and SH (Transverse) arrivals for models S362ANI combined with CRUST2.0 (M00, Black), GLAD-M15 (M15, Green), and GLAD-M25 (M25, Red).	127
5.12 Same as Fig. 5.10 except for amplitude measurements. These measurements are currently not used in the inversion.	128
5.13 Summary of the held-out database containing 360 earthquakes. Theses events were not used in the structural inversion. (a) Distribution of events color coded by depth range as in Fig. 5.2. (b) & (c) Histograms of moment magnitude and depth.	129
5.14 Same as Fig. 5.10, except for the held-out database.	130
5.15 Same as Fig. 5.11, except for the held-out database.	130
5.16 Map views of global shear wavespeed perturbations at various depths for model GLAD-M25 (left column), S362ANI+M(middle column) [91], and S40RTS(right column) [108]. At a given radius, perturbations are calculated relative to each model’s average. The range of perturbations in shear wavespeed varies from map to map, as indicated in the top left of each panel. The green circles denote locations of various hotspots [90]. The range of the colorbar is the same for each row, and its maximum value is indicated in parentheses on the left, after the depth.	132

5.17 Map views of global compressional wavespeed variations at various depths for model GLAD-M25 (left column), LLNL-G3Dv3(middle column)[119], and GAP-P4(right column) [41]. For LLNL-G3Dv3, depth ranges are labeled in the bottom right bottom of each panel. Other plotting conventions are as in Fig. 5.16.	134
5.18 Map views of isotropic shear wavespeed variations beneath North America for model GLAD-M25 (first column) and several global (S362ANI+M and S40RTS) and regional US22 [155] and SL2013NA [113] models. Green circles denote the locations of hotspots. For SL2013NA, we show a depth of 610 km instead of 600 km, reflecting its model parametrization.	135
5.19 Map views of isotropic shear wavespeed variations beneath Europe for model GLAD-M25 (first column), two global model (S362ANI+M and S40RTS), and one regional model EU60 [154]. For EU60, the range of the color bar is 4% at all depths, as indicated in the bottom right bottom of the panels. . .	138
5.20 Map views of shear wavespeed variations beneath Asia for GLAD-M25 (first column), global models S362ANI+M (second column) and SL2013sv (third column), and regional model EARA2014(last column) [20].	140
5.21 Map views of compressional wavespeed variations beneath South America for GLAD-M25 (first column) and global models S362ANI+M [91] (second column), LLNL-G3Dv3 [119] (third column), and GAP-P4 [41] (fourth column).	142

5.22 Vertical cross sections for various plumes for models GLAD-M25 (V_S ; left column), TX2015 [74] (center column), and SEMUCB-WM1 [38] (right column). The map in the top left corner of each row shows the cross section with color-coded red, green, and white dots for geographical reference; hotspots are denoted by red triangles. The dashed black semicircles in the cross sections denote depths of 410 km, 660 km, and 1000 km. (a) Afar; (b) Bermuda (left) and Canary (middle); (c) Cape Verde (middle) and Hoggar (right); (d) Iceland (middle) and Eifel (right); (e) Easter (left) and Galapagos (right); (f) Marion (middle), and Kerguelen (right).	143
5.23 Vertical cross sections of compressional wavespeed perturbations in various subduction zones for models GLAD-M25 (V_P ; left column), GAP-P4 [41] (middle column) and UU-P07 [139] (right column). The map in the top left corner of each row shows the cross section with color-coded red, green, and white dots for geographical reference. The dashed black semicircles in the cross sections denote depths of 410 km, 660 km, and 1000 km. (a) Aegean; (b) South America; (c) Hatteras; (d) Wichita. (e) Nepal; (f) Sunda. . . .	146
5.24 Normalized power per degree ℓ as a function of radius, based on Eqn. (B.17), for models S362ANI (left), GLAD-M15 (middle), and GLAD-M25 (right). Shown are depths greater than 120 km. (Courtesy of Caio Ciardelli.) . . .	151
A.1 1D radial shear and compressional wavespeed profiles for GLAD-M25, STW105, and PREM. The reference frequency for physical dispersion is 7.77 mHz.	154
A.2 1D radial-anisotropic shear and compressional wavespeed profiles for GLAD-M25 and STW105. The reference frequency for physical dispersion is 7.77 mHz.	154

B.1 Normalized power per degree ℓ , based on Eqn. (B.16), for models S362ANI (red), GLAD-M15 (green), and GLAD-M25 (blue). The calculation in- cludes depths greater than 120 km. Model S362ANI has no power beyond degree 18, and model S40RTS has no power beyond degree 40. (Courtesy of Caio Ciardelli.)	159
---	-----

Chapter 1

Introduction

Construction of global tomographic models of the Earth dates back to the late 1970s and early 1980s. However, due to the computational challenges, it took more than 20 years for the first adjoint-state models to be applied and shown successes to regional and continental scale studies. The first generation of global adjoint model, GLAD-M15, was published in 2016 using 253 earthquakes. During last 6 years, we have been working on extending the database and carry out the second generation of the global model. The new model, GLAD-M25, used 1,480 earthquakes, almost 6 fold of data compared last generation and ten quasi-Newton iterations starting from GLAD-15. We believe the new model could provide researchers with new insights into the interior and dynamics of the Earth.

To carry out iterations with such a large database and high demands for numerical computations, there are several technique challenges we solved to achieve our goals. Chapter 2 presents the Adaptable Seismic Data Format(ASDF). We discuss the motivation to introduce a new modern data format, to host our seismic data. It was designed on the purpose to facilitate the efficiency, integrity, and reproducibility of seismic data that used in our inversion.

Chapter 3 gives a overview of the technique chanllenges we encountered in the workflow of adjoint tomography, and our solution to them. Our solver, SPECFEM3D GLOBE, takes the most expensive part of computation stages, forward and adjoint simulations. It is accellerated using MPI and GPU, showing the improvs by various benchmark tests. We also covered I/O problems, for both mesher data and seismic data, by introductin ADIOS and ASDF to store different data. The last part is workflow integration and automazition, using workflow management systems.

Chapter 4 discussed the weightings we introduced in the tomography, to balance the uneven distribution of earthquakes and seicmic stations. We begun by demonstrating a few current used weighting methods and point them drawbacks. We future presented our simple-designed and robust weighting strategies. We conclude by conducting a 2D synthetic test, showing our weighting strategy can indeed improve the convergence rate of global-scale inversion.

Chapter 5 presented our second generation model, GLAD-M25. We went through the data and inverison strategy over iterations. The model was evaluated by various ways, including the misfit reduction and histogram change. 360 earthquakes were used as held-out data to future assess the quality of our model. We conclude by showing case the GLAD-M25 model, along with many regional and global models. The details and improvment on resolutions is unseen in other global models and we belive such improvements could help researchers to get an better understanding of the earth at a global scale.

Chapter 2

An Adaptable Seismic Data Format

Note

This chapter was submitted as a paper entitled "An adaptable seismic data format" by Krischer, L., Smith, J., Lei, W., Lefebvre, M., Ruan, Y., de Andrade, E.S., Podhorszki, N., Bozda, E. and Tromp, J. to *Geophysical Supplements to the Monthly Notices of the Royal Astronomical Society*, 2016.

2.1 Summary

We present ASDF, the Adaptable Seismic Data Format, a modern and practical data format for all branches of seismology and beyond. The growing volume of freely available data coupled with ever expanding computational power opens avenues to tackle larger and more complex problems. Current bottlenecks include inefficient resource usage and insufficient data organization. Properly scaling a problem requires the resolution of both these challenges, and existing data formats are no longer up to the task. ASDF stores any number of synthetic, processed, or unaltered waveforms in a single file. A key improvement compared to existing formats is the inclusion of com-

prehensive meta information, such as event or station information, in the same file. Additionally, it is also usable for any non-waveform data, for example, cross correlations, adjoint sources, or receiver functions. Last but not least, full provenance information can be stored alongside each item of data, thereby enhancing reproducibility and accountability. Any dataset in our proposed format is self-describing and can be readily exchanged with others, facilitating collaboration. The utilization of the HDF5 container format grants efficient and parallel I/O operations, integrated compression algorithms, and check sums to guard against data corruption. To not reinvent the wheel and to build upon past developments, we use existing standards like QuakeML, StationXML, W3C PROV, and HDF5 wherever feasible. Usability and tool support is crucial for any new format to gain acceptance. We developed mature C/Fortran and Python based APIs coupling ASDF to the widely used SPECFEM3D_GLOBE and ObsPy toolkits.

2.2 Introduction

2.2.1 Motivation

Seismology is, to a large extent, a science driven by observing, modeling, and understanding data. The process of making discoveries from data requires simple, robust, and fast processing and analysis tools, empowering seismologists to focus on actual science. Modern seismological workflows assimilate data on an unprecedented scale, and the need for efficient processing tools is pressing. In this context, the format in which data is stored and exchanged plays a central role. For example, passive seismic data are commonly stored in such a way that each time series corresponds to a single file on the file system. The amount of I/O required to process and assimilate data stored this way quickly becomes debilitating on modern HPC platforms. As another example, simulated seismograms depend on a large number of input parameters, par-

ticular versions of modeling software, and specific run-time execution commands. A modern data format should strive for complete reproducibility by keeping track of such data provenance. The majority of existing seismic data formats were created in a more primitive computing era, when no one could have foreseen the size, complexity, and challenges that seismological datasets must accommodate today. New seismological techniques, such as interferometry and adjoint tomography, require access to very large computers, where I/O poses a major bottleneck and data mining and feature extraction are challenging.

In this article we introduce a new data format —the Adaptable Seismic Data Format (ASDF)— designed to meet these challenges. We are fully aware of the fact that the introduction of yet another seismic data format should ideally be avoided. However, we believe it to be justified because the current state of the art is just not good enough. We further believe that the advantages of the proposed format are significant enough to quickly outweigh the initial difficulties of switching to a new format. We identify five key issues that a new data format must resolve, namely:

- **Efficiency:** Data storage is cheap, but data operations are increasingly becoming the limiting factor in modern scientific workflows. More efficient and better performing data processing and analysis tools are badly needed.
- **Data Organization:** Different types of data (waveforms, source & receiver information, derived data products such as adjoint sources, receiver functions, and cross correlations) are needed to perform a variety of tasks. This results in ad hoc data organization and formats that are hard to maintain, integrate, reproduce, and exchange.
- **Data Exchange:** In order to exchange complex datasets, an open, well-defined, and community driven data format must be developed.

- **Reproducibility:** A critical aspect of science is the ability to reproduce results. Modern data formats should facilitate and encourage this.
- **Mining, Visualization, and Understanding of data:** As data volumes grow, more complex, new techniques to query and visualize large datasets are needed.

The ultimate goal is to empower seismologists to focus on actual science. This is the time for the community to build an organized, high-performance, and reproducible seismic data format for seismological research. In order to facilitate integration of the new format into existing scientific workflows and to demonstrate that this is not just an academic exercise, we developed a Python library hooking ASDF into the ObsPy library [8], which, as a hugely beneficial side-effect, also takes care of any data format conversion issues, be it to, or from ASDF. A C-based ASDF library features an API for reading and writing ASDF files and includes examples in both C and Fortran. Embedding this library in the widely used spectral-element waveform solver SPECFEM3D_GLOBE [55, 56] made it gain native support for ASDF-integrated workflows. To engage and educate the community, a wiki provides demonstrations of the format and includes technical and non-technical introductions for both users and developers.

2.2.2 Scope

The proposed Adaptable Seismic Data Format is designed to be an efficient, self-describing data format for storing, processing, and exchanging seismological data, including full provenance information. It is intended to be used by researchers and analysts working with data, after it has been recorded. In contrast, it is not aspiring to replace the time proven MiniSEED format for data archival, streaming,

and low-latency applications. These use cases are contrary to a comprehensive and self-describing data format and both can probably not be achieved simultaneously.

ASDF is applicable to a large number of areas in seismology and related sciences. Its use ranges from classical earthquake seismology to active source datasets, ambient seismic noise studies, and GPS time series. Furthermore, it is generic enough to accommodate any kind of derived or auxiliary data that might accrue in the course of a research project.

2.2.3 Benefits

A well-defined format with the previously listed attributes directly results in a number of advantages and applicable use cases. In this section we list a few of these, in no particular order.

- Seismological datasets usually contain waveform data as well as associated meta data, such as information about events and stations. All this data needs to be integrated and accessed concurrently, which requires a large amount of book-keeping as datasets grow. Many tools are one-off scripts that cannot be reused for subsequent projects. Additionally, datasets become difficult to share with research groups that do not employ the same internal structure and data organization. Over the years, numerous groups have developed customized seismological data formats to work around these limitations. In contrast, ASDF is a well-defined format that can be used to store and exchange full seismological datasets, including all necessary meta information.
- It is oftentimes convenient to locally build up a database of preprocessed waveforms. A common example is storage of instrument corrected and bandpass filtered data. If a project continues for some years, it might ultimately no longer be known how exactly data were processed. The make up of the team may have

changed, or perhaps the processing software had a bug that has been fixed in the meantime, and this may or may not have affected the data. *Provenance*, that is, the tracking and storing of the history of data, solves this particular problem, and ASDF accommodates that. Existing data formats do not (or only in a very limited manner) track the origin of data and what operations were performed on it due to limited and inflexible metadata allowances. ASDF is capable of storing the full provenance graph that resulted in a particular piece of waveform or other data.

- For the first time, ASDF accommodates proper storage and exchange of synthetic seismograms, including information about the numerical solver, earthquake parameters, the Earth model, and all other parameters influencing the final result. Waveform simulations at high frequencies and in physically plausible Earth models are extremely expensive computationally, so preserving and carefully documenting such simulations is of tremendous value.
- ASDF greatly reduces the number of files necessary for many tasks, because a single ASDF file can replace tens to hundreds of thousands of single waveform files. Beside raw performance and organizational benefits, this also facilitates workflows that run into hard file count quota limits on supercomputers. Note that ASDF can store data from very many receivers as well as arbitrarily long time series from only a single receiver and any combination in between.
- Importantly, ASDF offers efficient parallel I/O on modern clusters with the required hardware. This facilitates fully parallel data processing workflows that actually scale.
- ASDF offers optional and automatic lossless data compression, thereby reducing file size.

- Seismograms are certainly not the only type of data used in seismology. Other data types, including spectral estimations, cross correlations, adjoint sources, receiver functions, and so on, also benefit from organized and self-describing storage.

ASDF is intended as a container for all the various kinds of data materializing in seismological research, including all required meta information. Additionally, each piece of data should be able to describe itself and what led to it. Having an organized and standard data container will, in the long run, increase the speed and accuracy of seismic research, and provides a medium for effectively communicating research results. The rest of this chapter is structured as follows. We first provide an overview of the layout of the format and justify some choices that needed to be made. We then compare the ASDF format to existing data formats in use in seismology, thereby further justifying its development. Finally, we showcase a number of existing implementations, detail several use cases for the ASDF format, and discuss future possibilities. The article is intentionally light on technical details to focus on a high-level view. A technical definition of the ASDF format can be found on line and in the electronic supplements.

2.3 Overview of the Format

ASDF, at its most basic level, organizes its data in a hierarchical structure inside a container — in a simplified manner a container can be pictured as a file system within a file. The contents are roughly arranged in four sections, as follows.

1. Details about seismic events of any kind (earthquakes, mine blasts, rock falls, etc.) are stored in a QuakeML document.

2. Seismic waveforms are sorted in one group per seismic station together with meta information in the form of a StationXML document. Each waveform is stored as an HDF5 array.
3. Arbitrary data that cannot be understood as a seismic waveform is stored in the auxiliary data section.
4. Data history (provenance) is kept as a number of SEIS-PROV documents (an extension to W3C PROV).

Existing and established data formats and conventions are utilized wherever possible. This keeps large parts of ASDF conceptually simple, and delegates pieces of the development burden to existing efforts. The ASDF structure is summarized in Figure 3.10 and is discussed in more detail in the following paragraphs. It is worth noting that almost everything is optional. The amount of stored information can thus be adapted to any given use case.

2.3.1 Container

Large parts of the ASDF definition are independent of the employed container format. An advantage of this approach is a certain resilience to technological changes as major pieces of ASDF can in theory be adapted to other container formats. Nonetheless, the container format has to be fixed to not severely affect interoperability and ease of data exchange. We evaluated a number of possibilities and chose HDF5 (Hierarchical Data Format version 5) [128]. It is used in a wide variety of scientific projects and has a healthy and active ecosystem of libraries and tools. NetCDF 4 [105] is implemented on top of HDF5 and ASDF does not gain from the additional functionality. While not being as fast as ADIOS [70] for the most extreme use cases, HDF5 also fulfills our hard requirement of being capable of efficient parallel I/O with MPI (message passing interface) [93]. It can be argued that seismology does not have to deal with

the same amount of data as, for example, particle physics or biology, where single datasets can easily attain volumes of multiple petabytes [9, 120]. At the time of writing, the HDF5 libraries work on more platforms and have more users as well as available tools, which we believe is well worth the minor loss in maximum potential I/O performance. Using HDF5 also grants a number of useful features (other formats also offer some or all of them): First, there is no need to worry about the endianness of data, which historically has been a big issue in seismology. Second, HDF5 has a number of built-in data compression algorithms and data corruption tests in the form of check summing.

2.3.2 Seismic Event Information

Information about all kinds of seismic events, including earthquakes, building collapses, fluid injections, and so on, are stored in a single QuakeML [116, 115] file inside the container. QuakeML is an XML [14] representation intended for different types of seismological meta information, but is in practice mostly used to describe earthquakes.

Note that one QuakeML document can describe an arbitrary number of events in a comprehensive manner. It is the de-facto standard for defining seismic events, adopted as a standard by the International Federation of Digital Seismograph Networks (see <https://www.fdsn.org>), and widely available, because it is served by web services of data centers around the world. A crucial capability is that it can specify a number of different hypocenters and focal mechanisms for each individual event, which might be the results from different source inversion algorithms. Each of these is identified by a unique id. ASDF uses these identifiers to, for example, determine the exact moment tensor and event location that was used to simulate an event that resulted in a particular waveform.

Shortcomings of the latest QuakeML version at the time of writing include no proper possibility for storing either finite fault sources or custom source time functions. This might be alleviated in future QuakeML versions, at which point ASDF also gains that functionality. As of now, both could either be stored in custom elements in a QuakeML document in a separate namespace, or as part of the auxiliary data section of ASDF files.

The exploration community employs seismic sources that cannot be appropriately described by the QuakeML standard. Nonetheless the concept of having detailed descriptions of seismic sources naturally translates to the active source case. It is conceivable that a standard for describing these sources might appear in the future at which point it can be incorporated into ASDF. In the use cases section we demonstrate how that could be achieved.

2.3.3 Waveforms and Station Meta Information

At the heart of ASDF is the waveform data. A single file can store any number, combination, and length of waveform data. Waveforms are restricted to single and double precision floating point and signed integer data and are stored as HDF5 native data arrays. These data arrays are logically grouped by using four codes: the network code denotes the operator of a seismological network, the station code denotes a station within that network, the location code denotes a particular instrument at a station, and finally the channel code denotes the recording component. These codes are often called SEED compatible identifiers [82] and, together with some temporal information, allow the unique identification of seismic instruments and are also used in the QuakeML and StationXML standards.

ASDF organizes waveforms and associated meta information at a station level granularity. Other choices would have been possible, but this provides a certain balance between the necessary nesting and the number of elements per group (like

a directory in HDF5 terms). Each station can optionally contain a StationXML document made up of meta information for one or more channels of that station. StationXML is the current FDSN standard for station information and the successor of the SEED standard. Roughly speaking, it contains information about who runs a network and deployed the station, about the geographical and geological setting of the station, and the impulse response of each recording channel. This is vital information, and storing it alongside the actual waveform data eases many common undertakings. A StationXML document can contain as much or as little information as appropriate for any given task. A further benefit is that StationXML can also be used to describe non-seismological time series, such as pressure and temperature curves.

The waveform data are stored as pieces of continuous, well-behaved time series data. Each piece, in the following called a trace, consists of a start time, a sampling rate, and a data array representing regularly sampled data. The starting time of each trace is internally represented as a nanosecond precision UNIX epoch time. The use of a 64-bit integer grants a temporal range from about the year 1680 to 2260, which is sufficient for all envisioned use cases. Times are always in UTC in accordance with most other seismological data and file formats.

Every station can contain an arbitrary number of traces consisting of data from multiple locations and channels. Each trace is named according to the following scheme:

`NET.STA.LOC.CHA__STARTTIME__ENDTIME__TAG`

`NET`, `STA`, `LOC`, and `CHA` are placeholders for the network, station, location, and channel codes. `STARTTIME` and `ENDTIME` are string representations of the start and end time of the trace. The final `TAG` part serves as another hierarchical layer. The need for this layer becomes obvious, for example, when attempting to store data from two waveform simulations but with a slightly different Earth model. They need

to be given different names — a randomized string would have been possible, but human readable tags seem to be a nicer alternative. Unprocessed data straight from a digitizer are, by convention, given the tag `raw_recording`; other tags will always depend on the use case. Traces may have any length without inhibiting the ability to work with them. Incidentally, HDF5 supports reading portions of an array which enables users to read only portions of very long time series within an ASDF file.

Real world data are not perfect, and seismic receivers can fail and thus produce gaps or overlaps in data. Many existing file formats have no concept of this and thus require workarounds. In ASDF a gap is represented by one trace before and another trace after the gap and two overlapping traces denote an overlap. This construct has proven itself to work very well in practice and is also employed in the MiniSEED format as well as the ObsPy library.

Last but not least, each trace potentially also carries some more meta information and relations to other places within an ASDF file. These are elaborated upon in a later section.

ASDF’s construction is not a perfect fit for active source exploration data, which is mainly a consequence of the chosen nesting structure and StationXML heavily leaning towards passive source and station based seismology. Most branches of seismology, however, work with the concept of sources and receivers. Thus we encourage the exploration community to come up with a general definition of their receivers, at which point it can be integrated into ASDF with only a minor effort.

2.3.4 Auxiliary Data

Seismologists are used to working with waveform data so they oftentimes exploit the same formats for other data. Receiver functions, cross correlations, and H/V stacks are all examples of this reuse. Header fields of the format are then used to store some limited amount of meta information. This becomes problematic if that data

should be archived for future generations of researchers or exchanged with the wider community. Within the ASDF format this type of data is referred to as auxiliary data, and can be anything that is not considered a seismic waveform. Conceptually, each piece of auxiliary data is stored in an arbitrarily nested path in the auxiliary data group and consists of a data array of any dimension and any necessary meta information in a key-value representation.

ASDF does not define auxiliary data in more detail on purpose. On the one hand, many areas of seismology where the concept of auxiliary data is interesting are in a heavy state of flux and are seeing a lot of active research. It is often unclear what to store and keep track of and that view constantly evolves. On the other hand, we are not experts in all areas of seismology, and it would take a long time to agree on what needs to be stored for each type of auxiliary data.

Over time, we hope that conventions for certain types of data, such as cross correlations, will become established by the wider community. Nonetheless, ASDF allows for arbitrary and descriptive meta information for any type of data to explain what the data actually is. This becomes particularly powerful when combined with the provenance information, which is described next.

2.3.5 Provenance

Reproducibility is frequently discussed and widely recognized as a critical requirement of scientific results. In practice, it is so difficult and time consuming to achieve that it is frequently just ignored. Provenance is the process of keeping track of and storing all constituents of information that were used to arrive at a certain result. This information is then used to judge the quality and trustworthiness of the results. While not being identical to reproducibility, the concept of provenance is a key ingredient towards this goal.

Each piece of waveform and auxiliary data within ASDF can optionally store provenance information in the form of a W3C PROV or SEIS-PROV document. This implies that ASDF can store any piece of observed, processed, derived, or synthetic data with full provenance information. Thus, such a file can be safely archived and exchanged with others, and information that led to a result is readily available to the user. It is important to note that SEIS-PROV only documents the processes that led to a certain piece of data. It does not, by default, store the actual data at each intermediate step, although this could also be achieved within the ASDF format.

W3C PROV is a data model to describe provenance, and SEIS-PROV is a domain-specific extension for using W3C PROV in the context of seismological data processing and generation. We quickly introduce SEIS-PROV as it is a critical component of ASDF; the motivation and reasoning behind it will be detailed in a separate publication.

Provenance can be described from different points of view. SEIS-PROV employs a process-centered provenance description that aims to capture all actions taken to arrive at a result. This is a natural fit for seismological data processing. In a nutshell, it works by describing things or entities which (in the context of seismology) might be waveform traces or cross correlation stacks at different stages in a processing chain. These representations are then connected by so called activities that can use existing entities and create new ones. A simple example of an activity is a filter in signal processing that takes an existing waveform trace and produces a new, filtered one. Additionally, all entities and actions can be assigned to agents that are responsible for it. Agents are usually persons or software programs. Figure 2.2 illustrates these concepts with a simplistic example.

The goal of the provenance descriptions in ASDF is that scientists looking at data described by provenance should be able to tell what steps were taken to generate the result.

ASDF only takes care of the storage of the provenance information. In practice, provenance will only be generated and used if it is captured and stored in a fully automatic fashion and is thus strongly dependent on the software used to generate and process data.

2.3.6 Data Relations

Data always needs to be regarded and interpreted in a wider context. This ranges from information about the origin of the data, which is dealt with in the previous section, to relations to other pieces of data. Classical relations in seismology are waveform data and information about the recording site and instrument, as well as the sources of the recorded wavefield.

Any time different pieces of data are required that are stored in varying places, formats, and files, the required bookkeeping to make workflows run can be substantial. ASDF greatly eases that pain by storing everything in a well-defined place within the same file. The need to find and assemble the different pieces can thus be performed by software, thereby requiring less mental work from scientists. ASDF, as shown in the previous sections, can store waveforms, events, station meta information, provenance, and auxiliary data all in the same file. Additionally, it permits relations between these items. For example, each waveform trace can be associated with a certain event, or a certain event origin or focal mechanism. Relations for each block of data to its provenance record are also retained.

All in all this allows for fully self-explanatory, complete datasets preserving complex internal relations. This is something that is required in scientific and data driven applications. Today, people usually use project-specific directory structures that cannot be exchanged nor properly archived, and ASDF clearly improves that system on all fronts.

2.4 Comparison to Existing Formats

Having yet another format induces more complexity and, potentially, noise into the community using that type of data and the landscape of software able to deal with it. “Do we really need a new format?” is thus a natural and understandable question. This sections addresses why no single existing data format in seismology is able to satisfy our needs and thus justifies the introduction of the ASDF format.

We limit ourselves to detailing alternative waveform formats as we directly incorporate the StationXML and QuakeML formats and no true alternative to storing derived data or provenance is currently in existence. A wide variety of different seismological data formats is used by researchers world wide. We will discuss the most widely used ones, namely, (Mini)SEED, SAC, and SEG Y/PH5. Please see [10] and [48] for additional information and descriptions of more formats.

2.4.1 MiniSEED

The Standard for the Exchange of Earthquake Data (SEED) was developed in the late 1980s and at least the data-only part (MiniSEED) continues to be in wide use today, and will likely continue to be the dominant data streaming and archival format for the foreseeable future. The ASDF format does not attempt to replace it. Some of MiniSEED’s features, such as the ability to build up large data volumes by concatenating small and short pieces, are very well suited for their use in data archives, where data is constantly streamed in. While the full SEED format can in theory store waveforms as well as station meta information, the complexity of the format hinders that. It furthermore can only properly store raw waveform recordings and no event information. Additionally, the dataless part of SEED, e.g., the part with the station information, sees declining usage nowadays with that responsibility being taken over by StationXML. MiniSEED, on the other hand, is more than capable of storing ar-

bitrarily large waveform volumes, but the file then contains no index of what is in it, so one must always read the entire file to figure that out, making large data volumes fairly impractical. Additionally, the amount of meta information in MiniSEED files is strongly limited, so one always needs additional files to work with it.

Summing up, MiniSEED is a good data archival format for data centers, streaming, and low-latency applications, but it is not well suited for the later research and processing stages, where ASDF has significant advantages.

2.4.2 SAC

The Seismic Analysis Code (SAC, [49]) introduced a new format named after its parent program, and is still in widespread use today. This is likely due to two reasons: the popularity of the SAC program itself and the relative simplicity of the format with a number of header fields that can be adapted to different purposes.

The SAC format is well suited for many tasks, but ASDF offers a number of advantages. The most obvious ones are the ability to store multiple components — including gaps and overlaps — in a single file without awkward workarounds, as well as the potential to create full datasets incorporating all necessary meta information. ASDF is, for large workflows, also more efficient, facilitates the storage of different data types — integers as well as floats — and, with the help of HDF5 offers file compression and check summing.

The combination of these factors results in ASDF being more suitable and convenient for many workflows. Some, for example experiments with millions of waveform files, are almost impossible without a more advanced seismological data format. In fact, part of the motivation for developing ASDF stems from the fact that reading and writing SAC files for a large tomographic inversion practically brings a huge parallel file system to its knees due to the very large number of involved files.

2.4.3 SEG Y and PH5

The SEG Y Data Exchange Format [117] is one of many in the family of data formats introduced and defined by the Society of Exploration Geophysicists (SEG) Technical Standards Committee. Amongst these, it is probably the most widely known and used. The more modern PH5 [53] format has a data model similar to SEG Y, but stores its data in an HDF5 container. This eliminates some limitations of the SEG Y format and facilitates more extensive meta information. It has been developed as an archiving format for active source seismic experiments. Typical workflows extract data from PH5 and save it as SEG Y, which is used in the further stages.

Both on- and off-shore active source data is very structured, meaning that all receivers generally have the same response and record for the same time span with the same sampling rate. Receivers are placed in lines and geo-referenced by relative coordinates. In contrast, passive source seismology is frequently very unstructured, with different receiver types scattered across a geographical region, and the meta information is fairly rich and detailed.

SEG Y and PH5 are well suited for active source experiments, but it is difficult to adapt these formats for passive source seismologists to suit their purposes. Historically, SEG Y is essentially not used in passive source seismology, and there is no reason to expect this will change with PH5. The inverse is true as well, in that passive source seismology tools are rarely used in active studies. A consequence is that the current iteration of the ASDF format is not fully suitable for exploration studies as it relies on certain formats and conventions. In the use cases section we will show an example of how it can still be done.

The concept of seismic sources and receivers nonetheless holds true in both active and passive source seismology. We have the hope that, in the future, ASDF will be used as a standard for both. Active source seismology currently lacks community accepted standards for sources and receivers as is common in passive source seismology

with formats like QuakeML and StationXML. Methods, ideas, and techniques are frequently exchanged between these communities, and we encourage the development of these missing standards. A common data format would enable greater sharing of tools, whole workflows, and most importantly human knowledge and skill, greatly benefiting both sides. The ASDF format is ready to incorporate these aforementioned definitions.

2.5 Implementations

We developed three usable implementations of the ASDF format and expect more to follow:

1. A C library with Fortran bindings to read and write ASDF files. This is for example used in the SPECFEM3D_GLOBE [55, 56] wave propagation solver.
2. A Python library to read, write, and convert ASDF files to a large number of other formats backed by the ObsPy library [84, 60].
3. A graphical user interface to visually and interactively explore the contents of ASDF files.

Technological advances often make existing codes and tools obsolete in a matter of just a few years, and we anticipate that these implementations will continue to undergo rapid development and expansion.

2.6 Demonstrations and Use Cases

The proposed ASDF format can be used in a number of different branches in seismology and its success will revolve around its adoption by the seismological community. This section shows some practical applications and benefits of the format.

2.6.1 Dataset Building

A dataset is the collection of all data necessary for a particular purpose. Examples include waveform data for a number of stations for a particular earthquake, all waveforms from a single array, or data from an active source study. A complete dataset also includes information about seismic receivers and sources and therefore contains everything that is needed for a certain task. All of this can be stored in a single ASDF file. Thus, one no longer needs to deal with complicated and custom directory structures. Tools and scripts written to work on larger datasets can work on a defined structure and be exchanged and adapted to new uses more easily.

Aside from facilitating data management this greatly decreases the number of files one has to deal with. Transfer and copy times can be prohibitive when dealing with a large number of small files. One million waveform files can easily take an hour to transfer from a cluster to a personal workstation. Storing all these waveform in about 50 ASDF files reduces the total transfer time to about a minute. Additionally, many clusters and operating systems impose hard file count limits.

HDF5 furthermore grants access to a number of different lossless compression algorithms reducing the size of ASDF files. Figure 2.3 shows the efficiency and computational cost of these for a number of typical seismological datasets.

2.6.2 Storage, Exchange, and Archival of Processed or Synthetic Waveforms

Synthetic seismograms can be very expensive to compute, especially in three-dimensional media with realistic rheologies. The same is true for some processing chains to, for example instrument correction, and filtering of data, and it is thus oftentimes worthwhile to preserve these pieces of data.

Their proper long-term storage, exchange, and archival is only possible if all processes that went into their creation are documented and stored alongside the data. This includes, for example, the precise version of the used software, and details about all processing steps. For synthetic data it includes the used Earth and source model as well as the waveform solver’s settings. ASDF, in combination with SEIS-PROV, preserves all this information.

2.6.3 (Parallel) Large Scale Data Processing

Data volumes are constantly growing, and the community has access to the computing power needed to process and work with it. However, we are at a point where I/O itself, i.e., reading and writing from and to disk, is one of the most expensive parts of many operations. This is especially true for a very large number of typically small files, as previously pointed out. ASDF, with the help of HDF5, supports efficient, parallel I/O on full data sets. Our implementations shown in the previous section make use of this and facility the construction of fully parallel workflows.

Applications for this operational approach are numerous and in the following we illustrate ASDF on an example occurring in large scale full waveform inversions using adjoint techniques [135, 35, 122], but the general concepts translate to other types of workflows using large amounts of data. This iterative procedure requires routine comparison of millions of waveform traces. We replaced an implementation based on the SAC package and file format [49] with an ASDF centered implementation. The SPECFEM3D_GLOBE waveform solver [55, 56] directly produces ASDF files which are then tied into a single cohesive workflow relying on the ObsPy [8] package. All components integrate with each other and stream data from one unit to the next. I/O only happens at the very beginning and the end.

These changes empower us to increase the scale of our inversions —in terms of frequency content, number of earthquakes, and number of stations— and fully exploit

modern computational platforms. Additionally, they reduce the complexity of operations and thus stabilize them. Last but not least, provenance information is kept to increase reproducibility and for future reference.

2.6.4 Active Source Industry Dataset

Industry datasets are not the primary focus of the ASDF format, but it is worthwhile proposing how we could adapt the format to that particular case in an effort to bring the active and passive communities closer together. Active source data is more structured and array-like, both in sources and receivers. As the industry currently lacks standards to describe these, we utilized the QuakeML and StationXML formats with some extensions to for example share the array configuration and source time functions. Waveforms are grouped by recording instrument — one network corresponds to one receiver layout.

We believe the industry would benefit from adopting ASDF, since the format offers improved data organization, simple but efficient parallel processing, and provenance capabilities all wrapped up in a modern format. Please refer to section 2.4.3 for some concrete suggestions and requirements.

2.6.5 Further Uses

The extraction of information from recordings of ambient seismic noise is a prime candidate for fully utilizing ASDF as the required data volumes are amongst the biggest in our science. ASDF enables the storage of arbitrarily long waveform traces in a single file with fine grained access. One example is storing a station’s data for several years in one file and only accessing a portion of the data whenever it is needed.

Many more use cases of the ASDF format can be envisioned, and we hope different subgroups within the seismological community will adapt it for their own purposes.

Aside from seismological waveforms, ASDF’s ability to save auxiliary data, including full provenance, enables it to store a lot of different pieces of data.

Examples include storing time dependent power spectral densities and combining them into probabilistic power spectral densities on the fly [83] or building a database of historical earthquake data. Even non-seismological data, such as GPS time series and magnetotelluric data, is not out of the question and would benefit from the provenance description and the advanced processing tools developed around ASDF. Some of these examples are already being attempted, and we intend to maintain a collection of use cases on our website.

2.7 Conclusions and Future Directions

ASDF has been developed with the broader seismological community in mind, and our hope is that scientists within this community will continually test, offer feedback, and improve the format and its associated tools. Through such a communal effort, we will gracefully meet future data challenges and empower ourselves to make new scientific discoveries.

All components of the format, including its definition, implementation, and other tools, are freely available under open source licenses and hosted on GitHub. A central entry point is the <http://seismic-data.org> website. We welcome any outside comments, criticisms, and success stories, and we are committed to maintaining the documentation and implementations for the foreseeable future.

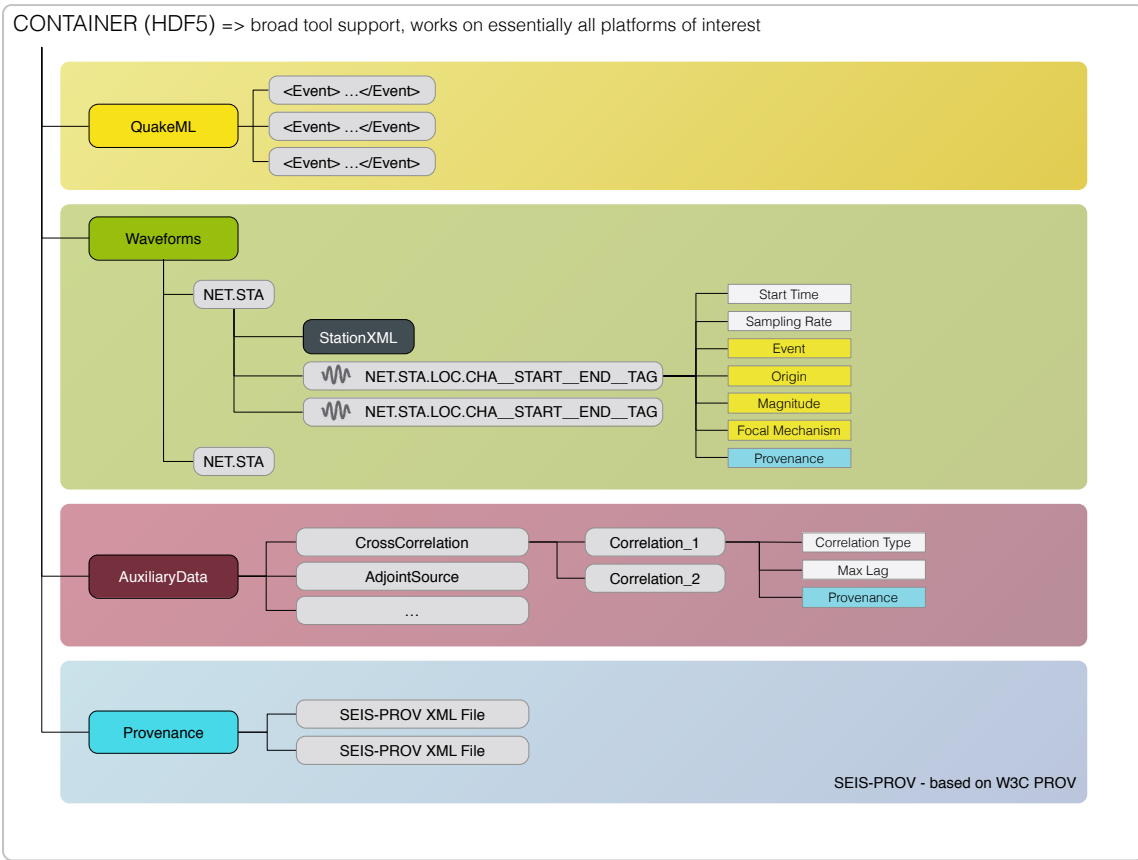


Figure 2.1: The general structure of an ASDF file in its HDF5 container — it has four distinct parts: (1, yellow) Information about an arbitrary number of earthquakes (or other seismic events) is stored in a single QuakeML document, the most complete earthquake description format currently available. (2, green) Seismic waveforms are stored per station together with the necessary meta information in the form of an FDSN StationXML document. (3, red) Anything that cannot be regarded as a seismic waveform is hierarchically stored in the auxiliary data section. (4, blue) Provenance information is stored as a number of SEIS-PROV documents, an extension to W3C PROV. Background colors in the attributes (rectangular boxes) denote relations to other sections in an ASDF file. Examples of this are relations of a waveform to a certain event or a provenance record for a piece of auxiliary data.

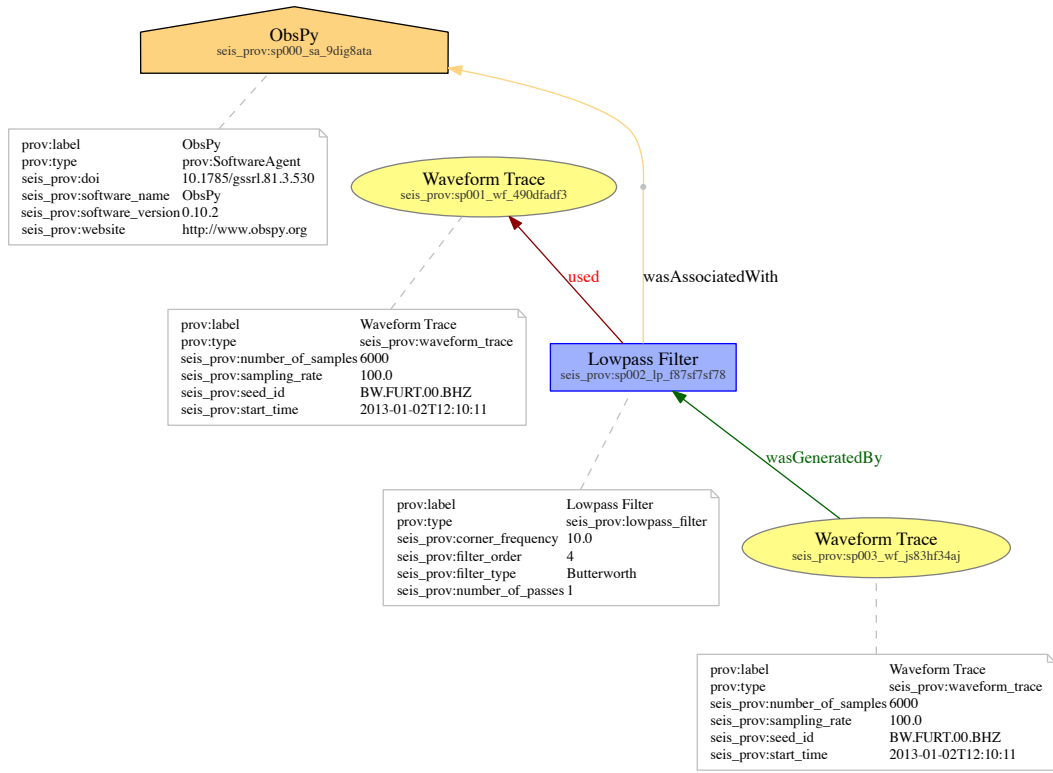


Figure 2.2: Simple example to illustrate the key concepts of storing provenance information with SEIS-PROV and W3C PROV. It describes a single waveform trace that has been lowpass filtered to create a filtered waveform trace. The arrows in this graphical representation mostly point backwards in the process towards the origin of something. The yellow ellipses are called entities, and here they represent a waveform trace at two different points in time. The blue rectangle is an activity that can use and generate entities. It denotes a lowpass filter and uses the first waveform trace to generate a new, filtered waveform trace. The orange house shape symbolizes an agent who is responsible for something. In this case it stands for the software that performed the filtering operation. Finally, the white rectangles are attributes with more details about any node. Please note that this figure shows only one possible graphical representation of the underlying data model and more or less detailed ones can be employed as appropriate.

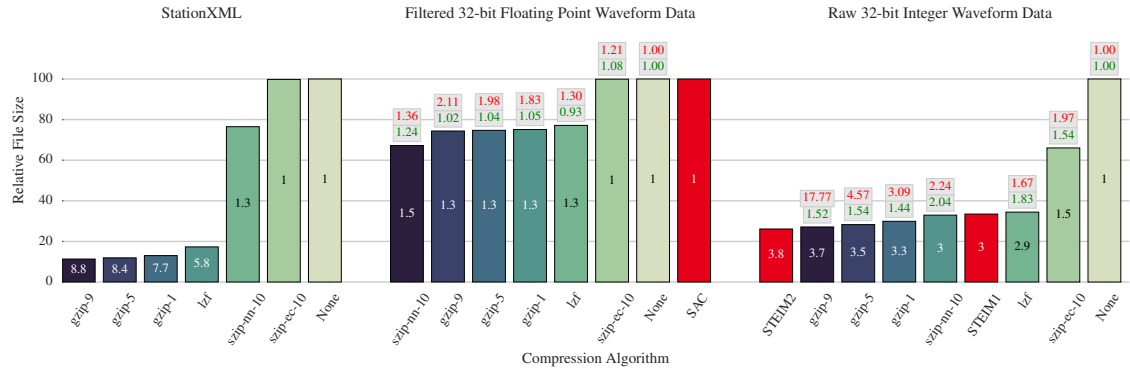


Figure 2.3: Compression efficiency of the ASDF format using algorithms available in HDF5 for a number of typical seismological datasets. Please keep in mind that the efficiency and I/O speed of these algorithms are heavily dependent on the actual data and hardware, and thus your mileage may vary. The columns represent the file size relative to the uncompressed case, the numbers inside are the achieved compression ratios. The small boxes above the columns denote the relative writing duration in red and the relative reading duration in green compared to the uncompressed case. The left plot shows the efficiency for a dataset containing 500 StationXML documents adding up to 120 MiB. I/O speed differences are irrelevant as the cost for parsing and generation of the XML documents is constant and dominates the total run time. The middle plot shows the compression efficiency for a bandpass filtered waveform dataset stored as 32-bit floating point numbers. It consists of 3,466 waveform traces taking up 282 MiB on disk. The red bar compares it to the uncompressed SAC format. The rightmost plot shows the efficiency for storing 3,346 raw waveform files stored as 32-bit integers taking up 2,340 MiB. The red bars here show the efficiency for the same dataset of the STEIM1 and STEIM2 special purpose compression algorithms defined for the SEED format measured by writing them as MiniSEED files.

Chapter 3

Data & Workflow Management for Exascale Global Adjoint Tomography

Note

This chapter was submitted as a chapter with the same title by M. Lefebvre, Y. Chen, W. Lei, D. Luet, Y. Ruan, E. Bozdag, J. Hill, D. Komatitsch, L. Krischer, D. Peter, N. Podhorszki, J. Smith, and J. Tromp, in the book entitle "Exascale Scientific Applications: Programming Approaches for Scalability, Performance, and Portability", Chapman and Hall/CRC 2017.

3.1 Introduction

Striving to comprehend Earth's interior has been a longstanding pursuit for humankind, and has been fantasized by many, from Dante Alighieri [26] to Jules Verne [140]. Seismologists see Earth's interior through seismic waves generated by seismic sources such as earthquakes, oceanic noise or man-made explosions, and recorded by seismic instruments deployed at the surface. The information inherent to

these seismic waves, which are sensitive to physical parameters of the medium they propagate through, is used to construct 3D images of the Earth based on *seismic tomography*. Advances in the theory of wave propagation and 3D numerical solvers, supported by dramatic increases in the amount and quality of seismic data as well as the unprecedented amount of computational power provided by large-scale high-performance computing centers, enables us to greatly improve our understanding of the physics and chemistry of Earth’s interior.

Adjoint methods are very efficient at incorporating 3D numerical wave simulations in seismic tomography. They have, for instance, successfully been applied to regional- and global-scale earthquake tomography [121, 34, 153, 12] and —to some extent—in exploration seismology studies [156, 77].

Adjoint tomography workflows consist of a series of iterations. Each iteration is composed of a few shared operations (e.g., mesh generation, model updates) and of a large number of embarrassingly parallel operations (e.g., forward and adjoint simulations for each seismic event, pre- and post-processing of seismic data). One of the main computational challenges is to increase the quality of seismic models while keeping the time to solution as short as possible. Having fast and efficient solvers still remains an important concern [106], but new obstacles have emerged: large-scale experiments and big datasets create bottlenecks in workflows causing significant I/O problems on HPC systems.

In this chapter, we devise and investigate strategies to scale global adjoint tomography to unprecedented levels by assimilating data from thousands of earthquakes. We elaborate on improvements targeting not only current supercomputers, but also next generation systems, such as OLCF’s *Summit*. The following remarks and developments stem from lessons learned while performing simulations on OLCF’s *Titan* for the first-generation global adjoint tomography model, which is the result of 15 iterations and a limited dataset of 253 earthquakes [12].

We begin in Section 3.2 by laying down the scientific methodology of the global adjoint tomography problem and providing explanations of the scientific workflow and its components. We then follow a reductionist approach, considering each component individually. Section 3.3 examines the computational aspects of `SPECFEM3D_GLOBE` [55, 56], our 3D seismic wave equation solver and the most computationally demanding part of our workflow. We provide a brief overview and discuss the programming approach it follows. We also present scalability analyses. Section 3.4 is closely related to the solver and describes the approach we chose to optimize I/O for computational data, that is, data related to meshes and models. We then describe a modern seismic data format in Section 3.5. Assimilating a large number of seismic time series from numerous earthquakes requires improvement of legacy seismic data formats, including provenance information and the ability to seamlessly integrate in a complex data processing chain. With the previous points in mind, Section 3.6 returns to our initial holistic approach and discusses how to bring the global adjoint tomography workflow bits and pieces under the control of a scientific workflow management system. Finally, Section 3.7 explains our approach to software practices, an often overlooked but crucial part of scientific software development.

3.2 Scientific Methodology

Seismic tomography involves the construction of images of Earth’s interior by minimizing a predefined misfit function involving observed and synthetic data. Typically, seismic signals are generated by a wide variety of sources and recorded by a set of receivers as time series of a physical quantity. Sources can be either passive (e.g., earthquakes, ambient noises) or active (e.g., nuclear explosions, air guns, etc.). In the most common cases, the receivers record a quantity, such as displacement, on vertical and/or horizontal components. In the past decades, seismic datasets have

grown very fast with accumulating sources and a dramatic increase in the number of receivers (e.g., cross-continental array deployments in passive seismology, 3D surveys in active source seismology). Such growth provides more information to constrain the model in greater details, but also poses a challenge for processing massive seismic data. In addition to the data deluge, a numerical solver capable of accurately simulating seismic wave propagation is very important for tomography to achieve higher resolution. To solve the (an)elastic or acoustic wave equation in realistic 3D models, a spectral-element method [54, 55, 56] is used to achieve high accuracy for realistic Earth models in complex geometries. Since the most computationally expensive part of a tomographic inversion involves wavefield simulations, excellent performance of the solver is crucial, as discussed in Section 3.3.

Using data from 253 earthquakes and adjoint tomography technique, we generated model GLAD-M15 [12], the first Earth model where forward and Fréchet derivative calculations were performed numerically in 3D background models. To further improve the resolution of this model, we have expanded the dataset to 1,000 earthquake, and will eventually include all available earthquakes (Mw 5.0-7.0) on the global scale (more than 6,000 as of 2016). Inverting such a large dataset requires optimizing I/O performance within data processing and simulations as well as efficient management of the entire workflow. Preparing for exascale computing in seismic tomography, we address the bottlenecks we encounter in our current adjoint tomography studies and discuss possible solutions. A typical adjoint tomography workflow is shown in Figure 3.1. It involves three major stages: (1) calculating synthetic seismograms and pre-processing observed and synthetic data, (2) calculating the gradient of the misfit function (the Fréchet derivatives), and (3) post-processing and updating the model.

The pre-processing stage is dedicated to assimilating data: (1) signal processing (i.e., tapering, re-sampling, filtering, deconvolving the instrument response, etc.), (2) window selection to determine the usable parts of seismograms according to certain

criteria by comparing observed and simulated seismograms; and (3) making measurements in each window and computing the associated adjoint sources [135, 121, 156, 77]. The pre-processing stage can easily involve dealing with millions of seismograms and has become a bottleneck in tomographic inversions. Although some groups have their own data formats, the Seismic Analysis Code (SAC) format has been the main seismic data format for earthquake seismology. Seismic data in SAC files are single time series stored independently for each component of each receiver, along with limited metadata as header. For large scales studies, this format produces severe I/O traffic in data processing and numerical simulation due to the large numbers of files to be dealt with. An Adaptable Seismic Data Format (ASDF) has been developed as an alternative to SAC. It enables flexible data types and allows storing large data in a single file through its hierarchical organization. We illustrate the advantages of this new data format in Section 3.5.

Computing the gradient of the misfit or objective function is accomplished through the interaction of a forward seismic wavefield with its adjoint wavefield; the latter is generated by back-projecting seismic measurements simultaneously from all receivers [?]. This procedure requires two numerical simulations for each source: one for the forward wavefield from the source to the receivers, and another for the adjoint wavefield from all the receivers to the source. The simulations are run for each source, resulting in *event kernels*, and the gradient of the misfit function is simply the sum of all event kernels. Between forward and adjoint simulations, we need to store a vast amount of wavefield data to account for the full attenuation of seismic waves in an anelastic Earth model. For thousands of events, the I/O approach we used to efficiently calculate the kernels is discussed in Section 3.4. In the post-processing stage, the gradient is pre-conditioned and smoothed. Based upon the gradient, a model update is obtained using a conjugate gradient or L-BFGS [97] optimization scheme. Usually, tens of iterations have to be performed to obtain a stable model, and in

Summary of computational requirements for a maximum resolution of 17 seconds, using 180 minutes seismograms on OLCF infrastructure.

	1 earthquake	253 earthquakes	6,000 earthquakes
Shortest period: 17 s		1 iteration	1 iteration
Duration: 180 m			
Solver (core hours) (forward+adjoint)	~ 11,520	~ 2,764,560	~ 69,120,000
Pre-processing (core hours)	~ 15	~ 3,795	~ 90,000
Post-processing (core hours)	~ 5,760	~ 5,760	~ 5,760

each iteration we have to process data, and run forward and adjoint simulations for thousands of events. At each stage, an additional complication is the necessity to check results and relaunch jobs when failure occurs. Manually handling the procedures described above is difficult because of the size of the dataset and also because of the distributed resource environment. Therefore an efficient scientific workflow management system is needed, and various options will be discussed in Section 3.6.

3.3 Solver: SPECFEM3D_GLOBE

3.3.1 Overview and programming approach

Our seismic inversion workflow includes many parts, each of them implemented based on a different software package. The most computationally expensive part involves the solver **SPECFEM3D_GLOBE**, a spectral-element code capable of modeling seismic wave propagation using fully unstructured hexahedral meshes of 3D Earth models of essentially arbitrary complexity. Capabilities for its application in adjoint tomography are extensively illustrated in [101]. Table ?? outlines the importance of the solver relatively to other parts of the workflow for a shortest period of 17 s. As the number of earthquakes grows, the importance of having a computationally efficient solver to perform both forward and adjoint simulations becomes clear.

At the top level, **SPECFEM3D_GLOBE** is parallelized using MPI. The parallelization extensively relies on the analytical decomposition of a cubed-sphere mesh, splitting the mesh into partitions with close-to perfect load balancing and assigning a single partition to a single MPI process. This coarse domain decomposition parallelism may even include a finer level of parallelism inside each domain.

To take advantage of architectures of modern processors, in particular multicore CPUs and hardware accelerators such as GPUs, a finer level of parallelization is added to each MPI process. For computations on multicore CPU clusters, partial OpenMP support and vectorization has recently been added by Tsuboi et al. [136].

The **SPECFEM** software suite has been running on CUDA-enabled GPUs since 2009 [58]. It has continuously been adapted to take advantage of advances in NVIDIA GPUs [57, 106].

With the advent of heterogeneous supercomputers, our code base —as for many other applications— has become increasingly complex. Due to a relatively large user base and the variety of targeted systems, several code paths have to be maintained. The most important issue is to ensure that similar capabilities are available, regardless of the system. Another matter is to provide the user with optimized software.

Our solution has been to use the BOAST [22] transpiler to generate both CUDA and OpenCL kernels. The performance of these BOAST-generated kernels is very close to those implemented directly in CUDA, and provides code optimized for various NVIDIA GPU generations.

On the one hand, because **SPECFEM3D_GLOBE** strives to be a tool capable of solving unexplored geophysical problems, most of it is written by geophysicists. On the other hand, BOAST provides the programmer with a Ruby-based domain specific language (DSL), an unfamiliar language for most of our developers. This implies that while BOAST is equally capable of generating Fortran or C code, we maintain the original Fortran code as the reference source for CPU execution.

In the future, and in particular for the next generation heterogeneous supercomputers, it will be interesting to investigate directive-based approaches. This is increasingly true with accelerator support becoming more mature in OpenMP 4. If performance is close to hand written code, it will certainly be the solution of choice toward a portable, geophysicist-friendly code base.

3.3.2 Scalability and Benchmarking results

During a large-scale inversion, the proportion of computational time spent to simulate wave propagation mandates the solver to be performant and to scale well. Figure 3.2 shows SPECFEM3D_GLOBE strong scaling results for simulations running on multiple GPUs with a shortest period of 9 s. It demonstrates that very close to ideal efficiency can be achieved with a minimum size of about 100 MB of data per GPU. Thus, the code exhibits excellent scalability and can be run with almost ideal code performance in part because communications are almost entirely overlapped with calculations. Also note that the average elapsed calculation time per time-step is inversely proportional to the number of GPUs whether one uses a single MPI process per GPU or two MPI processes. This indicates that we can run multiple MPI processes on a single GPU without loss of performance. Depending on the number of simultaneous seismic events that we want to simulate and the expected maximum time-to-solution, these benchmarks help us select both the optimal number of GPUs and the organization of the MPI tasks across them. Scalability improves as the scale of the simulation becomes larger and larger. Though scalability performance at the lowest resolution (27 s) is not optimal (Figures 3.4 and 3.5), as the resolution increases to 9 s scalability performance is very close to ideal (Figures 3.2 and 3.8). It should also be admitted that as the number of MPI tasks used in the simulation increases —though scalability performance is not affected—the overall performance of each GPU node will be

slightly decreased. This is because communications between MPI processes on each node will slightly slow down the computation.

Figure 3.3 shows **SPECFEM3D_GLOBE** weak scaling test results for an increasing problem size while keeping the work load for each MPI process almost the same. Weak scaling tests are a bit unusual for **SPECFEM3D_GLOBE**. What we do is find a setup where slices will have more or less the same number of elements, then correct the timing by dividing the actual number of elements per slice and multiply with the setup which we take as a reference. It can be observed from the weak scaling plot that parallel efficiency for GPU simulations is excellent and scales within 95% of the ideal runtimes across all benchmark sizes. Comparing weak scaling performances between GPU and CPU-only simulations on a Titan node, i.e., a K20x GPU (Kepler) versus 16 CPU-cores (AMD Interlagos), we see a speedup factor of the GPU simulations of $\sim 18x$ for the chosen mesh sizes. For high-end Intel Xeons microprocessor or IBM Power microprocessor, the speedup factor of the GPU simulation may not be as high as 18x. To make **SPECFEM3D_GLOBE** ready for next-generation supercomputers, e.g., GPU-based machines with high-end microprocessors, continuous work should be carried out in order to maintain a high speedup factor for GPU simulations. Our scaling results indicate that asynchronous message passing is nearly perfect in hiding network latency on Titan. Note that this becomes more of a challenge for smaller mesh sizes, where the percentage of outer elements increases compared to inner elements, but such small meshes are never used in practice.

Next, we discuss scaling results for low- and high-resolution simulations. We anticipate that the scalability of low-resolution simulations will be worse, since the computing resources of each node will not be effectively used and MPI communication costs will take up a larger percentage of the total computation time. An additional issue is that accurate calculation of the gradient of the misfit function requires full attenuation. This involves storage of snapshots of the forward wavefield which are

read back during the adjoint simulation, leading to increased I/O. We expect this additional I/O to adversely affect performance.

Figures 3.4 and 3.5 show strong scaling tests for a low-resolution model (minimum period of 27 s) with and without full attenuation, respectively. In each figure, the two diagrams show the scaling results for 1 and 2 MPI tasks per GPU node. The scalability does not change as the number of MPI tasks increases. However, when the number of GPU tasks increases from 1 to 2, the processing time per time step doubles. The scalability does not change whether or not we are considering full attenuation. As anticipated, when considering full attenuation the processing time per time step is a bit longer than when not considering full attenuation. Table ?? shows a comparison of processing time per time step in two different cases for a different number of MPI processes. Processing time with full attenuation is a bit longer than without.

Figures 3.6 and 3.7 show strong scaling tests for a medium resolution model (minimum period of 17 s) in two different situations: with and without full attenuation. The scalability in the two cases is similar, except that when considering full attenuation the scalability is a bit better than that of the opposite case. The number of MPI processes still does not affect scalability but is inversely proportional to computational performance. Compared to the 27 s case, the 17 s simulation shows scalability. Processing efficiency with full attenuation is also a bit lower than that of without full attenuation, as shown in table ??.

Figure 3.2 shows strong scaling tests for 9 s resolution with full attenuation. Figure 3.8 is the same test without full attenuation. It is obvious that scalability is close to ideal in both cases. Comparing the actual processing time for the two cases, as shown in Table ??, we conclude again that full attenuation causes slightly lower efficiency.

We compare the processing time per time step for different output data formats, including ASDF, our newly design modern seismic data file format (see Section 3.5).

Comparison of processing time per time step with and without full attenuation (27 s resolution).

No. of MPI processes	24	96	150	600	2400
With full attenuation	0.025	0.00679	0.00462	0.00174	0.00148
Without full attenuation	0.025	0.00678	0.00462	0.00171	0.00135

Comparison of processing time per time step with and without full attenuation (17 s

No. of MPI processes	96	384	1536	6144
With full attenuation	0.0194	0.00542	0.0226	0.0189
Without full attenuation	0.0193	0.00490	0.0023	0.00171

Whether or not we use ASDF, the processing time per time step is almost unaffected. This observation is encouraging, because when we enjoy the benefits of ASDF we do not lose the superb scalability performance of the code. We also compare scalability performance with respect to the number of receivers. We find that the number of receivers does not influence scalability of **SPECFEM3D_GLOBE**. This indicates that as the global seismographic network becomes denser and denser, scalability will not degrade.

In order to prepare **SPECFEM3D_GLOBE** for the next generation supercomputers, e.g., ‘Summit’, code improvements should be done to ensure a linear speed up of GPU simulations to at least 20 % of current Titan nodes ($\sim 3,600$ MPI processes) for both high-resolution and medium-resolution simulations. High-resolution simulations (~ 9 s) have already demonstrated perfect scalability to at least 5,400 nodes, which ensures a stable application for the intermediate future.

Comparison of processing time per time step with and without full attenuation (9 s

No. of MPI processes	600	1350	2400	5400
With full attenuation	0.0175	0.00848	0.0051	0.00233
Without full attenuation	0.017	0.00827	0.005	0.00229

3.4 Optimizing I/O for computational data

The workflow sketched in the previous sections deals with two main types of data, namely, seismic and computational data. In this section, we focus on computational data.

Computational data are, in general, characterized by discretization and representation of the scientific problem. In our case, these are mesh and model files, and data sensitivity kernels, which are the output of SPECFEM3D and **SPECFEM3D_GLOBE** used in the post-processing stage. They are shown in blue and green in the workflow chart in Figure 3.1. The size of these files depends on the spatial and temporal resolutions. For instance, a transversely isotropic global adjoint simulation (100 minutes long seismograms at a resolution going down to 27 s with 1300 receivers) reads 49 GB of computational data and writes out 8 GB of data for adjoint data sensitivity kernels. When increasing the resolution of the simulations by going down to a shortest period of 9 s, all these numbers should be multiplied by 3^3 , yielding about 1.3 TB of computational data. In practice, the number of events drastically reduces the simulation size we are able to reach, even on the latest supercomputers. This problem becomes even more prevailing when more realistic physics is used. To compute anelastic sensitivity kernels with full attenuation, a parsimonious disk storage technique is introduced [59]. It avoids instabilities that occur when time-reversing dissipative wave propagation simulations. In practice, this leads to a dramatic increase for I/O, as outlined in Figure 3.9.

3.4.1 Parallel file formats and I/O libraries for scientific computing

Although I/O libraries and file systems must be considered together to improve I/O techniques, only I/O libraries are exposed to the scientific programmer. In what follows, we try to focus our efforts on a more library-oriented approach.

The POSIX standard defines an I/O interface designed for sequential processing. Its single *stream of bytes* approach is well known to poorly scale on distributed memory machines. Extensive studies tried to extend this standard [141], most of the time in combination with research on parallel file systems.

When considering parallel software, developer choices have a great impact on how I/O calls perform. There are two simple ways to use the POSIX I/O interface in such parallel software:

- The most straightforward method is having separate files for each task. Eventually, subsequent processing can be applied on subsets of files to gather data. For a large number of tasks, this approach leads to a large number of files, potentially causing contention on the file system metadata servers.
- Each process sends its data to a set of master MPI tasks in charge of writing data to disk. Conversely, data can be read from disk by a subset of MPI tasks and then distributed among all MPI tasks. This approach has a few drawbacks. In particular, nodes running master tasks might run out of memory if the number of scattered/gathered data is high. Moreover, network traffic is likely to reach high levels, slowing down the execution.

Over the past decades, a number of techniques has been developed and incorporated into libraries to ease writing —sometimes large amounts of data— to disk. Our goal is not to provide a full description of parallel I/O techniques and libraries evolution. For this purpose, the reader may consult Schikuta and Vanek [114] or Liu

et al. [71]. However, we do believe that understanding where the need for simple and generic APIs comes from helps determine a solution satisfying our needs. In what follows, we consider distributed memory systems and software programmed using MPI, to date the most common paradigm to address large scientific simulations on modern HPC systems.

The first version of MPI did not define a dedicated I/O API. Parallel I/O libraries were often developed to match particular architectural or applicative requirements. For instance, ChemIo [96] was developed as an interface for chemistry applications and SOLAR [129] to accelerate writing dense out-of-core matrices. Thakur et al. developed ADIO (Abstract-Device interface for parallel I/O) [126] to fill the gap between various parallel filesystems and parallel I/O libraries. This work ultimately lead to ROMIO [127], one of the most popular MPI-IO libraries that was later integrated as a component into the well-known MPICH2 library. While MPI-2 introduced support for parallel I/O with the MPI-I/O approach, using it in large scientific code is not always straightforward. As a matter of fact, it is a low level API writing raw data to files and demands a concerted effort from the scientific programmer.

Scientific software can benefit from libraries wrapping complexity into a higher level function set. Hence, libraries accommodating metadata were designed to ease further exploitation of produced data. Two of the most popular parallel I-O libraries embedding metadata are netCDF [68] and HDF5 [52]. Both of them provide a parallel interface. While netCDF is principally oriented toward the storage of arrays —the most common scientific data structure— HDF5 is more versatile and based on user-defined data structures. The distinction between these two libraries became blurrier as netCDF, starting from version 4, is implemented through HDF5. Metadata allow further analysis on potentially large datasets in providing the necessary information to fetch values of interest. A significant number of well established tools are based on this format, showing their durability.

An alternative is the ADIOS library [71] released by ORNL. Compared to netCDF and HDF5, it works on simpler data structures since its main focus is parallel performance. Besides metadata availability similar to the other formats previously mentioned, it also lets users change the transport method to target the most efficient I/O method for a particular system or platform. A set of optimizations is embedded in so called *transport methods*. I/O experts have the option to develop new transport methods while scientific developers have to pick one matching the platform, their software and their simulation case. In particular, transport methods describe the file pattern, that is to say, if a number of MPI tasks write data to the same number of files, to a smaller number of files or to a single file. The underlying optimizations contain methods such as aggregation, buffering, and chunking, and are transparent to the user.

Two APIs are available, one POSIX-like API with a reduced number of functions and one XML API which is not as flexible as the regular API but allows one to keep I/O separated from the main program.

From a user perspective, reading data is very similar to writing them. It must be noted that it is possible to read and write data form a *staging* memory area, thus limiting disk access when produced data are consumed right away.

Although the ADIOS library needs to be improved by providing optimizations tuned for a larger number of file systems (GPFS for instance), its architecture allows domain scientists to focus on the actual problem.

Liu et al. [71] demonstrated excellent improvements in terms of I/O speed. For instance, both S3D, software simulating reactive turbulent flows, and PMCL3D, a finite-difference based software package simulating wave propagation, show a 10 fold improvement when switching from MPI-IO to ADIOS. They managed to write at a 30 GB/s rate when using 96K MPI tasks for S3D and 30K MPI tasks for PMCL3D.

3.4.2 Integrating parallel I/O in adjoint-based seismic workflows

Computational data, in general, do not require complex metadata since they are well structured within numerical solvers. In legacy `SPECFEM3D_GLOBE`, the way computational data were written to disk was not problematic on local clusters for smaller size scientific problems (e.g., regional- or continental-scale wave propagation, small seismic data sets, etc.). However, to run simulations more efficiently on HPC systems for more challenging problems, such as global adjoint tomography or increased resolution regional- and exploration-scale tomography, we needed to revise the way the solver handles computational data. In the previous version of the `SPECFEM3D` packages, for each variable or set of closely related variables, a file was created for each MPI process. The number of files, for a single seismic event, was proportional to the number of MPI processes P . For a full iteration of the workflow the number of files was $\mathcal{O}(P.N_s)$. Accessing these files during large-scale simulations did not only have an impact on performance, but also on the filesystem due to heavy I/O traffic. This is because of the difficulty for the file system metadata server to handle all requests to create the whole set of files. The new implementation uses ADIOS to limit the number of files accessed during reading and writing of computational data, independent of the number of processes, that is $\mathcal{O}(N_s)$. Since writing a simple file is also a potential bottleneck due to lock contention, we are sometimes asked to change the transport method to output a limited number of files. This is mostly invisible to the code user as these files are output as subfiles that are part of a single file. As an additional benefit, using ADIOS, HDF5 or netCDF let us define readers for popular visualization tools, such as Paraview and VisIt.

Tests have been run to assess the I/O speed to write models in `SPECFEM3D_GLOBE` on the Titan supercomputer. The test case has been chosen to match the number of processes and to result in the same amount of I/O as the complete simulation for our

Bandwidth for SPECFEM3D_GLOBE output using the ADIOS MPI_AGGREGATE transport method for mesh using 24,576 MPI tasks. Results are presented both for the old (Spider) and new (Atlas) OLCF filesystems. Numbers for different regions outline that large files benefit the most from use of the ADIOS library.

Mesh Region	Ouput Size (GB)	Spider (GB/s)	Atlas (GB/s)
Crust-Mantle	2,548	14.3	40.6
Outer Core	317	7.4	8.47
Inner Core	177	4.8	7.6

253 earthquake database. This results in more than 6 millions (6×1007^2) spectral elements on the Earth’s surface, processed through 24, 576 MPI tasks. ADIOS experts at ORNL indicated that the preferred way to get I/O performance is to use the MPI_AGGREGATE transport method. This method is carefully tuned for large runs on Lustre filesystems. Suitable parameters for this transport method were given by ORNL ADIOS experts in order to match both OLCF Spider file system characteristics and the test case parameters. A single ADIOS writer process was associated with 256 Object Server Targets (OST), 32 MPI tasks running on 2 Titan nodes. The test was later reproduced on the new OLCF Atlas file system. Results in Table ?? show that switching from Spider to Atlas brings a significant improvement in terms of I/O bandwidth. Moreover, in this case, the peak bandwidth on the Spider filesystem is 16.9 GB/s, while on the Atlas filesystem the peak bandwidth is 51.5 GB/s. This is likely to be beneficial for our research, especially when the spatial resolution is increased, yielding large data volumes on a high number of nodes.

3.5 A Modern Approach to Seismic Data: Efficiency and Reproducibility

Seismology is a science driven by observing, modeling, and understanding data. In recent years, large volumes of high-quality seismic data are becoming more and more easily accessible through the dramatic growth of seismic networks. Together with the

development of modern compute platforms, both large-scale seismic simulations and data processing can be done very efficiently. However, the seismological community is not yet ready to embrace the era of big data. Most seismic data formats and processing tools were developed more than a decade ago and are becoming obsolete in many aspects. In this chapter, we present our thoughts and efforts in bringing modernity into the realm.

The very basic unit of seismic data is the seismogram, which is a time series of ground motion recorded by a seismometer during an earthquake. Most seismometers on land are able to record 3-component data: one vertical component, and two horizontal components perpendicular to each other(usually east and north) while seismometers in the ocean vary, some are equipped with a water pressure sensor and others record 3-component displacement of the seabed (an Ocean Bottom Seismometers). Seismometers are recording 7/24 and data are archived at data centers. The data we are primarily interested in are 3-hour time windows after an earthquake, during which time seismic waves propagate inside the earth and gradually damp out.

3.5.1 Legacy

Most earthquake seismologists are familiar with Seismic Analysis Code (SAC, see [49]), a general-purpose program designed for the study of time series. It provides basic analysis capabilities, including general arithmetic operations, Fourier transforms, filtering, signal stacking, interpolation and etc., which fit the general requirements of researchers.

Alongside the software package, SAC also defines a data format, which has been widely used by seismologists over the last few decades. In the SAC data format, each waveform (time series) is stored as a separate data file, containing a fixed length header section to store metadata, including time and location information), followed by the data section (the actual time series). Thus, for one earthquakes recorded

by 2,000 seismometers, one would expect 6,000 independent SAC files. The main reason SAC is popular within the seismological community is its ease of use and its interactive command line tools. Even though functionality is limited, SAC covers the most frequent needs of seismologists. For example, visualizing seismograms is very easy in SAC and is frequently used to check the effect of operations applied to data.

However, things are evolving quickly as more and more seismometers are installed. For a single network, the number of seismometers can go easily beyond 1,000, leading to sizable datasets. Thus, SAC and its associated format is no longer a good choice for the following reasons.

- It has limited non-programmable functionalities. SAC tools have to be invoked by system calls (shell scripts) and the lack of APIs for programming languages, such as C and Fortran, makes it difficult to customize workflows.
- The SAC data format only stores one waveform per file. Given 5,000 earthquakes and 2,000 stations for each earthquake, $3 * 10^7$ SAC files have to be generated and stored. Reading or writing such a large number of files is highly inefficient,
- The header in the SAC data format is very limited, with only a fixed number of pre-defined slots to store metadata. However, a modern data format should be flexible enough for users to define metadata relevant to the problem they are solving. Imposing pre-defined offsets in bytes to access information is a recipe for disaster.
- Station information, which contains instrument response information, is stored in separate files. This approach increases the number of files to deal with and the possibility of making errors. Having the ability to store station information along with the waveform data greatly reduce the chances of mistakes.

3.5.2 The Adaptable Seismic Data Format

We looked for existing solutions lacking the drawbacks listed in the previous paragraph. Because introducing a new data format should ideally be avoided, the seismological community has been postponing the definition of more modern approaches. We believe that the advantage of a new data format are significant enough to quickly outweigh the initial difficulties of switching to a new format. We identify five key issues that the new data format must resolve.

- **Robustness and stability:** The data format should be stable enough to be used on large datasets while ensuring data integrity and the correctness of scientific results.
- **Efficiency:** The data format should be exploitable by efficient, parallel tools.
- **Data Organization:** Different types of data (waveform, source & station information, derived data types) should be grouped at certain levels to perform a variety of tasks. The data should be self-describing so no extra effort is needed to understand the data.
- **Reproducibility:** A critical aspect of science is the ability to reproduce results. A modern data format should facilitate and encourage this.
- **Mining and Visualization of data:** Data could be queried and visualized anytime in an easy manner.

The Adaptable Seismic Data Format (ASDF) [61] was introduced to solve these issues. Using HDF5 at its most basic level, it organizes its data in a hierarchical structure inside a container —in a simplified manner a container can be pictured as a file system within a file.

HDF5 was chosen as the underlying data format for a variety of reasons. First, HDF5 has been used in a wide variety of scientific projects and has a rich and active

ecosystem of libraries and tools. It has a number of built-in data compression algorithms and data corruption tests in the form of check summing. Second, it also fulfills our hard requirement of being capable of parallel I/O with MPI [93, 52]. Besides, there is no need to worry about the endianness of data, which historically has been a big issue in seismology.

An ASDF file is roughly arranged in four sections, as follows.

1. Details about seismic events of any kind (earthquakes, mine blasts, rock falls, etc.) are stored in a QuakeML document.
2. Seismic waveforms are grouped seismic station along with meta information describing the station properties (a StationXML document).
3. Arbitrary data that cannot be understood as a seismic waveform are stored in the auxiliary data section.
4. Data history (provenance) is kept as a number of SEIS-PROV documents (an extension to W3C PROV).

Existing and established data formats and conventions are utilized wherever possible. This keeps large parts of ASDF conceptually simple, and delegates pieces of the development burden to existing efforts. The ASDF structure is summarized in Figure 3.10. With such a layout, every seismograms of a given earthquake can be naturally grouped into one ASDF file. Also, event information and station information are incorporated so no extra files have to be retrieved during processing.

Reproducibility is frequently discussed and widely recognized as a critical requirement of scientific results. In practice, it is a cumbersome goal to achieve and is frequently ignored. Provenance is the process of keeping track of and storing all constituents of information that were used to arrive at a certain result or at a particular piece of data. The main goal of storing provenance data directly in ASDF

is that scientists looking at data described by it should be able to tell what steps were taken to generate that particular piece of data. Each piece of waveform and auxiliary data within ASDF can optionally store provenance information in the form of a W3C PROV or SEIS-PROV document. Thus, such a file can be safely archived and exchanged with others, and information that led to a certain piece of it is readily available.

More details about ASDF may be found in [61].

3.5.3 Data Processing

Global adjoint tomography is ideal for the ASDF data format. First, the data volumes involved are massive, easily containing millions of seismograms. Second, it necessitates sophisticated processing to turn raw data into meaningful results. Here, we present a typical data processing workflow occurring in full seismic waveform inversions with adjoint techniques [135, 35, 122, 153]. The general idea also translates to other types of tomography (see [?] for a recent review).

To enable a physically meaningful comparison between observed and synthetic waveforms, time series need to be converted to the same units and filtered in a way that ensures a comparable spectral content. This includes standard processing steps like detrending, tapering, filtering, interpolating, deconvolving the instrument response, and others. Subsequently, time windows in which observed and simulated waveforms are sufficiently similar are selected and adjoint sources are constructed from the data within these windows, see Figure 5.4 for a graphical overview.

The following is an account of our experiences and compares a legacy workflow to one utilizing the ASDF format, demonstrating the latter’s clear advantages. Existing processing tools oftentimes work on pairs of SAC files, observed and synthetic seismic data for the same component and station, and loop over all seismic records associated with any given earthquake. Given the large number of seismic receivers

and earthquakes, the frequent read and write operations on a very large number of single files create severe I/O bottlenecks on modern compute platforms. The implementation centered around ASDF shows superior scalability for applications on high-performance computers: observed and synthetic seismograms of a single event are stored in only two ASDF files, resulting in a significantly reduced I/O load. What is more, it is beneficial to keep meta information in the same file. For example, one does not need to reach out for separate files that keep track of the stations' instrument information or files containing earthquake information, which greatly reduces the complexity of operations and the possibility of making mistakes. Last but not least, provenance information is kept to increase reproducibility and for future reference.

Other than the data format itself, the data processing workflow benefits from the extensive APIs provided by ASDF. ASDF is supported in the `SPECFEM3D_GLOBE` package [55]. Synthetic ASDF files are directly generated, meaning synthetic data can seamlessly be fed as an input into the workflow. To maximize performance, we rewrote our existing processing tools. A big drawback in the old versions was that codes were written in different languages and unable to communicate with each other easily. For example, the SAC package was used for signal processing and the Fortran based FLEXWIN program [79] for window selection. In the new version we treat tasks as individual components in a single cohesive workflow. Relying on the seismic analysis package ObsPy [8], we re-developed all workflow components in Python. Therefore, all components integrate with each other and stream data from one unit to the next. I/O only happens at the very beginning, when we read the seismogram into memory, and at the very end, when we write out the adjoint sources. All in all these changes empower us to increase the scale of our inversions—in terms of frequency content, number of earthquakes, and number of stations—and fully exploit modern computational platforms.

3.6 Bringing the Pieces Together: Workflow Management

The importance of a performant solver to simulate forward and adjoint wavefields is well understood and accepted. In our case, sustained efforts are being made to adapt and tune `SPECFEM3D_GLOBE` to newer architectures. One of the most significant benefits of this work is the ability to use GPU acceleration.

The ever increasing performance level of the wave simulation software goes along with rapidly growing data volumes. This offers new opportunities for improving our understanding of the physics and chemistry of Earth’s interior, but also brings new data management and workflow organization challenges.

Existing geoscience inversion workflows were designed for smaller scientific problems and simpler computational environments and suffer from I/O inefficiency, lack of fault tolerance, and inability to work in distributed resource environments. Workflow management challenges are by no mean limited to earthquake seismology, let alone to global adjoint tomography. In exploration seismology, streamers can contain sixty thousand hydrophones, and the number of shots can reach fifty thousand, requiring petabytes of storage. Even then, a crying lack of scalable seismic inversion software (outside of proprietary, closely-guarded oil industry codes) poses a continuing obstacle to robust and routine inversions. Given data volumes in the petabytes and compute time requirements in tens to hundreds of millions of core-hours, new workflow management strategies are needed.

This section starts with a discussion of some of the most widely used scientific workflow management system and solutions that have been brought in order to manage seismic workflow. We then expose the requirements for large-scale seismic inversions and the design of a solution. Finally, additional challenges are outlined.

3.6.1 Existing solutions

When researching which workflow engine would be the most appropriate for global adjoint tomography, the need to restrict the signification of the word *workflow* emerges. Indeed, workflow and workflow management have very different meanings depending on the application domain. While there is some degree of similarity between business and scientific workflows [76], we will exclusively consider tools focusing on the latter.

Even then, the number of tools available to manage scientific workflows is large. What follows discusses the main options and is by no means exhaustive. For more in depth reviews, the reader should consult [150, 50, 23].

Focusing on usability by domain scientists, we also restrict ourselves to tools providing a higher level of abstraction, and forbid ourselves to directly work with powerful but complex tools such as HTCondor [125].

From an user experience point of view, and forgetting about technical details, two competing approaches are available. The first one relies on graphical user interfaces (GUI). Examples include Kepler [2], Taverna [144], and Triana [124]. The second approach involves scripting and is implemented by a number of workflow management systems, such as Swift [143], Pegasus [27], or Radical-Ensemble [137]. Scripting is particularly well suited to scientists familiar with both HPC systems and software development. It allows for fast prototyping and flexible definition of workflows. As such, it provide users with powerful exploratory tools.

In the field of geophysics, fully managed workflows seem to be the exception rather than the norm. Of course, proprietary software geared toward the oil industry exists, but their closed nature forbids us to adapt and use them to perform global adjoint tomography. Most of the daily research and production computational work rely on a mixture of hand-written scripts steering more computationally expensive software such as solvers and data processing packages. Each scientist, or group of scientists, has their own set of scripts embedding a fair amount of specific knowledge about the

system they are running on. Needless to say, such an approach is nonportable and error prone. Attempts to provided a more streamlined way of running these hand-written scripts have been made. Starting from the ever increasing importance of reproducible research [36], Fomel et al. developed Madagascar [37], where dependencies between tasks are managed with SCons, a software build tool similar in essence to GNU Make.

As science workflows, computer systems, and workflow engines grow more mature and complex, inter-disciplinary collaboration is mandatory to bring seismic simulation and processing to the next level. One major exception to the lack of fully managed seismic workflows is CyberShake [46], which aims is to compute probabilistic seismic hazard maps. CyberShake developers have been experimenting and using a number of workflow managers to schedule computations on a wide range of HPC centers. Among the workflow managers CyberShake has been run under the control of are Condor, Globus, Pegasus [15], and Radical-Pilot.

The Hadoop ecosystem, a popular paradigm to perform distributed computations, is worth mentioning. It has been used in production environments for many years by the industry and is gaining traction in scientific computing, especially to solve data-driven problems. For many scientific problems relying on HPC systems, involving large, multi-nodes simulations, it has so far remained an exotic approach. The frontier tends to blur, thanks to approaches such as Yarn. A non critical, but interesting feature for a suitable workflow engine is to be able to address both Hadoop and HPC systems. This is for example the case for some of Radical-Pilot [75] most recent developments.

3.6.2 Adjoint tomography workflow management

As each problem and domain has widely different requirements, we will focus on ad-hoc solutions suited to large-scale seismic inversions on leadership-class resources, such as the ones provided by the DOE computing centers.

The first requirement for large-scale seismic inversions is performance along with efficiency. Indeed, the number of core-hours required to perform a global inversion being in the hundreds of millions, a suitable workflow management system needs to ensure that a minimum amount of compute cycles are wasted. Large compute centers have requirements on the size of jobs that are allowed to run; as they are primarily designed to accommodate computations that would not fit any other place. While elementary computations of a seismic inversion do not fulfill this condition, the large number of simulations involved does. This means that in order to match the queueing requirements, smaller-scale jobs have to be bundled in batches. Ideally, the workflow management system should be in charge of such accounting matters. This is, for instance, one of the features offered by the Pilot approach.

A second condition is the ability to execute in a relatively heterogeneous environment. Here, the concept of heterogeneous environment is understood differently than for its more traditional grid computing definition. Each elementary part of the workflow is run on an homogenous machine, while different parts are not. For instance, for our current global inversions, Titan is used to run simulations while Rhea, an Intel-based commodity cluster, is used to process data. Appropriate resources are also used for visualizing data and data transfer.

Another reason to run seismic inversion under a workflow management system is reliability. On large systems, the mean time between failures [16] is reduced compared to smaller-scale systems. This is specially true for systems, such as the ones provided by DOE facilities, that are on the edge of what is technically feasible. Job failures due to hardware and software errors as well as corrupted data do happen. Hand-tracking

causes of such failures when dealing with large data sets and numerous simulations is time consuming and error prone. The ability for a workflow to account for this failures and eventually relaunch jobs is become even more critical as we are the number of earthquake we assimilate data from raise.

It is equally important to keep the user in mind and to follow the science problem logic. The typical user is a domain scientist with experience running simulations on large-scale supercomputers. While the computer science details must be hidden from such users, they are usually fluent in developing scripts, allowing some level of technical details to be exposed to them. For this scenario, scripting is particularly well adapted as it provides a dynamic environment to define and iteratively improve workflows. This flexibility is a very desirable feature for our global tomographic inversion, where the numerical algorithmic strategy needs to be adapted according to the decrease in the misfit function and the lessons learned performing previous iterations. Domain logic is also better accommodated by a flexible ad-hoc approach. From experience, concepts such as direct acyclic graphs (DAG) are, surprisingly enough, difficult to convey to domain scientists. It is important to note that the previous remarks are specific to large-scale exploratory computations by power-users on leadership systems. A better approach for the broader community might very well be such that it includes a graphical interface and does not require any knowledge of the underlying system.

Additionally, a desirable feature is workflow portability. As newer distributed paradigms, such has Hadoop, are gaining traction across the scientific community, being able to run part of the workflow, most likely data processing, on such infrastructures would undoubtedly benefit us.

3.6.3 Moving toward fully managed workflows

From this panorama of existing workflow management systems and requirements, we can see what a suitable solution for large-scale seismic inversion is.

Past experience on defining scripts ranging from simple bash scripts to sophisticated modular python scripts taught us the need to separate the application domain from the engine running the workflow. This has several benefits, the most immediate being able to take advantages of the most recent advances in the application domain and in workflow science. Decoupling is also a good software engineering practice, as each part can be implemented, tested, and maintained independently. For instance, the application domain pieces might be used as standalone applications or plugged in different workflow engines. Similarly, the workflow engine can evolve to exhibit common patterns for a class of problems and thus be reused. However, this does not mean that each side should not be designed with the other one in mind. Indeed, complex inverse workflows impose significantly more complex and sophisticated resource management and coordination requirements than simple parameter sweeps in that they support varying degrees of coupling between the ensemble members, such as global or partial synchronization. In addition, all parts of the workflow must successfully complete to yield a meaningful scientific result.

From the previous requirements, and after surveying a few workflow management systems, it appears that two of them are particularly well suited to our needs: Pegasus and Radical-Pilot.

The first step to be able to take advantages of such tools is to ensure the most desired separation between the science software and the workflow management system. Due to the number of steps involved in processing seismic data (as explained in Section 3.5) and to create adjoint sources, we picked this stage of the inversion workflow as the first sub-workflow to implement.

An important preparation has been to define clear interfaces for each of the executables. That is, each executable must clearly define its inputs and outputs without assumptions such as their relative location. Different parts can then be assembled, either as a DAG (in the case of Pegasus), or as an ad-hoc dependency description (in the case of Radical-Pilot). We experimented with both, and consideration over the end-user experience oriented our choice toward the latter.

To operate, workflow engines store information about job statuses along with data useful to their internal machinery. Information of interest to the scientist and to the science workflow, regardless of the engine, also need to be tracked. We have chosen to have information relevant to our pre-processing workflow stored in an SQLite database. This database is regularly polled by the workflow engine to dynamically create and launch jobs along with relevant parameters. Its purpose is two-fold: to feed the workflow engine and to keep track of the assimilated data. The process is described in Figure 3.12.

For now, the workflow engine is rudimentary and relies on Radical-SAGA to launch jobs. Adapting it to a more complete solution, similar to Ensemble-MD, is ongoing. Relying on Radical-Pilot, patterns common to seismic inversions would be exhibited and released to the public.

3.6.4 Additional challenges

As we progress through the implementation and the understanding of automated seismic inversion workflows, several challenges worth mentioning will need to be taken care of. Taking full advantage of large-scale resources requires tight software integration. For instance, some next generation supercomputers will have burst buffers allowing staging of data between computing steps. While this is a promise of greater performance, this is problematic from a workflow management perspective. Indeed, such techniques disrupt the control flow and defy the purpose of a workflow engine.

How to solve this is an open question. A second challenge comes from the desire of scientists to visualize intermediate data. This is motivated by the will to take informed decisions to steer the inversion process in the best direction possible. This calls for a level of interactivity that interfaces well with an automated approach.

It is equally important to start thinking from the beginning about the general geophysicist population and how they can benefit from developments made for large-scale inversions. We are confident that the pattern defining approach of the Ensemble toolkits, along with the system-agnostic Radical-SAGA backend, is a step toward dissemination.

3.7 Software Practices

The number and complexity of the software packages that we have developed, in order to be able to perform exascale seismic inversions, have required us to adopt more rigorous software practices.

Compared to professional software development teams, scientific software developers face particular issues. First, they are often a group of independent researchers that are in different physical locations. Second, there is often a large range in the level of programming experience. To address these issues, we implemented a simple collaborative workflow based on modern software development techniques, such as Agile development and Continuous Integration/Continuous Development.

The two main goals of this workflow are to facilitate communication between the developers, and to ensure that new software developments meet some agreed upon quality criteria before being added to the common code base. In practice, we have implemented this workflow using the tools provided by the GitHub platform, and the automatic testing frameworks Buildbot, Jenkins and Travis CI.

As illustrated in Figure ??, our collaborative software development practice is organized around three Git repositories.

The central repository: where the code is shared among developers, and where users can download releases of the code.

Forks of the central repository: where each developer can post their changes to be tested by Buildbot, before being committed into the central repository.

Local clones: where each developer builds his/her changes.

The first two repositories are hosted on the Computational Infrastructure for Geodynamics (CIG) GitHub organization. The third repository is on the developers desktop or laptop.

An essential part of our workflow is the differentiation between production and development code: the production code is in a Git branch called `master`, and the development code is in a branch called `devel`. The code in the `master` branch is intended for users that are only interested in running the code, while the `devel` branch is intended for code developers. The changes to the code are first committed to the `devel` branch. Development code is transferred to the `master` branch only after extensive testing.

A fundamental rule of our workflow is that code changes can only be committed to the `devel` branch of the central repository through a pull-request. This provides us with two important features: first it allows us to test the changes before they are committed to the central repository, and, second, it sends an e-mail notification to the group of developers. The notification to the developers is important because it lets them review the changes before they are committed to the shared repository.

We have two distinct roles within our developer's community: *code maintainer* and *code developer*. The code maintainer role consists of accepting the code changes proposed by the developers. The code maintainers have push/pull (or read/write)

permissions to the central repository, while the developers only have pull (or read only) permissions. In addition, code maintainers cannot accept their own source code changes.

Assuming that a developer already has a clone of the central repository on his/her local machine, a typical workflow for committing new code developments to the central repository is as follows (see Figure ??).

1. The developer pushes his/her changes to his/her fork on GitHub.
2. He/she opens a pull-request.
3. Opening a pull-request triggers automatic testing of the changes.
4. The maintainers and developers are notified of the results of the tests. If the changes failed the tests, then the developer needs to fix the problems and follow the steps 1 through 4, if they pass the test, go to step 5.
5. Before they can be committed in the central repository, the code needs to be reviewed by other developers.
6. The maintainers accept the changes and the new code is committed to the `develop` branch of the central repository.

For this workflow to be successful, it is crucial to have a carefully designed test suite. We use three types of tests for our codes.

Compilation tests: they consist in looping through all the available compiling options (e.g. OpenMP, MPI, CUDA) and using different compilers (GCC and Intel compilers).

Unit tests: they tests individual functions by checking the output for some predefined set of input parameters.

Functional tests: in our case, functional testing refers to the testing of the a set of features of the code. Concretely, we run full examples for which we compare the computed seismograms with some precomputed reference seismograms.

The compilation, unit, and some functional tests can be all done within 15 min of opening the pull-request. These quick tests are the only ones that are done before a pull-request is accepted. Other tests, that take longer to execute, are run on daily and weekly bases. If these tests fail, then some changes need to be reverted, but at least the changes are recent and there are few of them, so it is easy to find what needs to be fixed; we failed but we failed early.

In conclusion, our experience over the past three years has shown this software development workflow to balance simplicity and effectiveness. Its simplicity has made it easy to adopt for both experienced and new developers, without hindering new developments. Its effectiveness at detecting problems early has ensured the stability of our central repository. In addition, by making the changes to the code more visible, this workflow has improved the communication within our developer’s community and enabled the release of increasingly more sophisticated software.

3.8 Conclusion

We have outlined some of the difficulties arising in modern computational seismology. They stem from the need to simultaneously handle large data sets and increased Earth model resolution. This is even more true when performing large-scale inversions at leadership supercomputer centers. Even though the data volumes might not be comparable to what is commonly referred as “big data”, data and workflow management are creating performance and filesystem issues on supercomputers.

In order to be able to pursue our scientific goals on the next-generation supercomputers we have devised several strategies. For heavy computational I/O we now

rely on ADIOS. The developers of ADIOS have either tight links with US computing centers or are part of them. We rely on the improvements they bring to the so-called transport method to continue getting a satisfying level of performance. To accommodate the attenuation snapshots required for anelastic simulations, several additional strategies might need to be developed as the specificities of next-generation machine are unveiled. We can think about overlapping I/O calls with computations, or using on-node non-volatile memory (NVMe) as a burst-buffer.

Interestingly enough, the focus of seismic inversion is shifting from pure computations to a more balanced approach, where data is a first-class citizen, seen as equally important as computations. Using a modern file format, such as ASDF, including comprehensive metadata not only helps increase computational performance, but also ensures reproducibility, and in the long term brings a standard to seismic and computational data which will ultimately increase collaboration within the seismological community.

The sheer number of data and simulations is becoming increasing difficult to manage. Workflow management has been sparsely used within the seismological community and, to the best of our knowledge, not in production-scale inversions. This last sentence might be controversial, but, in our opinion, to be considered as managed, a workflow must provide the user with automation going beyond a simple dependency description. Workflow management is an exciting challenge, particularly with the present effort of infrastructure designers (both hardware and software) to bring *HPC* and *Big Data* systems closer.

Many other challenges remain and keep arising during our journey to perform global adjoint tomography problems on exascale systems. Some of the more thrilling include exploring deep-learning methods to assimilate data in a more sensible fashion, as well as newer visualization techniques allowing scientists to discover features in global Earth models with unprecedented levels of detail.

Acknowledgement

This research used resources of the Oak Ridge Leadership Computing Facility at Oak Ridge National Laboratory, which is supported by the Office of Science of the U.S. Department of Energy under Contract No. DE-AC05-00OR22725.

Additional computational resources were provided by the Princeton Institute for Computational Science & Engineering and the Princeton University Office of Information Technology Research Computing department.

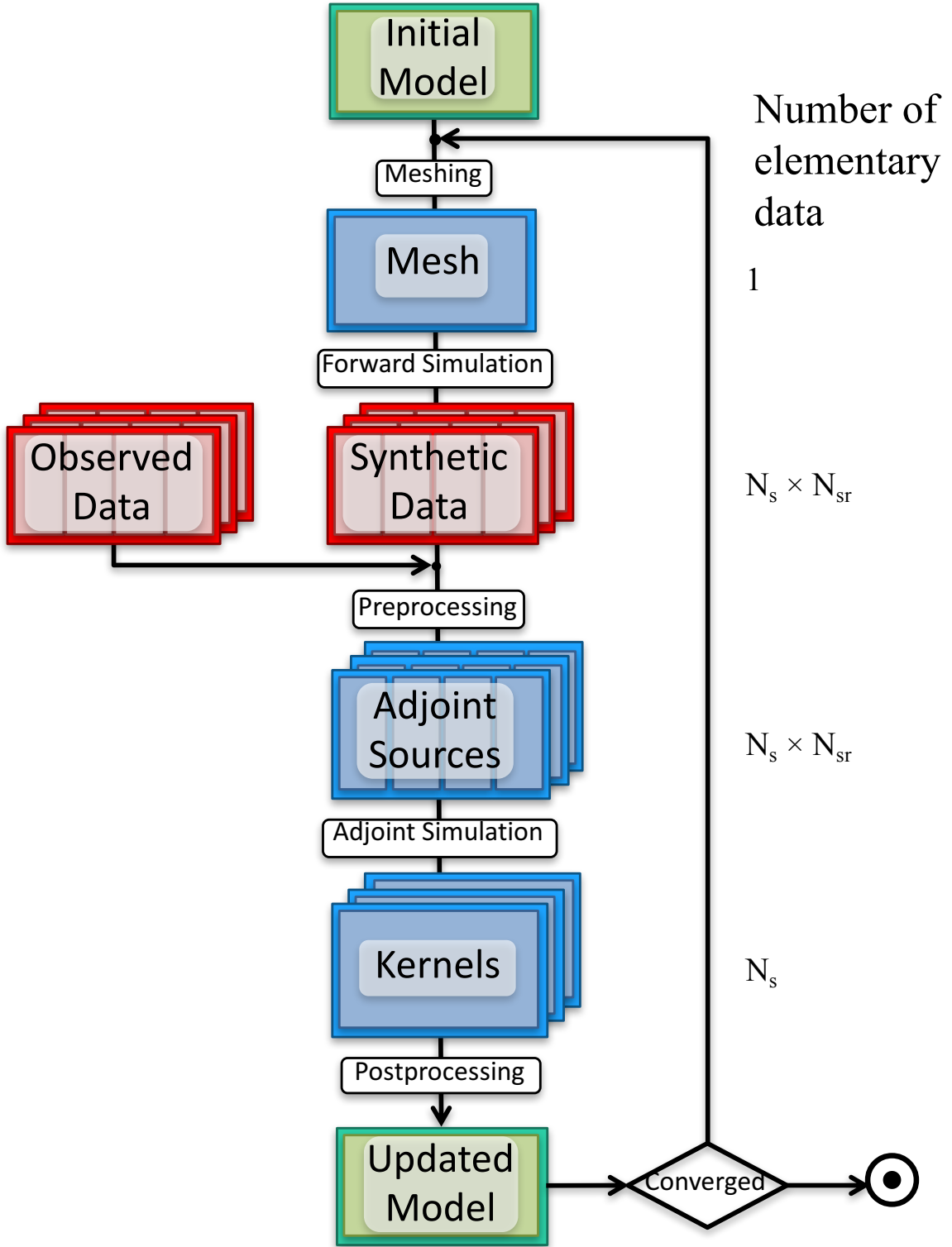


Figure 3.1: General adjoint tomography workflow. The focus is on the data involved in each step. Seismic data are depicted by red boxes and for each of the N_s seismic events they are recorded by N_{sr} receivers. Computational data are represented by green and blue boxes. The amount of elementary data varies depending on the workflow stage and eventually be grouped into a smaller number of files.

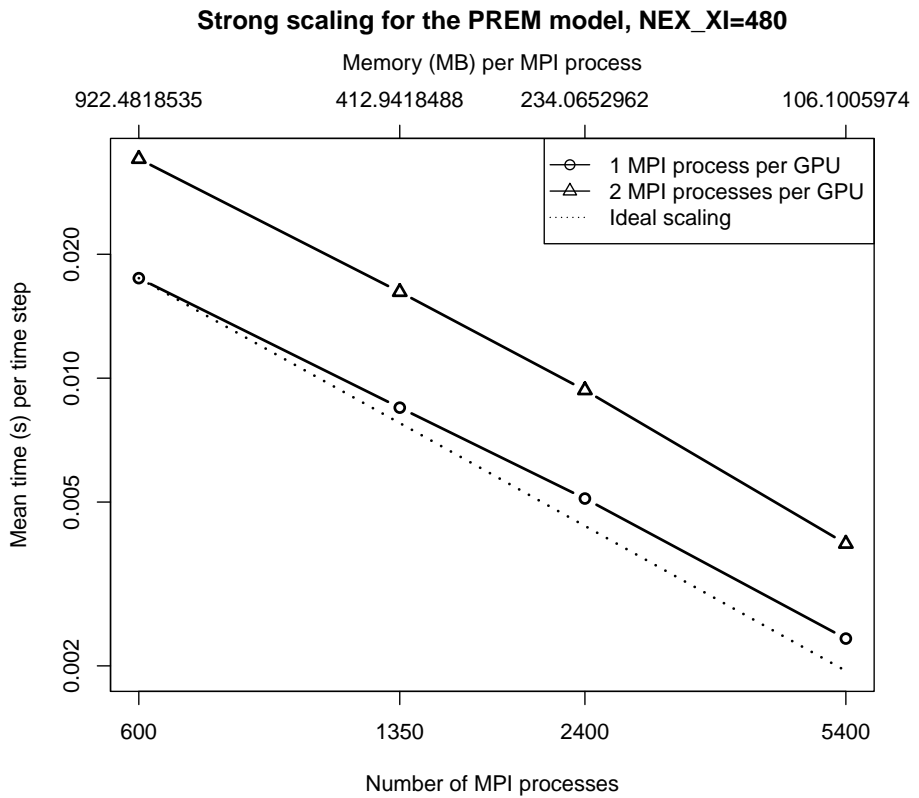


Figure 3.2: Strong scaling for the spherically symmetric PREM Earth model on Titan for a minimum seismic period of 9 s. The mesh is comprised of ~ 25 million elements for this resolution. Values are plotted against the number of MPI processes.

Weak scaling for the PREM model

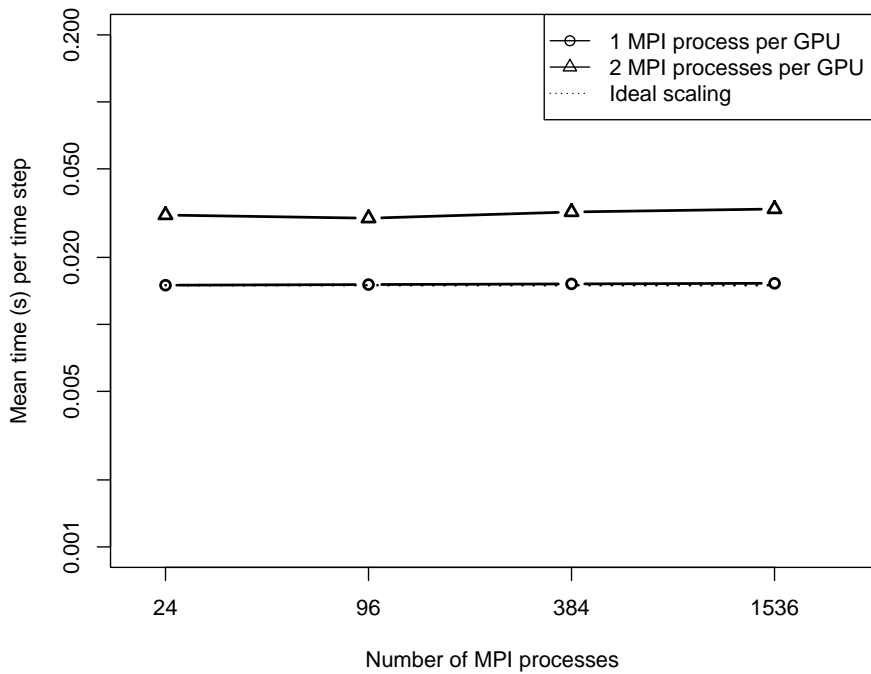


Figure 3.3: Weak scaling for the PREM Earth model on Titan. Performance is measured as the averaged mean time for each time step. The same work load is applied to each MPI process in different cases.

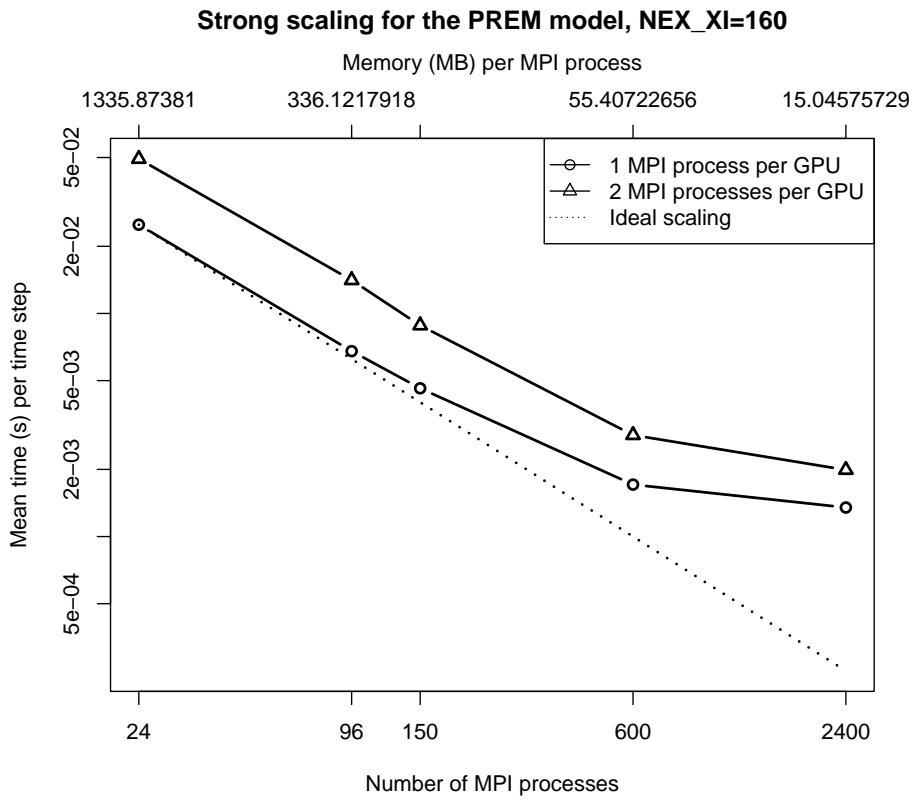


Figure 3.4: Strong scaling for the PREM Earth model on Titan for a minimum seismic period of 27 s with full attenuation. Values are plotted against the number of MPI processes.

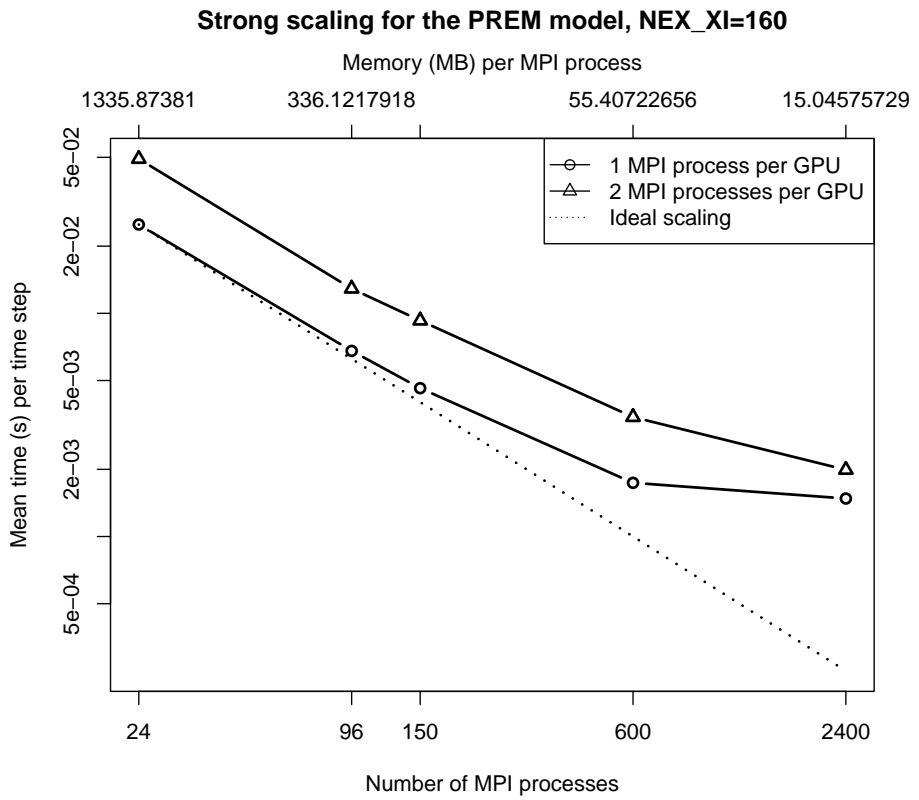


Figure 3.5: Strong scaling for the PREM model on Titan for a minimum seismic period of 27s in the case of without *full attenuation*. Values are plotted against the number of MPI processes.

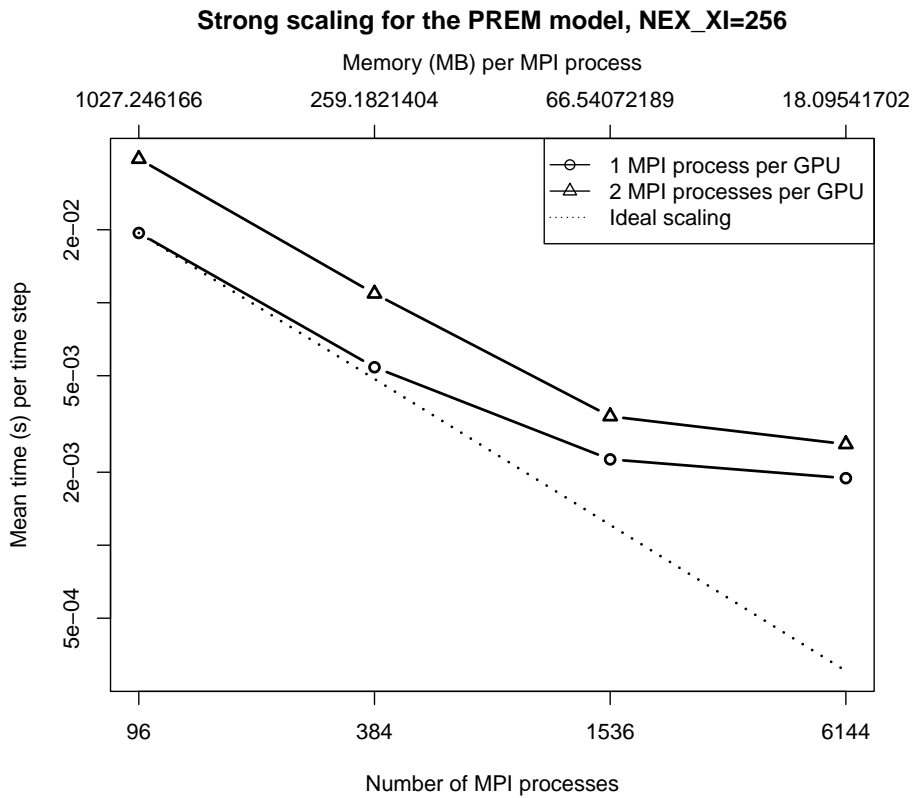


Figure 3.6: Strong scaling for the PREM model on Titan for a minimum seismic period of 17 s in the case of with *full attenuation*. Values are plotted against the number of MPI processes.

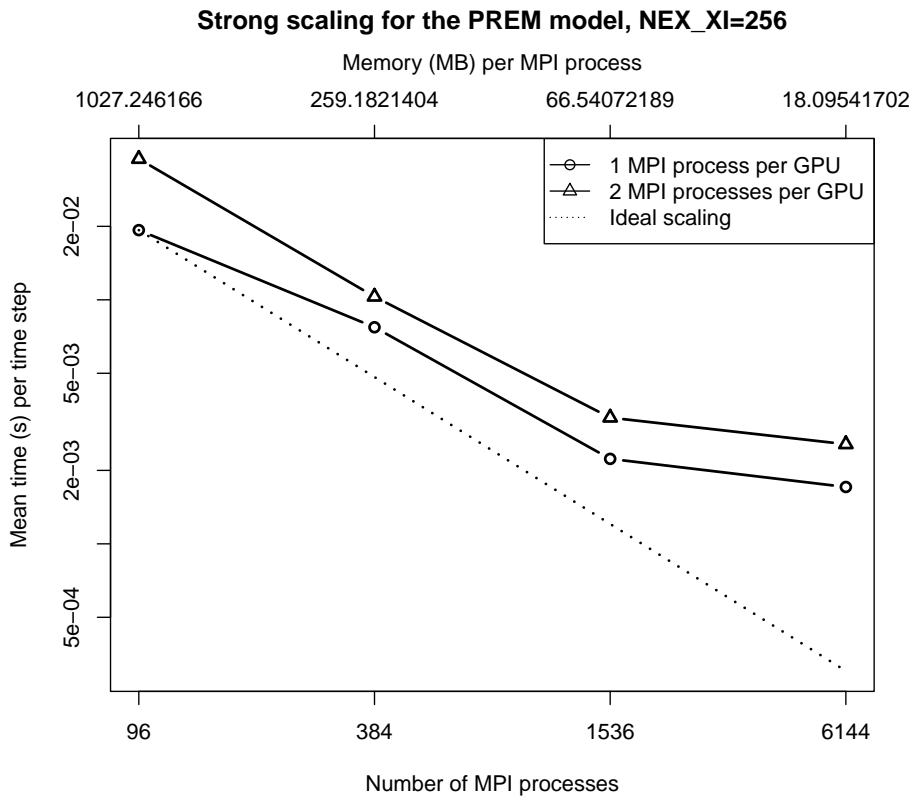


Figure 3.7: Strong scaling for the PREM model on Titan for a minimum seismic period of 17s in the case of without *full attenuation*. Values are plotted against the number of MPI processes.

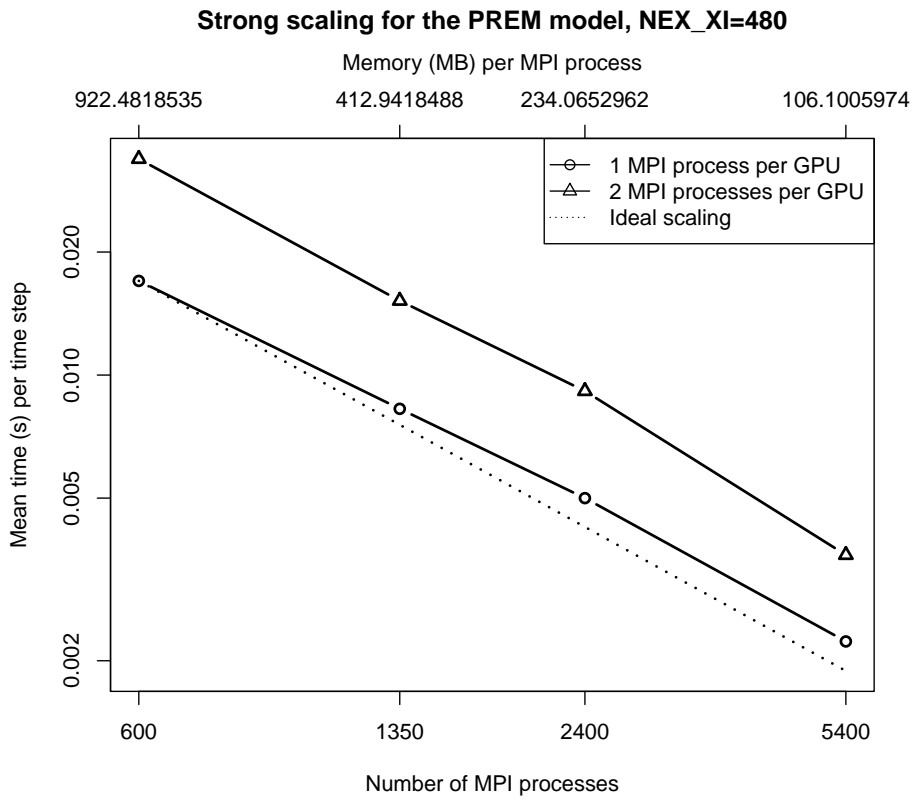


Figure 3.8: Strong scaling for the PREM model on Titan for a minimum seismic period of 9s in the case of without *full attenuation*. Values are plotted against the number of MPI processes.

```

[scale=0.8]
[top color = black, bottom color = black!15!white] (0,0) rectangle +(0.5,10);
[top color = black!50!white, bottom color = black!10!white] ((10,9) rectangle +(0.5,1));
[top color = black!65!white, bottom color = black!20!white] ((10,8) rectangle +(0.5,1));
[dashed] (10,3) rectangle +(0.5,5); [top color = black!70!white, bottom color = black!30!white] ((10,2) rectangle +(0.5,1));
[top color = black!85!white, bottom color = black!45!white] ((10,1) rectangle +(0.5,1));
[top color = black, bottom color = black!50!white] ((10,0) rectangle +(0.5,1));
[top color = black!15!white, bottom color = black] (12,0) rectangle +(0.5,10);
[color = black!40!white] (5,10) circle [x radius=8mm, y radius=4mm]; [color = black!40!white] (5,9) circle [x radius=8mm, y radius=4mm];
[color = black!40!white] (5,8) circle [x radius=8mm, y radius=4mm]; [color = black!40!white] (5,2) circle [x radius=8mm, y radius=4mm];
[color = black!40!white] (5,1) circle [x radius=8mm, y radius=4mm];
[- $\iota$ , thick, densely dotted,  $\iota = \text{triangle } 45$ ] (0.5,10) –(4.2,10);
[- $\iota$ , thick, densely dotted,  $\iota = \text{triangle } 45$ ] (0.5,9) –(4.2,9);
[- $\iota$ , thick, densely dotted,  $\iota = \text{triangle } 45$ ] (0.5,8) –(4.2,8);
[- $\iota$ , thick, densely dotted,  $\iota = \text{triangle } 45$ ] (0.5,2) –(4.2,2);
[- $\iota$ , thick, densely dotted,  $\iota = \text{triangle } 45$ ] (0.5,1) –(4.2,1);
[- $\iota$ , thick, densely dotted,  $\iota = \text{triangle } 45$ ] (5.8,1) –(10,10);
[- $\iota$ , thick, densely dotted,  $\iota = \text{triangle } 45$ ] (5.8,2) –(10,9);
[- $\iota$ , thick, densely dotted,  $\iota = \text{triangle } 45$ ] (5.8,8) –(10,3);
[- $\iota$ , thick, densely dotted,  $\iota = \text{triangle } 45$ ] (5.8,9) –(10,2);
[- $\iota$ , thick, densely dotted,  $\iota = \text{triangle } 45$ ] (5.8,10) –(10,1);
[- $\iota$ , thick,  $\iota = \text{triangle } 45$ ] (-0.2,10) –(-0.2,0);
[- $\iota$ , thick,  $\iota = \text{triangle } 45$ ] (10.7,10) –(10.7,9.1) –(11.8,10) –(11.8, 9) –(10.7, 8.9) –(10.7,8.1) –(11.8, 8.9) –(11.8, 8);
[- $\iota$ , thick,  $\iota = \text{triangle } 45$ ] (10.7,3) –(10.7,2.1) –(11.8,3) –(11.8, 2) –(10.7, 1.9) –(10.7,1.1) –(11.8, 1.9) –(11.8, 1) –(10.7, 0.9) –(10.7, 0.1) –(11.8, 0.9) –(11.8, 0);
[align=center,below] at (5,-0.1) Snapshots; [align=center,below] at (10.25,-0.1)
    Forward; [align=center,below] at (12.25,-0.1) Adjoint;
[decorate,decoration=brace,amplitude=10,mirror,yshift=0] (9.5,-0.6) –(13,-0.6)
    node [black,midway,xshift=0, yshift=-17] Gradient simulation;
[decorate,decoration=brace,amplitude=10,mirror,yshift=0] (-0.5,-0.6) –(1,-0.6)
    node [black,midway,xshift=0, yshift=-17] Forward simulation;

```

Figure 3.9: I/O pattern with full attenuation. The forward simulation (left bar) produces snapshots at regular intervals. During the kernel simulation (right bars) these snapshots are read in reverse order to piece-wise reconstruct the forward wavefield for a number of time steps. The interaction of this reconstructed wavefield with the adjoint wavefield yields to the so-called event kernels, the sum of which is the misfit gradient. Solid arrows depict computation order, dashed arrows represent I/O. Bars shade from black to light gray jointly with forward time.

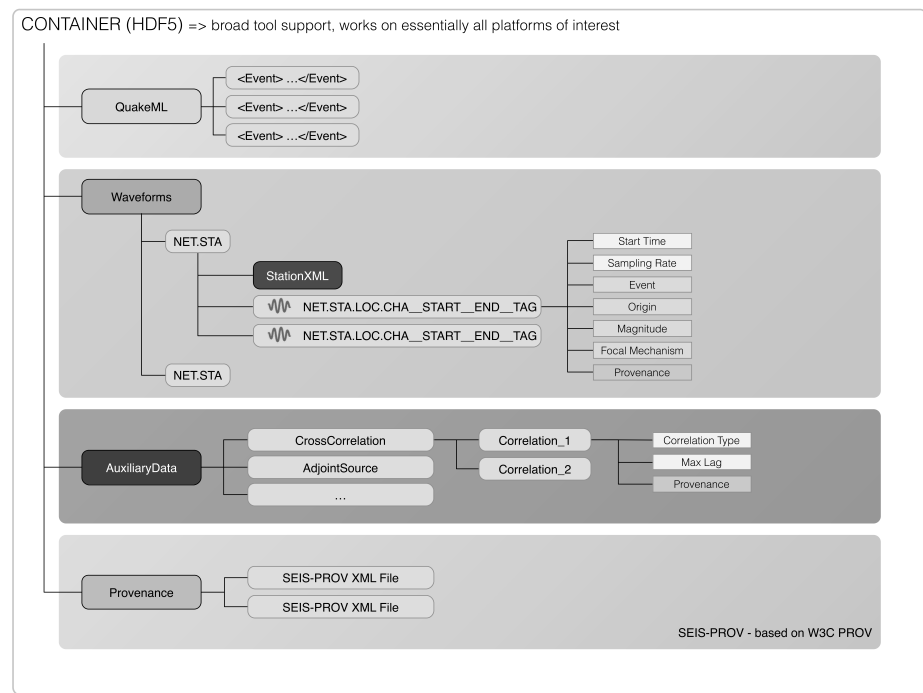


Figure 3.10: Layout of the Adaptable Seismic Data Format, including earthquake event information, waveforms and station meta information, auxiliary data and provenance. In such layout, different types of data are grouped into one file and ready for later retrieval.

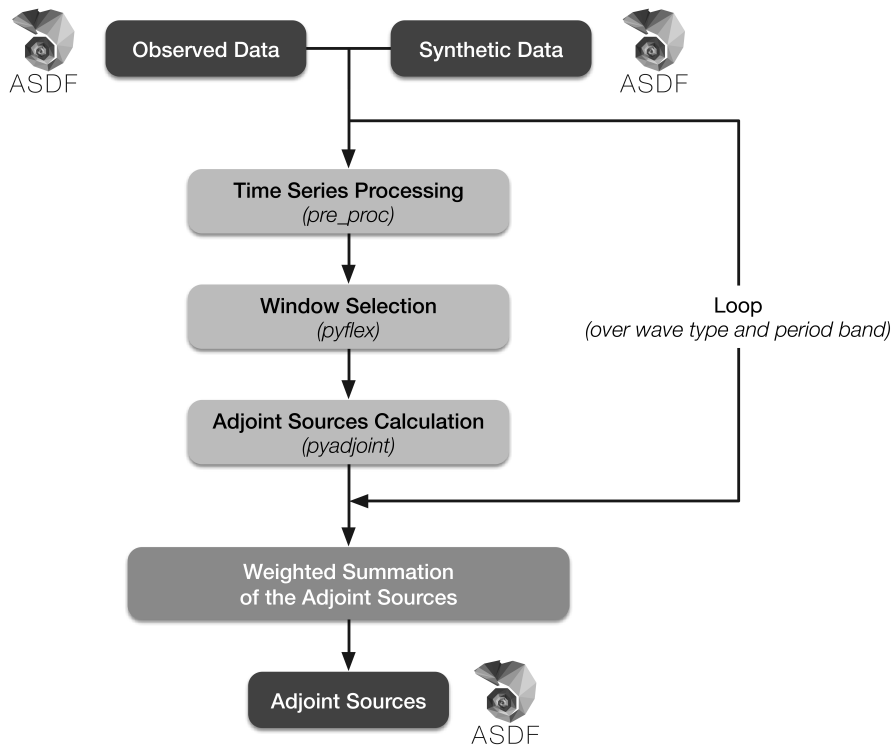


Figure 3.11: Workflow of seismic data processing using ASDF. First, time series analysis is applied to raw observed and synthetic data to ensure a comparable spectral content at a later stage. Then, time windows are selected for pairs of processed observed and synthetic data, inside which measurement are made. Finally, adjoint sources are generated as the final pre-processing output. ASDF speeds up these tasks by using parallel processing (MPI). For each step, processing information is added to the provenance.

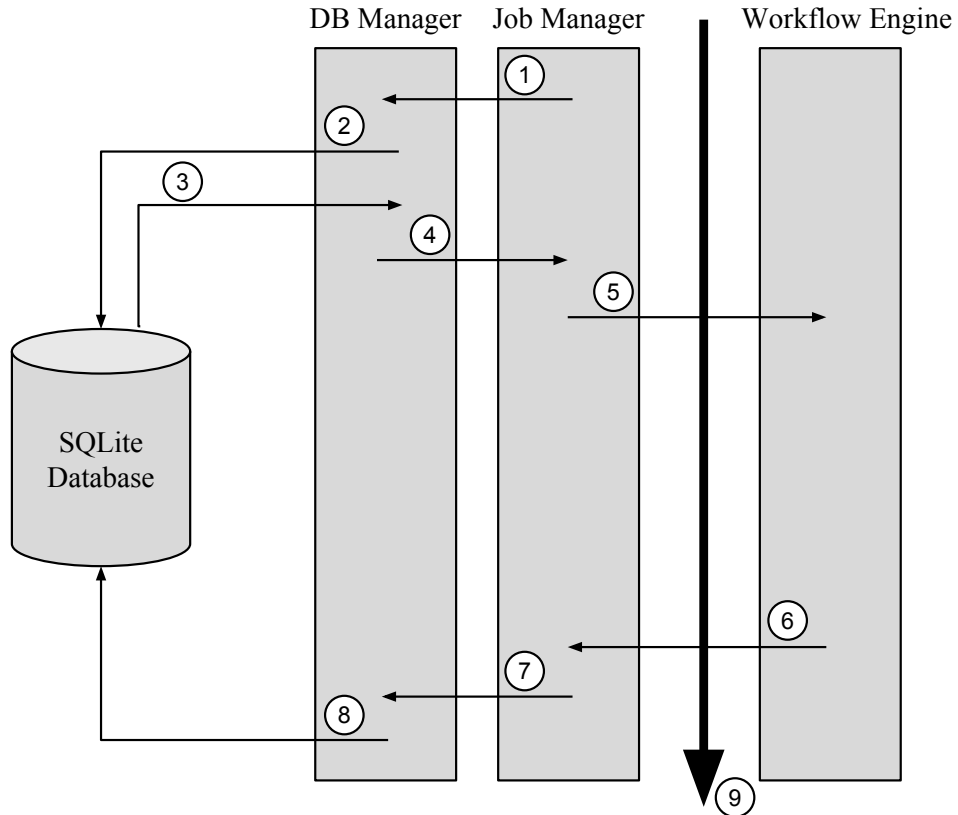


Figure 3.12: Steering process of the workflow management system. Two objects (DB manager and Job Manager) serve as an interface between the database and the workflow engine. The job manager requests data from the DB manager (1), which polls an SQLite database (2). Once the request is served (3), executables, parameters, and inputs are formatted (4) to feed the workflow engine (5). The workflow engine transparently launches the job and monitors its status, which is then returned (6). The status is used to update the database (7, 8) in order to keep track of the inversion status. This process is repeated (9), until everything has been processed.

Chapter 4

Balancing Unevenly Distributed Data in Seismic Tomography: A Global Adjoint Tomography Example

Note

This chapter was submitted as a paper entitled "Balancing Unevenly Distributed Data in Seismic Tomography: A Global Adjoint Tomography Example" by Ruan, Youyi and Lei, Wenjie, and Modrak, Ryan, and Örsvuran, Ridvan, and Bozdağ, Ebru, and Tromp, Jeroen to *Geophysical Journal International*, 2019.

4.1 summary

The uneven distribution of earthquakes and stations in seismic tomography leads to slower convergence of nonlinear inversions and spatial bias in inversion results. Including dense regional arrays, such as USArray or Hi-Net, in global tomography

causes severe convergence and spatial bias problems, against which conventional preconditioning schemes are ineffective. To save computational cost and reduce model bias, we propose a new strategy based on a geographical weighting of sources and receivers. We validate this strategy in a 2D global waveform inversion test and show that the new weighting scheme leads to a nearly two-fold reduction in model error and much faster convergence relative to a conventionally-preconditioned inversion. We implement this geographical weighting strategy for global adjoint tomography.

4.2 summary

4.3 Introduction

The deployment of new global and regional seismographic stations has made more data available for seismic tomography than ever before. The spatial distribution of these stations remains highly lopsided, however, with limited Ocean Bottom Seismometers (OBSs) or ocean island stations, and fewer stations in the southern hemisphere than in the northern hemisphere. This uneven station coverage, combined with the uneven distribution of earthquakes dictated by plate tectonics, poses major challenges for the inverse problem. In global adjoint tomography in particular, the large number of paths from subduction zones, such as Fiji-Tonga, to dense arrays, such as USArray, causes highly oscillatory behavior in model updates, hindering convergence [12].

Since the first global tomographic study by [31], uneven data coverage has been an issue of concern. The problem with a cluster of earthquakes or a dense receiver array is that data residuals are correlated, and large portions of data are in some sense redundant. The correlation of data residuals is reflected in the data covariance matrix: its diagonal terms are the measurement error of each datum, and off-diagonal

terms indicate coherence between the errors of two corresponding data. Ideally, data errors are independent, in which case only diagonal terms need to be considered, and off-diagonal terms can be safely ignored. When measurements are strongly correlated, the off-diagonal terms become relevant.

Although uneven data coverage is a well-known issue in seismic tomography, there is limited literature on how it should be properly dealt with. In an important global seismic tomography study by [69], uneven data coverage was addressed by weighting the diagonal terms of the data covariance matrix according to how significant their errors are correlated with the errors of the other data. The weighting function in this study ($\omega = \omega_e \omega_n \omega_r$) consists of data errors (ω_e — the rms amplitude of a wave packet), data redundancy within a wave packet (ω_n — the inverse of the square root of number of data), and data redundancy amongst wave packets sampling similar ray paths (ω_r — a geometrical relationship between a given source-receiver pair to all other pairs). The final term addresses data covariance through a path weighting strategy and has been employed in a few subsequent global tomography studies [112]. In this paper, we adopt a similar but more general approach to handle unevenly distributed measurements.

The effects of uneven data coverage depend to some extent on the model parameterization and regularization in a given inversion. [11] examined the effects of uneven data coverage with differently parameterized and regularized inversions. They parameterized their global model in terms of both blocks and spherical harmonics. Sparse data coverage in the southern hemisphere produced fictitious model features, especially in the spherical harmonic model. Applying stronger regularization or damping, however, more or less resolved the issue. In other words, to resolve bias in inversions caused by uneven data coverage, we need to sacrifice resolution in well-covered regions through stronger damping. Their experiments justify to some extend the use of strong damping in some global inversions [80, 3].

Besides geographical weighting, other strategies have been developed in different contexts [43, 62, 108, 92]. For instance, the use of weights based on analyst-assessed data quality or weights for jointly inverting disparate data types (e.g., seismic and gravity measurements). These weighting choices are sometimes ad hoc and vary from one practitioner to another. In this study, we focus on weighting with the goal of balancing uneven data coverage, without drawing many connections with other types of weighting. Since full-waveform adjoint tomography is computationally expensive, it is important to address slow convergence due to unevenly distributed data. Here, we focus on a robust weighting strategy that can be applied to unevenly distributed earthquakes and stations to balance their contributions.

4.4 Weighting strategy

4.4.1 Measurements and Misfit Function

Seismic waves sample different parts of Earth’s interior at different dominant frequencies, so it is natural to categorize seismic signals in terms of their type and band. In global adjoint tomography [12, 67], we currently consider three period bands: 17–40 s, 40–100 s, and 90–250 s. Typically, we select body waves in the 17–40 s band, body waves in the 40–100 s band, surface waves in the 40–100 s band, and surface waves in the 90–250 s band. Within each band, we consider three-component seismograms rotated into vertical, radial, and transverse directions of motion, so in total there are twelve data categories, as summarized in Table 4.1.

Considering all these data categories, along with all the sources and receivers available for an inversion, we define an overall data misfit

$$\Phi = \sum_{s=1}^S \omega_s \sum_{c=1}^C \omega_c \sum_{r=1}^{R_{sc}} \omega_{scr} \sum_{w=1}^{N_{scr}} \omega_{scrw} \chi_{scrw} . \quad (4.1)$$

	Vertical (Z)	Radial (R)	Transverse (T)
17–40 s	P-SV body waves	P-SV body waves	SH body waves
40–100 s	P-SV body waves	P-SV body waves	SH body waves
40–100 s	Rayleigh waves	Rayleigh waves	Love waves
90–250 s	Rayleigh waves	Rayleigh waves	Love waves

Table 4.1: Measurement categories in global adjoint tomography [12, 67]. Seismic waves are categorized in terms of complementary period bands on three components of motion.

Here, $s = 1, \dots, S$ denotes a given source and S the total number of sources. Likewise, $c = 1, \dots, C$ denotes a given category and C the total number of categories (in our case, the twelve categories summarized in Table 4.1). R_{sc} denotes the number of receivers for a given source s and category c . Finally, N_{scr} denotes the number of measurement windows for a given source s , category c , and receiver r .

The misfit for a given source s , category c , receiver r , and measurement window w is

$$\chi_{scrw} = \left(\frac{\Delta d_{scrw}}{\sigma_{scrw}} \right)^2 , \quad (4.2)$$

where Δd_{scrw} denotes a measurement with associated uncertainties σ_{scrw} . When the model fits the data to within one standard deviation, we expect that

$$\chi_{scrw} \sim 1 . \quad (4.3)$$

In the following sections we discuss various options for the assignment of the source, category, receiver, and window weights ω_s , ω_c , ω_{scr} , and ω_{scrw} , respectively.

4.4.2 Category-weighting strategy

We start by considering an ideal case where each datum in a certain category is independent and the associated errors are not correlated. (In reality, the measurement error of a datum is difficult to estimate, not to mention the correlation of the errors.) The standard deviation σ_{scrw} in eqn. (4.2) is often set as an *a priori* constant in

the practice of inversion. Under such conditions, a common weighting strategy is to assign a constant weight to all windows, receivers, and sources, i.e.,

$$\omega_s = 1 \quad , \quad (4.4)$$

$$\omega_{scr} = 1 \quad , \quad (4.5)$$

$$\omega_{scrw} = 1 \quad . \quad (4.6)$$

We seek to define a misfit function Φ such that when the model fits the data to within one standard deviation, $\Phi \sim 1$. The data in each category should contribute equally to the overall misfit, which implies that we should choose a category weight

$$\omega_c = \frac{1}{C} \frac{1}{N_c} \quad , \quad (4.7)$$

where N_c is the number of measurements in category c , that is

$$N_c = \sum_{s=1}^S \sum_{r=1}^{R_{sc}} N_{scr} \quad . \quad (4.8)$$

Note that the category weight in eqn. (4.7) is independent of source s . Now we see that when the model fits the data to within one standard deviation, i.e., $\chi_{scrw} \sim 1$,

then

$$\Phi \sim \sum_{s=1}^S \omega_s \sum_{c=1}^C \omega_c \sum_{r=1}^{R_{sc}} \omega_{scr} \sum_{w=1}^{N_{scr}} \omega_{scrw} \quad (4.9)$$

$$= \sum_{s=1}^S \sum_{c=1}^C \omega_c \sum_{r=1}^{R_{sc}} N_{scr} \quad (4.10)$$

$$= \sum_{c=1}^C \frac{1}{C} \frac{1}{N_c} \sum_{s=1}^S \sum_{r=1}^{R_{sc}} N_{scr} \quad (4.11)$$

$$= \sum_{c=1}^C \frac{1}{C} \quad (4.12)$$

$$= 1 \quad , \quad (4.13)$$

as desired.

Let us next analyze the contribution of each datum to the misfit function at various levels. At the receiver level, we consider

$$\chi_{scr} = \sum_{w=1}^{N_{scr}} \omega_{scrw} \chi_{scrw} \quad . \quad (4.14)$$

When we assign a weight of one to all windows, i.e., $\omega_{scrw} = 1$, thus putting them on the same footing, and when the model fits the data to within one standard deviation, i.e., $\chi_{scrw} \sim 1$, we see that

$$\chi_{scr} \sim N_{scr} \quad . \quad (4.15)$$

Next, we consider the misfit for a given source s and category c , namely

$$\chi_{sc} = \sum_{r=1}^{R_{sc}} \omega_{scr} \sum_{w=1}^{N_{scr}} \omega_{scrw} \chi_{scrw} = \sum_{r=1}^{R_{sc}} \omega_{scr} \chi_{scr} \quad . \quad (4.16)$$

When the model fits the data to within one standard deviation, we find that

$$\chi_{sc} \sim \sum_{r=1}^{R_{sc}} N_{scr} = N_{sc} \quad , \quad (4.17)$$

where N_{sc} denotes the number of measurements for a given source s in category c . Note that we have used the fact that $\omega_{csr} = 1$, meaning all receivers are weighted equally.

Since category weighting is independent of source weighting, we can change the order of summation. The misfit in a given category c is given by

$$\chi_c = \sum_{s=1}^S \omega_s \chi_{sc} . \quad (4.18)$$

Since $\omega_s = 1$, we see that when the model fits the data to within one standard deviation

$$\chi_c \sim \sum_{s=1}^S N_{sc} = N_c , \quad (4.19)$$

as expected.

Finally, the total misfit function is

$$\Phi = \sum_{c=1}^C \omega_c \chi_c , \quad (4.20)$$

and thus we see that when the model fits the data to within one standard deviation

$$\Phi \sim \sum_{c=1}^C \frac{1}{C} \frac{1}{N_c} N_c = 1 . \quad (4.21)$$

as required. This weighting scheme is widely used in a variety of inversions [154, 12]. The behavior of the misfit function at the various levels demonstrated above will guide the design of source and receiver weights in the next section.

4.4.3 Geographical-weighting strategy

In the previous section we treated each measurement datum in a given category equally, which means each datum was weighted only by the total number of measure-

ments in its category, regardless of possible correlations between data. Solving the inverse problem based on this “all datums are equal” strategy can fail sometimes, because the uneven spatial distribution of sources and receivers on Earth’s surface is found to negatively affect convergence rate. In particular, if data from dense regional arrays such as USArray are included, progress of the inversion can be extremely slow. In this section, we add additional weights associated with the geographical distribution of sources and receivers, with the goal of down-weighting densely sampled regions, so that we obtain more uniform spatial sampling and minimize the dominant effects of dense regional arrays.

Geographical Weighting

For closely located sources or dense receiver arrays, measurement errors are correlated for a variety of reasons [69], and the degree of correlation is associated with geographical distance. With these correlations in mind, we seek to define a source and receiver weighting scheme that results in more uniform spatial sampling. In such a scheme, areas with dense sampling, like Japan or North America, should be down-weighted relative to areas which are sparsely sampled, such as the Southern Ocean.

To determine weights for each source and receiver, one option is to construct a Voronoi tessellation [29] of the sources or receivers, and then weight each source or receiver by the area of its corresponding cell. Unfortunately, this approach can lead to instabilities, because stations at the edge of a dense array can be weighted orders of magnitude more than stations slightly away from the edge.

A robust alternative approach is as follows. Given a set of N receivers, calculate the epicentral distance Δ_{ij} for each receiver pair. The weight ω_i assigned to each receiver i is calculated via

$$\omega_i^{-1} = \sum_{j=1}^N \exp \left[-\left(\frac{\Delta_{ij}}{\Delta_0} \right)^2 \right] \quad , \quad (4.22)$$

where Δ_0 is a reference distance parameter. We note that if a station has few nearby stations, it is assigned a larger weight than if it has many nearby stations. For large values of Δ_0 the scheme reduces to the category weighting in Section 4.4.2.

We also note that an equivalent weighting scheme for sources can be obtained by substituting source pairs for receiver pairs in the above expression. In Section 4.4.3 we discuss how weights determined by eqn. (5.2) are normalized to obtain weights ω_c for each event and ω_{csr} for each receiver associated with a certain event.

Interestingly, eqn. (5.2) is just a discretized version of the “regularization by convolution” method used in many parameter estimation and optimal design studies [86]. Rather than using convolution to smooth the gradient of an objective function, however, we are using it to “smooth” the uneven discrete receiver distribution.

Choice of reference parameter

The distribution of weights calculated from eqn. (5.2) depends strongly on the reference distance Δ_0 . This parameter needs to be carefully chosen so that the ratio of maximum to minimum weights is not unreasonably small or large. In the example in Figure 4.1, we chose Δ_0 so that the ratio is about one third of the largest possible ratio for all choices of Δ_0 . In other words, we chose the reference length parameter to be about one third of the most aggressive value.

Based on this choice, Figures 4.2 and 4.3 illustrate the distribution of weights in a recent global adjoint tomography study [67]. In Figure 4.2, USArray and European stations weights are brought down to about one-tenth of ocean island station weights. The source weighting is similar, with the contribution of individual Fiji Tonga events brought down to about one-tenth the contribution of intraplate events in Asia. This ratio between the minimum and maximum weights can be adjusted through the reference distance parameter, as informed by practical experience in a given inversion.

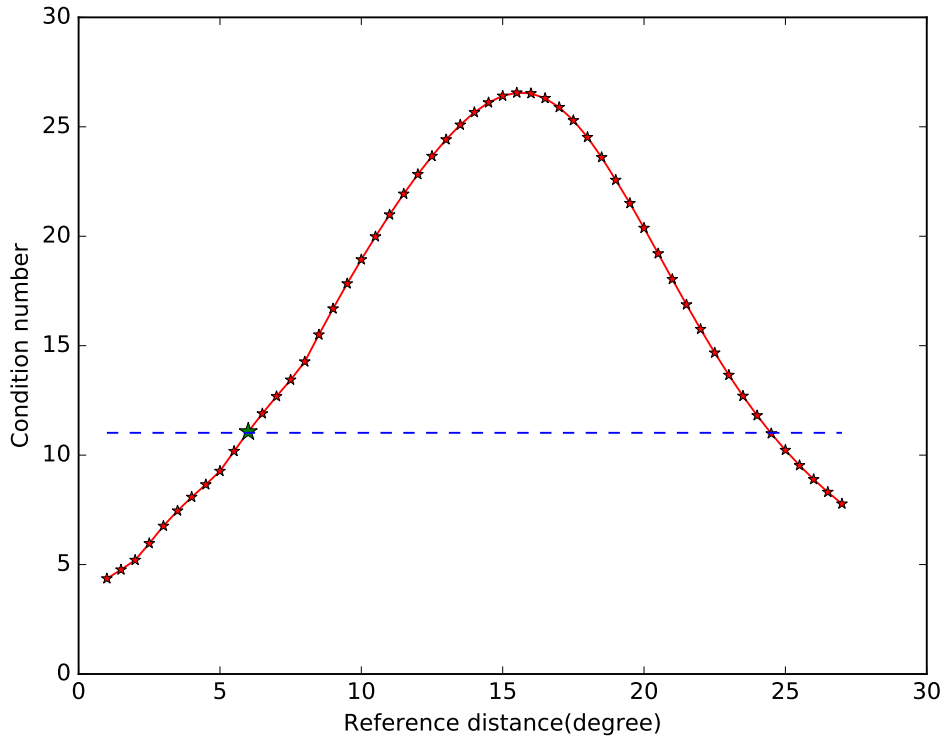


Figure 4.1: Condition number of the diagonal weighting matrix defined by eqn. (5.2) as a function of the reference distance Δ_0 . The chosen value, indicated by the green star, is about one third of the largest possible value. Since evaluation of eqn. (5.2) for different reference distances adds negligible computational expense, it is possible (and recommended) to repeat this type of analysis for each iteration.

Weighting Normalization

In this section our goal is to introduce geographical source and receiver weighting without changing the event- and category-level behavior of the misfit function discussed in Section 4.4.2.

In geometrical ray-based tomography, specific phases are identified and windowed. These phases usually correspond to distinct paths that provide constraints on different parts of Earth's interior, and some phases may be assigned more weight than others depending on the aims of the researcher. In waveform inversion, any part of the wave train can be selected and phase identification is no longer required. We thus assign a

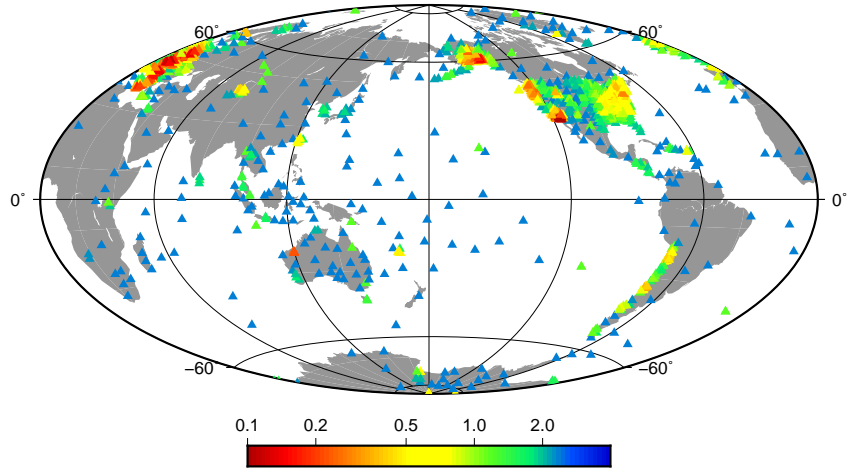


Figure 4.2: Example of receiver weights for an event C201604131355A at 40–100 s period band and vertical component determined based upon eqn. (5.2), and normalized according to eqn. (4.25). The weights are in logarithmic scale. Note the difference between USArray stations and ocean island stations.

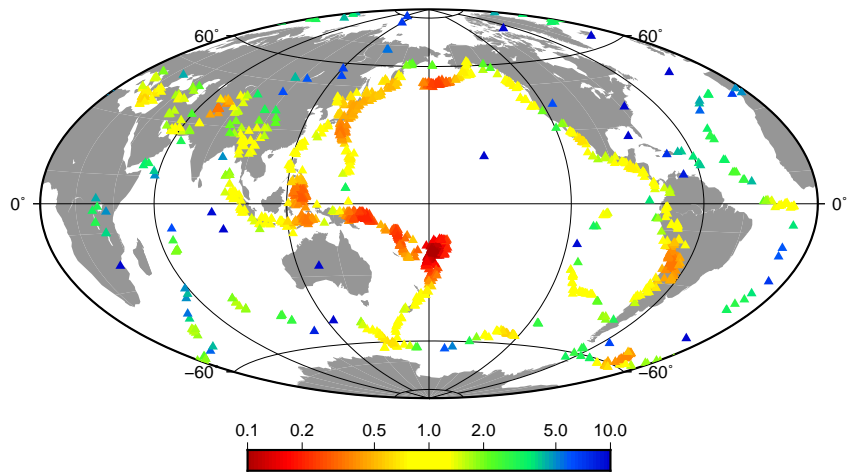


Figure 4.3: Example of source weights determined based upon eqn. (5.2), and normalized according to eqn. (4.24). Note the difference between dense subduction zone earthquakes and sparse transform fault earthquakes.

uniform weight to all windows in a seismogram,

$$\omega_{scrw} = 1 \quad , \quad (4.23)$$

such that, according to eqn. (4.15), $\chi_{scr} \sim N_{scr}$. The normalization of the geographical source weights from eqn. (5.2) is then determined in a straightforward manner by

$$\sum_{s=1}^S \omega_s = S \quad . \quad (4.24)$$

Because the number of receivers that happen to be online varies from one source to another, including receiver weights in an inversion is not as straightforward. To guide the normalization of receiver weights, we adopt the same type of analysis performed in connection with category-weighting and eqn. (4.16).

If the model fits the data to within one standard deviation, the misfit in a certain source and category χ_{sc} approaches N_{sc} , and the receiver-level misfit χ_{scr} approaches N_{scr} (eqns. 4.15–4.17). These properties of the misfit imply a normalization requirement for the receiver weights ω_{scr} , determined by eqn. (5.2) for a given category c and source s :

$$\sum_{r=1}^{R_{sc}} \omega_{scr} N_{scr} = N_{sc} \quad . \quad (4.25)$$

When $\omega_{scr} = 1$, as in the simple weighting strategy, this normalization condition is naturally satisfied because

$$\sum_{r=1}^{R_{sc}} N_{scr} = N_{sc} \quad . \quad (4.26)$$

After we determine the source and receiver weights, what is left is to examine the category weights ω_c . For the misfit function given by eqn. (5.3), we want the contri-

butions from each category to be balanced, and this implies that

$$\omega_c \sum_{s=1}^S \omega_s \sum_{r=1}^{R_{sc}} \omega_{scr} N_{scr} = \omega_c \sum_{s=1}^S \omega_s N_{sc} = \frac{1}{C} , \quad (4.27)$$

and thus

$$\omega_c = \frac{1}{C} \frac{1}{\sum_{s=1}^S \omega_s N_{sc}} . \quad (4.28)$$

Note that when $\omega_s = 1$, the weighting reduce to the category-weighting strategy, namely

$$\omega_c = \frac{1}{C} \frac{1}{N_c} . \quad (4.29)$$

From the normalization of geographical weights described above, we see that when the model fits the data to within one standard deviation, the source-level misfit χ_{sc} approaches N_{sc} and category-level misfit χ_c approaches N_c .

In theory, data correlation changes the degrees of freedom in the data space of an inversion. Loosely speaking, the above normalization can be thought of as changing the degrees of freedom of the dataset for a given category c and source s , as well as the degrees of freedom of the dataset in a given category c . Geographical weighting can be viewed as an approximation of the complete data covariance matrix.

4.5 Numerical Validation: 2D Global Adjoint Tomography

To test the geographical weighting strategy, we performed 2D inversions with a global test problem. In these experiments, we used both GSN stations, which are sparsely distributed at the global scale, and USArray stations, which densely cover the North

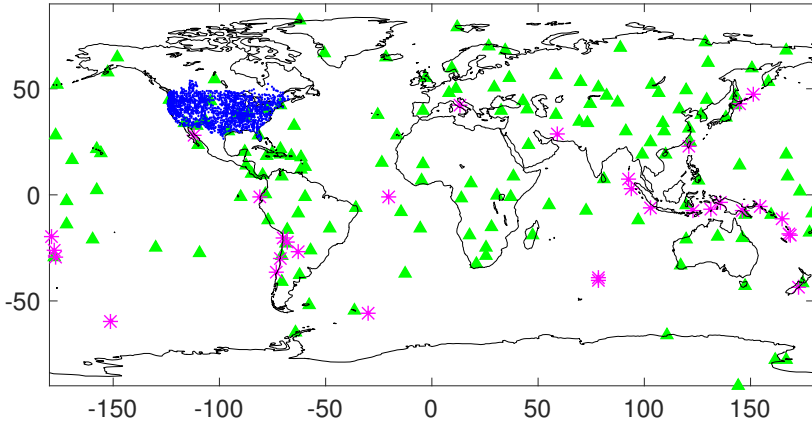


Figure 4.4: Source-receiver geometry used in synthetic inversions. GSN stations are labeled by green triangles, USArray stations by blue triangles, and sources by magenta asterisks.

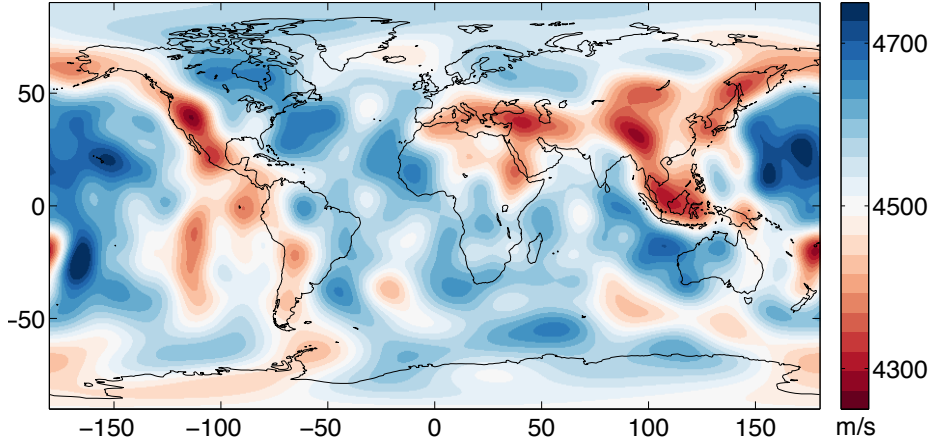


Figure 4.5: Target model used in the synthetic inversions. Wavespeeds are determined by the 40 s Rayleigh wave phase speed model of [131].

American continent, as shown in Figure 4.4. For the target model, we employed the acoustic test case shown in Figure 4.5. We generated synthetic data for this model using periodic boundary conditions at the edges to approximate a spherical Earth. Finally, we inverted these data with the workflow described by [87].

Starting from a homogeneous model, we tracked the reduction in model error as a function of the number of wavefield simulations in three separate inversions. In the first inversion, we employed model-space diagonal preconditioning, using the best-performing preconditioner of all the variants tested by [86]. In the second inversion,

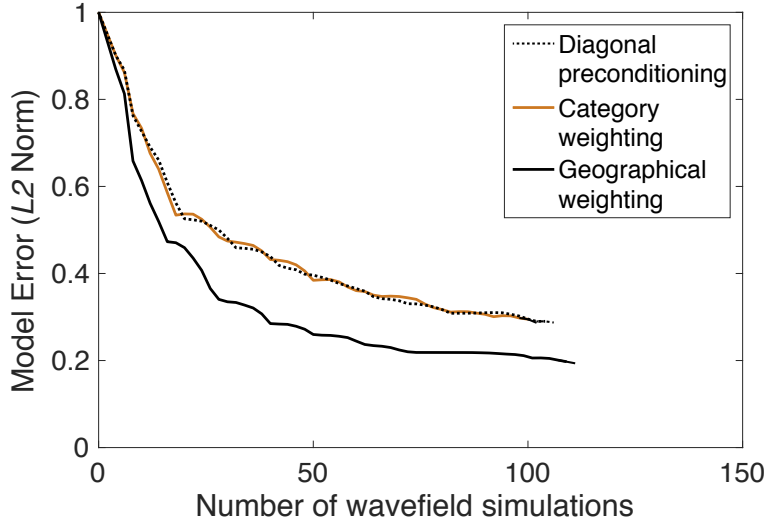


Figure 4.6: With the category weighting defined in Section 4.4.2, convergence is extremely slow. With the geographical weighting discussed in Section 4.4.3, convergence is much faster. Diagonal model-space preconditioning, it turns out, is not an effective alternative to weighting when dealing with extremely lopsided source-receivers distributions.

we employed the category-weighting strategy discussed in Section (4.4.2). In the third inversion, we used the geographical-weighting strategy described in Section 4.4.3. The performance of the three methods is shown in Figure 4.6.

Compared with category weighting, preconditioning fails to provide an effective improvement, while the geographical-weighting strategy provides a much faster convergence rate. Considering the high cost of large-scale inverse problems like global adjoint tomography, where one iteration can require millions of core hours, the saving could be significant. In addition to the performance improvement, the geographically-weighted inversion demonstrates larger model error reduction than the other approaches.

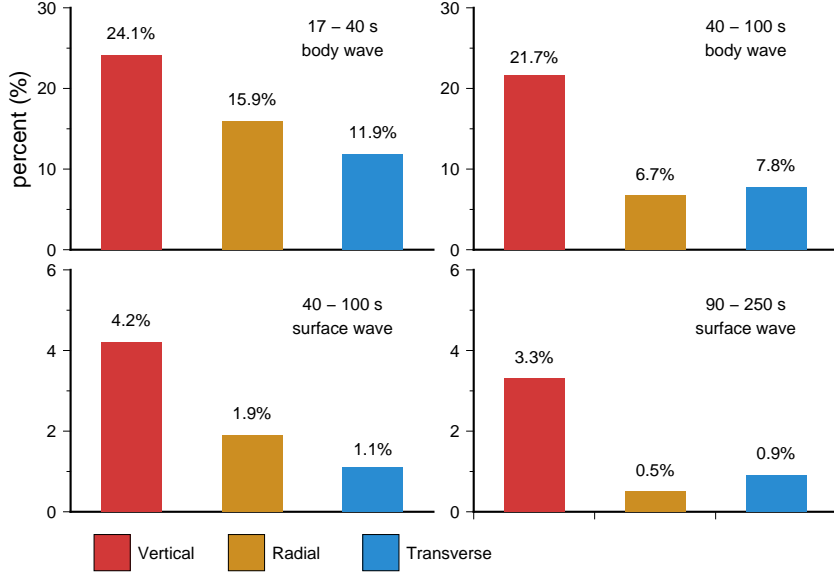


Figure 4.7: Percentage of data (window count) in each of the twelve categories (see Table 4.1). Period band and wave type are labeled in the upper right corner of each panel. Note the dramatic differences between body-wave (top) and surface-wave data (bottom). The large variations in data count from category to category illustrate the need for balancing.

4.6 Application to 3D Global Adjoint Tomography: Misfit Statistics

After testing the geographical-weighting strategy through synthetic experiments, we deployed it in our ongoing global adjoint tomography study [67] with the goal of obtaining faster convergence and a better model. In this section we illustrate various aspects of the above category- and geographical-weighting strategies..

As described in Section 4.4, the weight we assign to each measurement is the product of source, category, receiver, and window weights: $\omega_s \omega_c \omega_{scr} \omega_{scrw}$. In Figures 4.2 and 4.3, we plotted weights ω_s assigned to sources and weights ω_{scr} assigned to receivers. Next, we examine the misfit when the product of all four weights is applied.

In total, we picked more than 17 million windows from 1,480 sources and 12 categories [67]. As shown in Figure 4.7, the contribution from each category is far

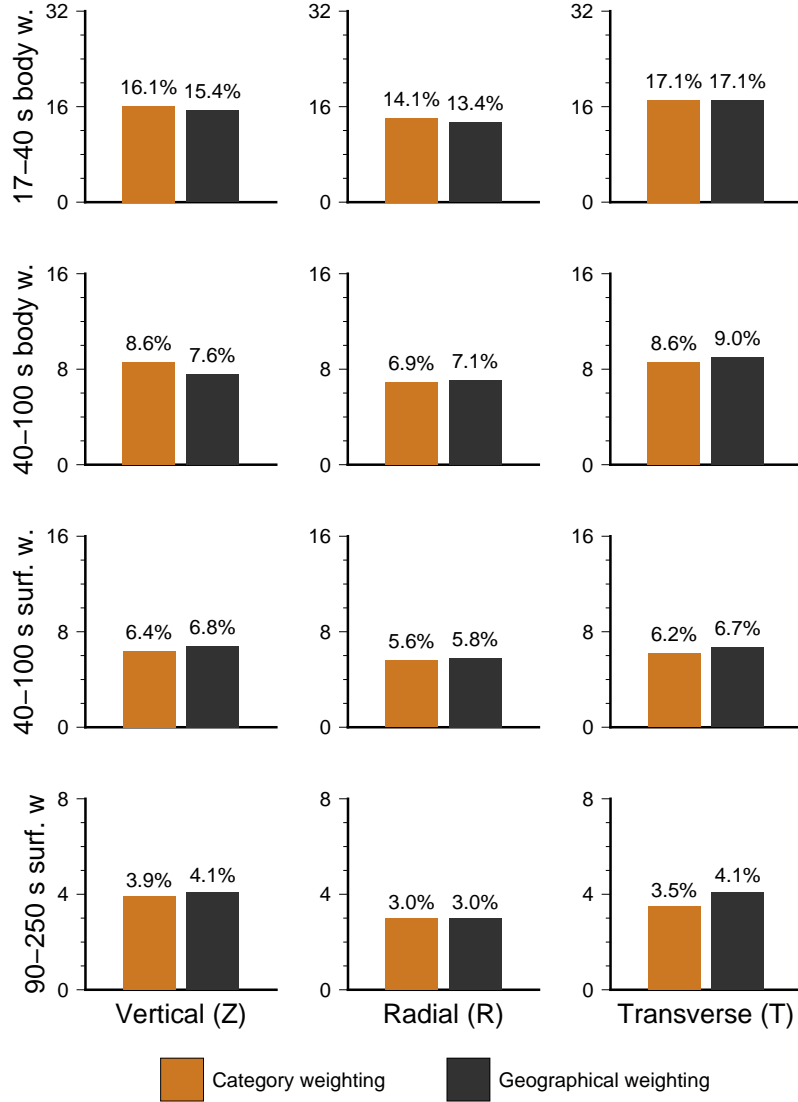


Figure 4.8: Percentage of the misfit in each of the twelve categories (see Table 4.1) using the category-weighting strategy (orange), and geographical-weighting strategy (black). The percentage contribution in each category is labeled above the bars. Note that each category's contribution to the misfit barely changes with geographical weighting, because weight rebalancing only happens within each category.

from balanced. Short period body-wave data (17–40 s) account for more than 50% of the total number of windows while long period surface waves (90–250 s) contribute less than 5%. Across all three periods bands, more than 80% of windows correspond to body-wave data. For a given period band, the vertical component always provides more data than the horizontals. If not balanced, these differences between categories can cause regions sensitive to body waves to be updated more than regions sensitive to surface waves and slow down the overall convergence rate.

We define the weighted misfit for each category as

$$\Phi_c = \sum_{s=1}^S \sum_{r=1}^{R_{sc}} \sum_{w=1}^{N_{scr}} \omega_s \omega_c \omega_{scr} \omega_{scrw} \chi_{scr} \quad (4.30)$$

In Fig. 4.8, we calculate the percentage of the summed misfit for each category using two weighting strategies: (1) Orange bars correspond to category-only weighting, and (2) black bars correspond to the full category- and geographical-weighting strategy.

In the first case, after employing the category-weighting strategy in which the misfit is normalized by the total number of data in each category (Fig. 4.7), misfits from different categories are better balanced and do not vary dramatically from category to category. Although the summed weights themselves are equal in each category, the weighted misfits from each category are not. The weighted misfits of short-period body waves are on average 2 to 3 times larger than the misfits of long-period body and surface waves. We attribute this to the larger number of updates required to fit short-period phases compared with long-period phases, and we expect the body-wave misfits to decrease as the inversion progresses.

In the second case, when geographical weighting is applied, the distribution of misfits in each category does not significantly change, meaning that the re-balancing happens only within each category, as desired.

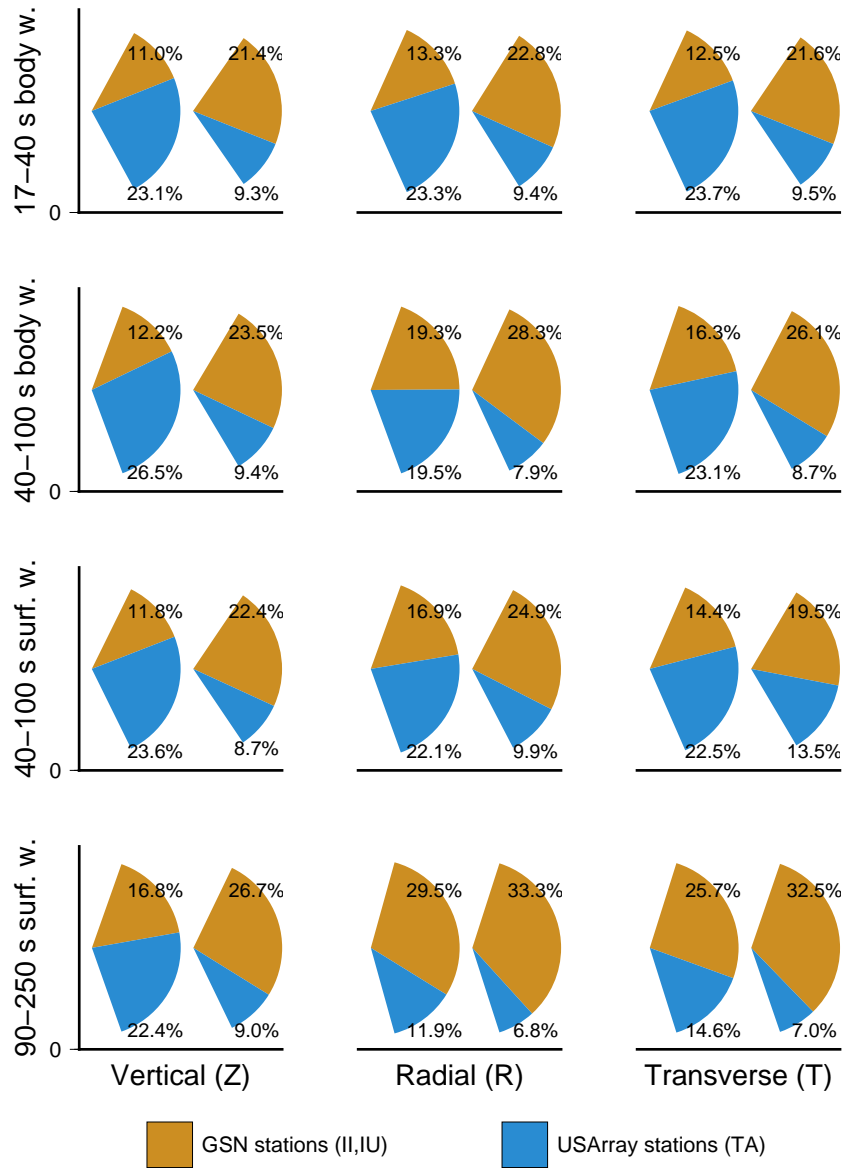


Figure 4.9: Percentage of the misfit of GSN stations (II, IU) and USArray stations (TA) in each category using category-weighting (left wedges in each panel) and geographical-weighting strategies (right wedges in panel). Compared with the category-weighting strategy, the geographical-weighting strategy assigns more weight to GSN stations and down weights USArray stations in all categories.

To further probe the overall re-balancing within each category, we compare the contribution to the total misfit from two seismographic networks: USArray (network ID TA) and GSN (network IDs II and IU). USArray stations are densely distributed across North America and GSN stations are sparsely distributed across the globe.

The total misfit from USArray or GSN stations in each category is given by

$$\Phi_c^{\text{USArray} / \text{GSN}} = \sum_{s=1}^S \sum_{r=1}^{R_{sc}} \sum_{w=1}^{N_{scr}} \omega_s \omega_c \omega_{scr} \omega_{scrw} \chi_{scr}^{\text{USArray} / \text{GSN}} \quad (4.31)$$

Fig. 4.9 shows the percentage of Φ_c^{USArray} and Φ_c^{GSN} in each category under different weighting strategies. In the category-weighting strategy, GSN stations contribute much less to the overall misfit than USArray stations, reflecting the proportionality to the amount of data, as expected. In the geographical-weighting strategy, the contribution of GSN stations is enhanced due to the re-balancing.

To further illustrate the effects of weighting, we selected 42 events for a pilot test and examined the model update gradient. Ideally, we should run forward and adjoint simulations for each of the 12 categories for one weighting strategy, and repeat this process for the other weighting strategy, which would require 2,016 simulations in total. To save computational cost while keeping the test meaningful, we considered only three categories, 17–40 s, 40–100 s, and 90–250 s, and ignored wave types for the adjoint simulations. Fig. 4.10 shows cross sections of the model update gradient. In the shortest period band (17–40 s), the gradient based on category-weighting is dominated by regions beneath Fiji Tonga and North America, with limited updates in the southern hemisphere. In contrast, the geographical-weighting approach results in a balanced gradient with more information in the southern hemisphere and relatively reduced sensitivity beneath Fiji Tonga and North America. The longer period bands, involving mostly surface waves, demonstrate similar behavior but more focused on the shallow mantle. Upon combining all three categories, we clearly see that the model

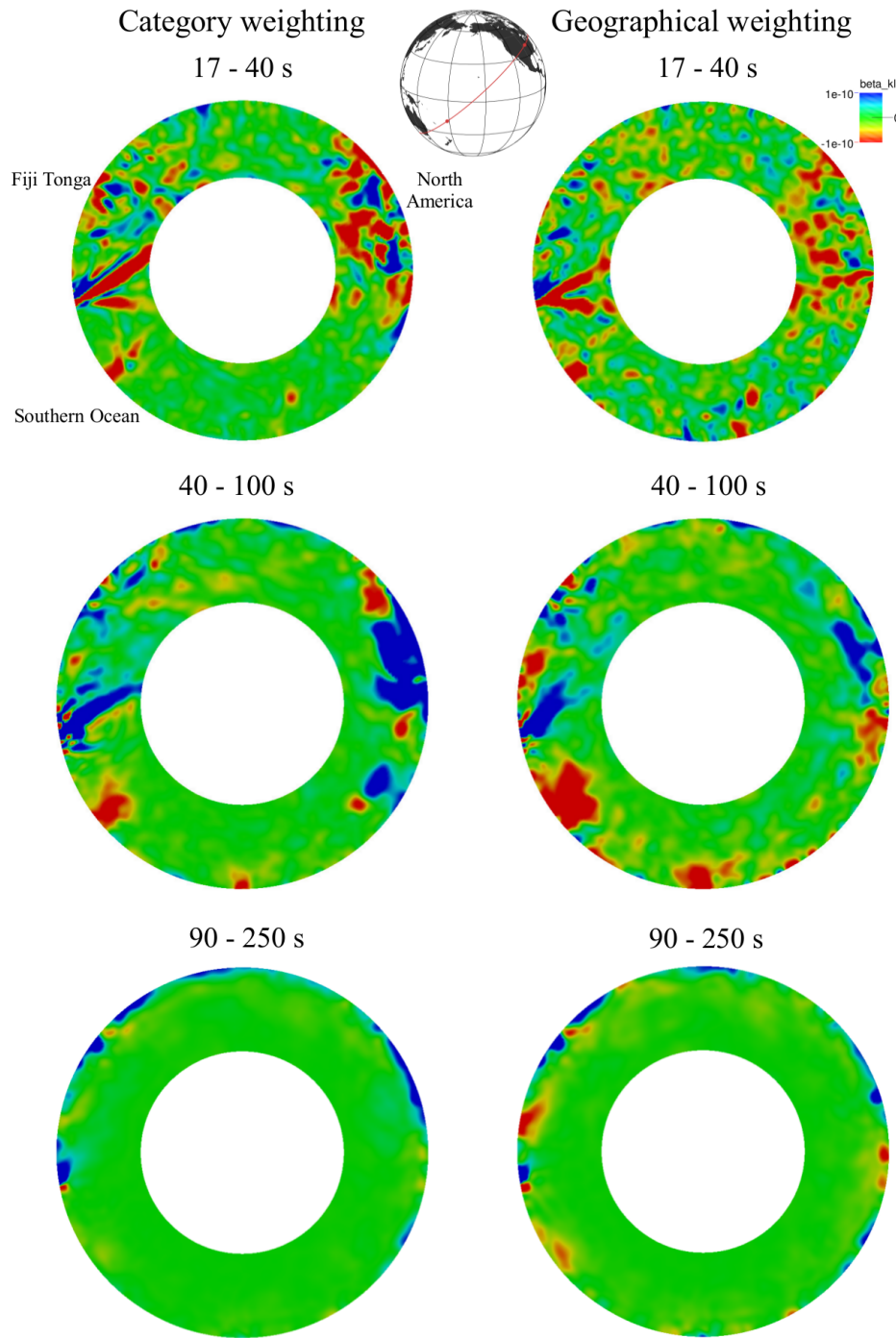


Figure 4.10: Smoothed gradient contributions using data from 42 earthquakes without (Left Column) and with source & receiver weighting (Right Column) in three period bands: 17–40 s (Top Row), 40–100 s (Middle Row), and 90–250 s (Bottom Row). The top center map shows the cross section with red line for reference. The isotropic smoothing length scale is 100 km.

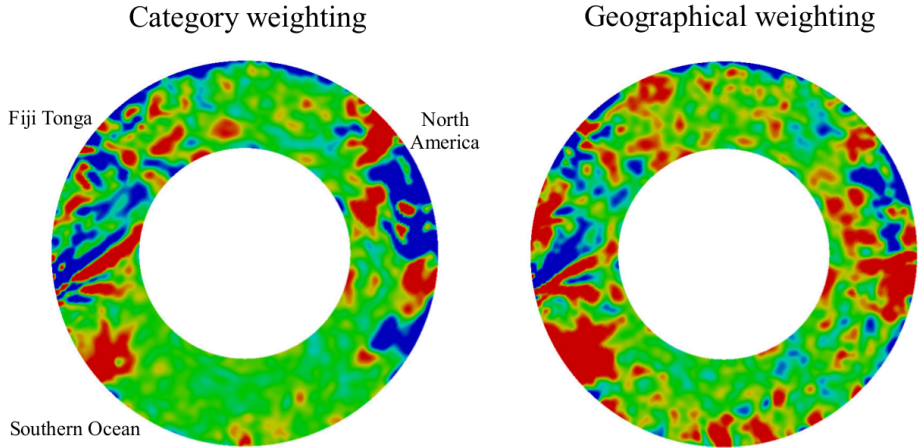


Figure 4.11: Example of a smoothed misfit gradient (weighted summation of the contributions of the three period bands shown in Fig. 4.10) using data from 42 earthquakes without (Left) and with source & receiver weighting (Right). The isotropic smoothing length scale is 100 km.

update based on the geographical weighting strategy is better balanced, with a more even sampling of the whole mantle (Fig. 4.11). From this pilot test we conclude that the geographical-weighting strategy effectively balances the inversion and improves the convergence rate, which is necessary for any inversion dealing with the unevenly distributed data.

4.7 Conclusion

We propose a geographic weighting strategy to address uneven data coverage in seismic tomography. To test the approach, we performed synthetic 2D global adjoint tomography experiments using realistic source and receiver distributions. The results show that geographical weighting performs better than category-only weighting and conventional diagonal model-space preconditioning. A 42-event pilot test was used to illustrate how geographical weighting balances densely and sparsely sampled regions. Finally, using a database of 1,480 earthquakes, we performed a statistical analysis of 17 million measurements assimilated in the global adjoint tomography inversion

of [67], verifying expected effects of the weighting scheme. As more data from dense regional seismographic networks become available, we expect weighting to play an increasingly important role in scientific studies of Earth's interior [99].

Chapter 5

Global Adjoint Tomography – Model GLAD-M25

Note

This paper was submitted as a paper entitled "Global Adjoint Tomography – Model GLAD-M25" by Lei, Wenjie and Ruan, Youyi and Bozdağ, Ebru and Peter, Daniel and Lefebvre, Matthieu and Komatitsch, Dimitri and Tromp, Jeroen and Hill, Judith and Podhorszki, Norbert and Pugmire, David to *Geophysical Journal International*, 2019.

5.1 Summary

Building on our first-generation global adjoint tomography model, GLAD-M15 [12], we present our second-generation transversely isotropic global model, named GLAD-M25, which is the result of ten quasi-Newton tomographic iterations with an earthquake database consisting of 1,480 events in the magnitude range $5.5 \leq M_w \leq 7.2$, an almost six-fold increase over the first-generation model. We calculated fully 3D synthetic seismograms with a shortest period of 17 s based on a GPU-accelerated spectral-element wave propagation solver which accommodates effects due to 3-D

anelastic crust & mantle structure, topography & bathymetry, the ocean load, ellipticity, rotation, and self-gravitation. We used an adjoint-state method to calculate Fréchet derivatives in 3D anelastic Earth models facilitated by a parsimonious storage algorithm. The simulations were performed on the Cray XK7 “Titan” at the Oak Ridge Leadership Computing Facility. We quantitatively evaluated GLAD-M25 by assessing misfit reductions and traveltimes & amplitude anomaly histograms in twelve measurement categories. We performed similar assessments for a held-out data set consisting of 360 earthquakes, with results comparable to the actual inversion. We compare GLAD-M25 with numerous other global and regional models, and highlight a variety of plumes and subduction zones.

5.2 Introduction

Construction of the first seismic tomographic models of the Earth dates back to the late 1970s [1, 31, 118] and early 1980s [145, 95]. Around the same time, [5], [64], and [123] formulated and adapted the theory of adjoint-state methods [19] for exploration seismology with the goal of capturing the full physics of seismic wave propagation. Mainly due to computational challenges, it took until the late 2000s to see the first applications of adjoint-state methods in regional- and continental-scale earthquake seismology [121, 34, 153]. The first global “adjoint tomography” model of the Earth’s mantle, GLAD-M15, was published in 2016 [12], more than 30 years after the development of the original “full waveform inversion” (FWI) theory.

Current global seismic models are in general agreement regardless of data type and inversion strategy in terms of long-wavelength heterogeneity [109, 130, 7]. However, discrepancies between models become noticeable as resolution increases. Using accurate 3D simulations of seismic wave propagation and the computation of data sensitivities in 3D background models are key requirements for improving resolution

in tomographic images on all scales. Such detailed images are essential for understanding mantle dynamics and related surface tectonic processes —for example the origin of hotspots and the forces behind plate motions and earthquakes. Higher resolution wavespeed models are also important for accurately locating earthquakes, and are required from an engineering point of view to assess seismic hazard in earthquake prone regions and to detect nuclear explosions.

With these goals in mind, in this study we use a GPU-accelerated version of the 3D spectral-element solver SPECFEM3D_GLOBE [55, 56] on the Cray supercomputer “Titan” at the Oak Ridge Leadership Computing Facility (OLCF) for global adjoint tomography. These simulations accommodate the full 3D complexity of global Earth models, including 3D anelastic crust and mantle structure, self-gravitation, rotation, ellipticity, topography & bathymetry, and the load of the oceans. No compromises are made with regards to resolving the Earth’s crust, which is explicitly captured by the spectral-element mesh [134], thereby eschewing the need for ubiquitous “crustal corrections”. The ultimate goal is to use every single piece of information in seismograms, a task made partly feasible based on the automated window selection tool FLEXWIN [79].

Global adjoint tomography has a well-defined but complex workflow with multiple stages. It is essential to optimize, automate, and harden the entire process using workflow management tools, especially with large data sets. For each iteration, 1,480 forward and adjoint simulations need to be performed, generating a few Petabytes of wavefield files for the parsimonious-storage kernel calculation algorithm of [59], and consuming 16 million OLCF node hours. How to deal with hardware failures during this process is critical to prevent contamination of the inversion results. For these reasons, we use EnTK as our workflow management engine [4]. This workflow engine can automatically detected job failures, both from the high-performance computing

(HPC) system and via user-defined functions. This facilitates tracking of tasks and semi-automatic job resubmission if necessary.

In this article we compare the results of our inversion with a number of previous tomographic models. On a global scale, we present comparisons with model S362ANI+M [91], which is an updated version of model S362ANI [63], the starting model for the GLAD-M15 inversion. We also consider global shear wavespeed models S40RTS [108], TX2015 [74], SEMUCB-WM1 [38], and SL2013sv [112], as well as compressional wavespeed models LLNL-G3Dv3 [119], GAP-P4 [41], and UU-P07 [139]. On the scale of North America we make comparisons with models US22 [155], a radially anisotropic model based on adjoint tomography using USArray data from 180 regional earthquakes, and SL2013NA [113], a modification of global model SL2013sv focused on North America. In Europe we use regional model EU60 [154] for comparison, which is based on the assimilation of data from 190 regional earthquakes recorded by more than 700 European seismographic stations. Finally, in Asia we use regional adjoint tomography model EARA2014 [20] as a reference, a model based on data from 227 earthquakes recorded by more than 1,800 stations.

This article is organized as follows. Sections 5.3–5.5 describe the starting model, earthquake database, and seismographic data set. Sections 5.6 and 5.7 describe the misfit function minimized during the inversion process and the related model parameterization. In Section 5.8 we describe the adjoint tomography workflow in some detail. Section 5.9 describes the evolution of the misfit, and in Section 5.10 we evaluate the model based on a held-out data set of 360 earthquakes. Finally, in Section 5.11, we describe the model in detail, offering many comparisons with various global and regional models, as described in the proceeding paragraph. We conclude with a discussion of future opportunities and directions.

5.3 Starting model GLAD-M15

As a continuation of our previous work [12], we used the first-generation model GLAD-M15 as our starting model. GLAD-M15 is a 3D transversely isotropic earth model, which combined 3D mantle model S362ANI [63] with 3D crustal model CRUST2.0 [6] as its starting model. In this study, we continue to use the same transversely isotropic model parametrization. Instead of relying on crustal corrections, the mesh implementation of the crust in the spectral-element solver SPECFEM3D_GLOBE [55, 56, 102] enables us to accurately accommodate topography and bathymetry as well as variations in the Moho. GLAD-M15 was constructed using a global database of 253 earthquakes. The first 12 iterations of the GLAD-M15 inversion used three-component seismograms with a shortest period of 27 s, and the final 3 iterations reduced this further to 17 s. In this study we also used three-component seismograms with a shortest period of 17 s.

5.4 Earthquakes

In addition to the 253 earthquakes used for the construction of GLAD-M15, we initially carefully selected 784 additional earthquakes from the global Centroid-Moment Tensor (CMT) catalog [32], resulting in a total number of 1,040 earthquakes. To ensure a good signal-to-noise ratio on a global scale, the smallest moment magnitude in the database is set to 5.5, thereby capturing more deep events, and, to avoid complications associated with source dimension and directivity, the largest moment magnitude is set to 7.2.

Before using the 1,040 earthquakes in our structural inversion, we performed CMT inversions using model GLAD-M15, the results of which are summarized in Fig. 5.1. To ensure even global coverage, we used seismographic stations from the Global Seismic Network (II, IU, IC, US, CU, and GT), GEOFON (GE), GEOSCOPE (G), and

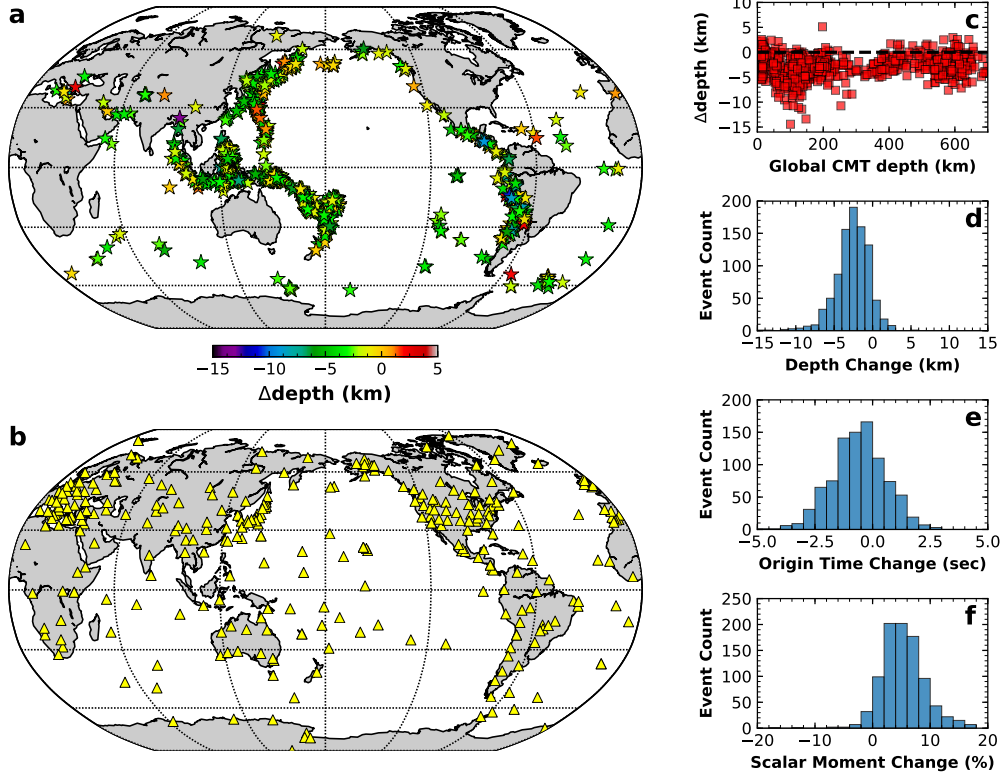


Figure 5.1: Source corrections for 1,040 out of 1,480 events used in the structural inversion. (a) Map view of depth changes. (b) Distribution of seismographic stations used for source inversions. (c) Depth change relative to the original global CMT Catalog depth. (d)–(f) Histograms of depth, origin time, and scalar moment changes relative to the CMT Catalog.

several regional networks, such as MedNet (MN), the Brazilian Lithospheric Seismic Project (BL), the Chilean National Seismic Network (C), and the Japan Meteorological Agency Seismic Network (JP) (Fig. 5.1b). The number of stations used for CMT inversion usually ranges from 150 to 500.

To determine the source parameters in the starting model, we used the CMT inversion algorithm of [72]. This algorithm combines a normalized waveform difference misfit with an envelope difference misfit. Specifically, the algorithm minimizes the

misfit function

$$\Phi = \sum_{c=1}^C \omega_c \sum_{r=1}^{R_c} \omega_{cr} \sum_{w=1}^{W_{cr}} \left\{ \lambda \frac{\int [d_w(t) - s_w(t - \Delta t)]^2 dt}{\int [d_w(t)]^2 dt} + (1 - \lambda) \frac{\int [e(d_w(t)) - e(s_w(t - \Delta t))]^2 dt}{\int [e(d_w(t))]^2 dt} \right\}, \quad (5.1)$$

where $d_w(t)$ denotes data in time window w , and $s_w(t - \Delta t)$ the corresponding synthetic for model GLAD-M15. We allow the synthetics to shift relative to the data by an amount Δt — effectively a station correction — determined by cross correlation. The envelope function is denoted by $e(\cdot)$, and the parameter λ determines the balance between fitting waveforms versus fitting envelopes. The number of measurement categories is denoted by C . Following [32], seismograms were filtered between 50 s and 100 s to select three-component body-wave windows, and between 60 s and 100 s to select three-component surface-wave windows, resulting in six measurement categories, $c = 1, \dots, C$. To balance their contributions, each category is weighted by the reciprocal of the number of measurements in that category, ω_c . The number of windows for a given receiver r in a given measurement category c is W_{cr} . Each such window is weighted equally, i.e., $\omega_{crw} = 1$. The number of receivers that records data in category c is denoted by R_c . As shown in Fig. 5.1b, the receivers are unevenly distributed across the globe, with several dense arrays in the Northern Hemisphere and poor coverage in the Southern Hemisphere. To balance the coverage, following a strategy articulated by [111], we assign receiver weights ω_{cr} based on the expression

$$\omega_{cr}^{-1} = N_c \sum_{r'=1}^{R_c} \exp \left[- \left(\frac{\Delta_{rr'}}{\Delta_c} \right)^2 \right] \quad , \quad (5.2)$$

where N_c is a normalization factor for category c , and where $\Delta_{rr'}$ denotes the angular distance between receivers r and r' . The reference angular distance Δ_c for each cat-

egory c needs to be chosen such that the condition number of the diagonal weighting matrix defined by Eqn. (5.2) is not too large. The calculation of the weights may be abstracted as: given a distribution of points on the unit sphere, determine a spatial weighting associated with each point.

The algorithm inverts for the six elements of the moment tensor and the centroid location (latitude, longitude, and depth). These source inversions are computationally very expensive, because for each of the 1,040 events nine full 3D forward simulations are required to obtain the source parameter Fréchet derivatives.

Because we allow the synthetics to shift in phase by an amount Δt relative to the data, the CMT inversion has unreliable sensitivity to the centroid time. To alleviate this problem, following [153], we perform a subsequent grid search for the centroid time and the scalar moment. The grid-search calibration involves simple shift and multiply operations on seismograms and, unlike the CMT inversion, requires minimal simulation time.

Most earthquakes show a shallower depth after inversion (Fig. 5.1c), consistent with our previous experiences [154, 20, 12] and with experiments by [51]. We observed an average depth change of -2.62 ± 2.49 km relative to the global CMT solutions, an average scalar moment change of $5.31 \pm 3.91\%$, and an average centroid time shift of -0.60 ± 1.17 s. These are relatively minor corrections, especially in view of the significant expense of the source inversions. For this reason, when we added another 440 earthquakes during iteration 22, thereby bringing the total to 1,480 events, we only performed a grid search to calibrate the centroid times and scalar moments. Fig. 5.2 summarizes the characteristics of all 1,480 earthquakes used in this study.

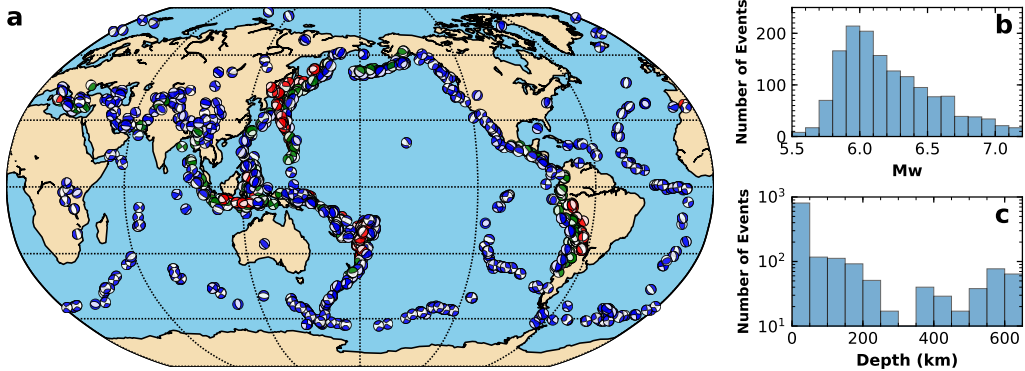


Figure 5.2: The 1,480 earthquakes used in this study. (a) Distribution of earthquakes. The color of each beach ball reflects its depth range, where blue designates events shallower than 50 km, green events between 50 km and 300 km, and red events deeper than 300 km. (b) & (c) Histograms of earthquake moment magnitudes and depths.

5.5 Seismic data

The seismographic stations used in this study were carefully selected to ensure global coverage and high data quality (Fig. 5.3). In addition to the seismographic stations used for the source inversions, we included all available data for our 1,480 event earthquake database from many data centers, including IRIS, ORFEUS, INGV, IPGP, ETH, and GEONET. Regional and temporary networks, such as US Array (TA), Africa Array (AF), the Canadian National Seismograph Network (CN), Geoscience Australia (AU), the Antarctic Seismographic Argentinean Italian Network (AI), and the New Zealand National Seismograph Network (NZ), constitute a significant part of our database and greatly improve coverage in certain regions.

5.5.1 Adaptable Seismic Data Format

Conventional seismic data formats, such as SAC, involve one file per time series plus related files with instrument response and event information. Since every earthquake in the database is typically recorded by thousands of instruments, I/O during the preprocessing stage of the adjoint tomography workflow quickly cripples the file sys-

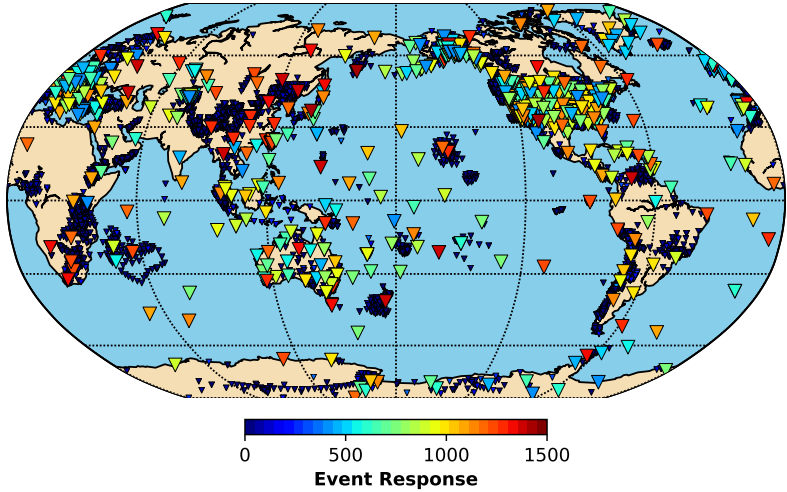


Figure 5.3: Distribution of the 11,800 seismographic stations used in this study. Colors denote the number of events for which a given station contributes waveforms to the structural inversion. Stations with a number of event responses < 400 are plotted in smaller size; these are usually temporary arrays deployed over a short period of time, frequently ocean bottom seismometers. The maximum number of event responses comes from ANMO, in Albuquerque, New Mexico, which contributed to 1,442 out of 1,480 earthquakes in the data set.

tem. The Adaptable Seismic Data Format (ASDF) [61] was developed with complete reproducibility and fast parallel processing in mind.

In this context, there are four key issues ASDF resolves.

- Robustness and stability: the data container is developed and maintained to ensure accuracy of scientific results.
- Data organization: the container is self-describing. Data, including waveform, source, and station information, are organized into well-defined structures.
- Reproducibility: the container enables scientists to keep track of which operations have been performed on the data so that results can be reproduced.
- Efficiency: the format provides easy mechanisms for parallel processing.

ASDF serves as a self-contained-and-explained data container while taking full advantage of parallel computing. In our workflow, one ASDF file contains all the

information needed for processing one event, including the seismic traces, an event information file (in QuakeML format), and station response files (in StationXML format). The related Application Programming Interfaces (API)s are carefully designed for easy data extraction and parallel processing.

5.6 Misfit function

The misfit function to be minimized during the iterative inversion process must be carefully constructed. In this study, it typically involves cross-correlation traveltimes for body waves and frequency-dependent multitaper phase measurements for surface waves. Measurements are made in several passbands of three-component seismograms rotated into vertical, radial, and transverse components, resulting in a number of measurement categories. In this study, we consider four passbands, namely, a 17–40 s passband targeting body waves, two 40–100 s passbands separately targeting body and surface waves, and a 90–250 s passband targeting longer-period surface waves. Each passband involves measurements on all three components, which results in a total of twelve measurement categories. Although the inversion is designed to minimize the overall misfit, we track the misfit reduction in each of the categories to ensure that the model is improving the fit to the data roughly equally across the board. One of the biggest challenges in the construction of the misfit function is the highly uneven distribution of earthquakes — discussed in Section 5.4 — and seismographic stations, which must be counterbalanced by geographically weighting the data. This issue is discussed in detail by [111]; in this section we present a brief synopsis.

With these considerations in mind, the overall misfit, Φ , is defined as follows:

$$\Phi = \sum_s^S \omega_s \sum_c^C \omega_c \sum_r^{R_{sc}} \omega_{scr} \sum_w^{W_{scr}} \omega_{scrw} \chi_{scrw} , \quad (5.3)$$

where S denotes the number of sources, C the number of categories, R_{sc} the number of receivers recording source s in category c , and W_{scr} the number of measurement windows for source s , category c , and receiver r . The misfit for a specific source s , category c , receiver r , and window w is

$$\chi_{scrw} = \frac{1}{\Delta\omega} \int_{\omega_1}^{\omega_2} \left(\frac{\Delta\tau_{scrw}}{\sigma_{scrw}} \right)^2 d\omega , \quad (5.4)$$

where $\Delta\tau_{scrw}$ denotes a multi-taper frequency-dependent phase measurement over the frequency interval $\Delta\omega = \omega_2 - \omega_1$, with associated uncertainties σ_{scrw} . For body waves, the window misfit is often simply the cross-correlation traveltime anomaly, ΔT_{scrw} , weighted by its standard deviation, i.e., $\chi_{scrw} = (\Delta T_{scrw}/\sigma_{scrw})^2$. As in the source inversions, the window weights are equal, $\omega_{scrw} = 1$, and the category weight, ω_c , is the reciprocal of the number of measurements in that category, $1/C$. Earthquakes mainly occur along plate boundaries, and most seismographic stations are confined to the continents, which leads to a very uneven distribution of sources and stations, as illustrated in Figs. 5.2 and 5.3. Therefore, weighting is crucial in global tomography to balance this uneven sampling of Earth's interior. Our source and receiver weighting strategy, encapsulated by the weights ω_s and ω_{scr} , is developed to compensate for uneven spatial sampling. Following the same strategy as for the receiver weights in the source inversions, we define source and receiver weights as

$$\omega_s^{-1} = N \sum_{s'=1}^S \exp \left[- \left(\frac{\Delta_{ss'}}{\Delta} \right)^2 \right] , \quad (5.5)$$

and

$$\omega_{scr}^{-1} = N_{sc} \sum_{r'=1}^{R_{sc}} \exp \left[- \left(\frac{\Delta_{rr'}}{\Delta_{sc}} \right)^2 \right] , \quad (5.6)$$

respectively. Here N and N_{sc} are normalization factors, and $\Delta_{ss'}$ and $\Delta_{rr'}$ denote angular distances between source and receiver pairs $\{s, s'\}$ and $\{r, r'\}$. The reference

angular distances Δ and Δ_{sc} need to be chosen based on the condition numbers of the diagonal weighting matrices defined by Eqns. (5.5) and (5.6).

5.7 Model parameterization

We use the same transversely isotropic model parametrization as starting model GLAD-M15. Such a model is described by the five Love parameters A, C, L, N , and F [73], or, alternatively, using the mass density ρ , in terms of the wavespeeds $\alpha_v = \sqrt{C/\rho}$, $\alpha_h = \sqrt{A/\rho}$, $\beta_v = \sqrt{L/\rho}$, $\beta_h = \sqrt{N/\rho}$ and the dimensionless parameter $\eta = F/(A - 2L)$ [30, 24]. Assuming the radial anisotropy is due to shear anisotropy, these five parameters may be further reduced to four by introducing the bulk sound speed, $c = \sqrt{\kappa/\rho}$. Therefore, the final four parameters are c, β_v, β_h , and η . Transverse isotropy is confined to the upper mantle; the lower mantle is assumed to be isotropic.

Since density is difficult to constrain with seismic data, density perturbations are scaled to isotropic (Voigt averaged) shear wavespeed perturbations based on the relationship $\delta \ln \rho = 0.33 \delta \ln \beta$ [88].

Based on this parametrization, the variation in the misfit function (5.3) may be expressed as [154, 12]

$$\delta\Phi = \int_V (\delta \ln c K_c + \delta \ln \beta_v K_{\beta_v} + \delta \ln \beta_h K_{\beta_h} + \delta \ln \eta K_\eta) dV , \quad (5.7)$$

where $K_c, K_{\beta_v}, K_{\beta_h}$, and K_η denote the four Fréchet derivatives, which are calculated based on an adjoint-state method [103, 135].

5.8 Adjoint tomography workflow

The adjoint tomography workflow is depicted in Fig. 5.4. It starts with the selection of earthquakes, as discussed in Section 5.4. Given the earthquake selection, observed seismographic data and related response information are acquired, as discussed in Section 5.5. For a given earthquake, the corresponding seismograms and related response information are combined in a single ASDF file, described in Section 5.5.1. For a given earthquake data set, the conversion to ASDF needs to be performed once and for all. In the following sections we highlight several important aspects of the workflow.

5.8.1 Forward simulations

The observed seismograms need to be compared to corresponding synthetic seismograms for the purpose of making measurements. The forward simulations are based on the global spectral-element solver SPECFEM3D_GLOBE [55, 55], and take a CMT solution, a relevant list of stations, and the current earth model as input. The solver is GPU accelerated, and the simulations are performed on the Cray supercomputer “Titan” at the OLCF. To simulate 120-min seismograms with a shortest period of 17 s on 384 NVIDIA Tesla K20X GPUs takes approximately 10 min of wall clock time.

The calculation of Fréchet derivatives requires access to snapshots of the forward wavefield as part of the parsimonious storage algorithm developed by [59], with rapid I/O facilitated by ADIOS [70]. For the current simulation setup, this requires about 1 TB of storage per earthquake, so for 1,480 earthquakes this adds up to 1.5 PB. This volume of data is generated during \sim 6 hours of simulations. Based on our experience, ADIOS is capable of achieving \sim 120 GB/s of sustained I/O on OLCF resources. Given that typical write speeds for modern hard disks are \sim 100 MB/s,

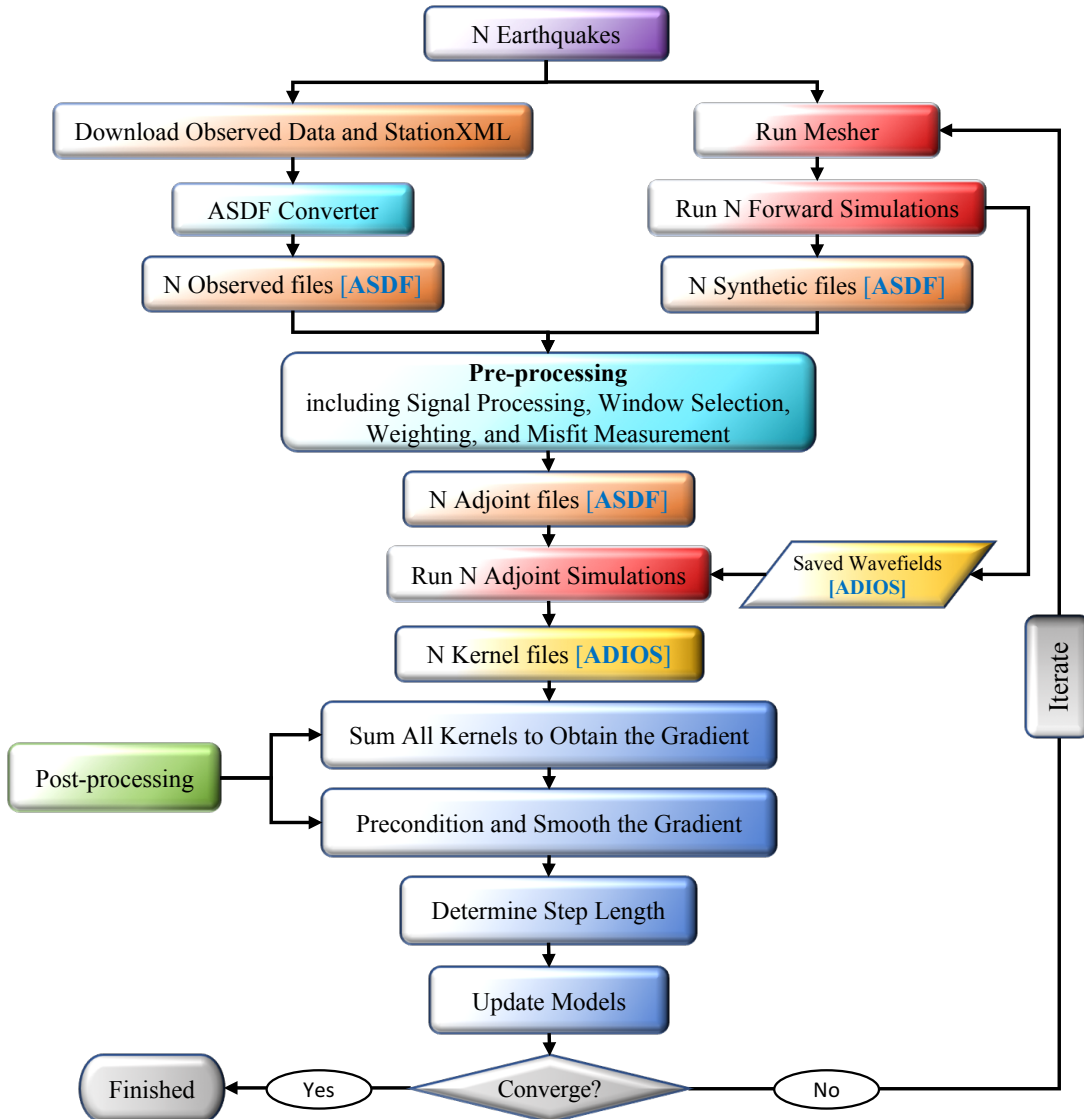


Figure 5.4: Adjoint tomography workflow.

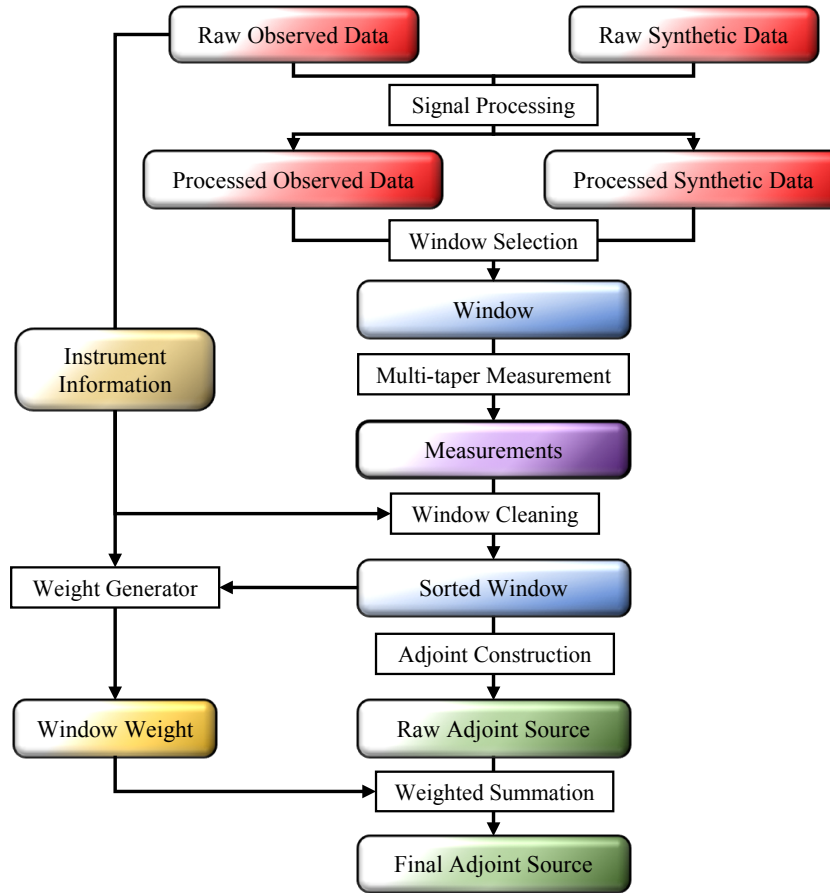


Figure 5.5: Sub-workflow workflow for preprocessing seismic data.

it would be extremely difficult to carry out global adjoint tomography without the ADIOS library.

5.8.2 Seismic data processing

The seismic data preprocessing workflow takes raw observed and synthetic data as input, and generates adjoint sources for data assimilation as output. From a computational perspective, the preprocessing workflow consumes only 1% of the overall computational requirements. But from the perspective of the tomographic inversion, this is by far the most important stage of the adjoint tomography workflow, directly and fundamentally impacting the outcome. Any “bad data” assimilated at this stage may contaminate the gradient and ultimately the final model.

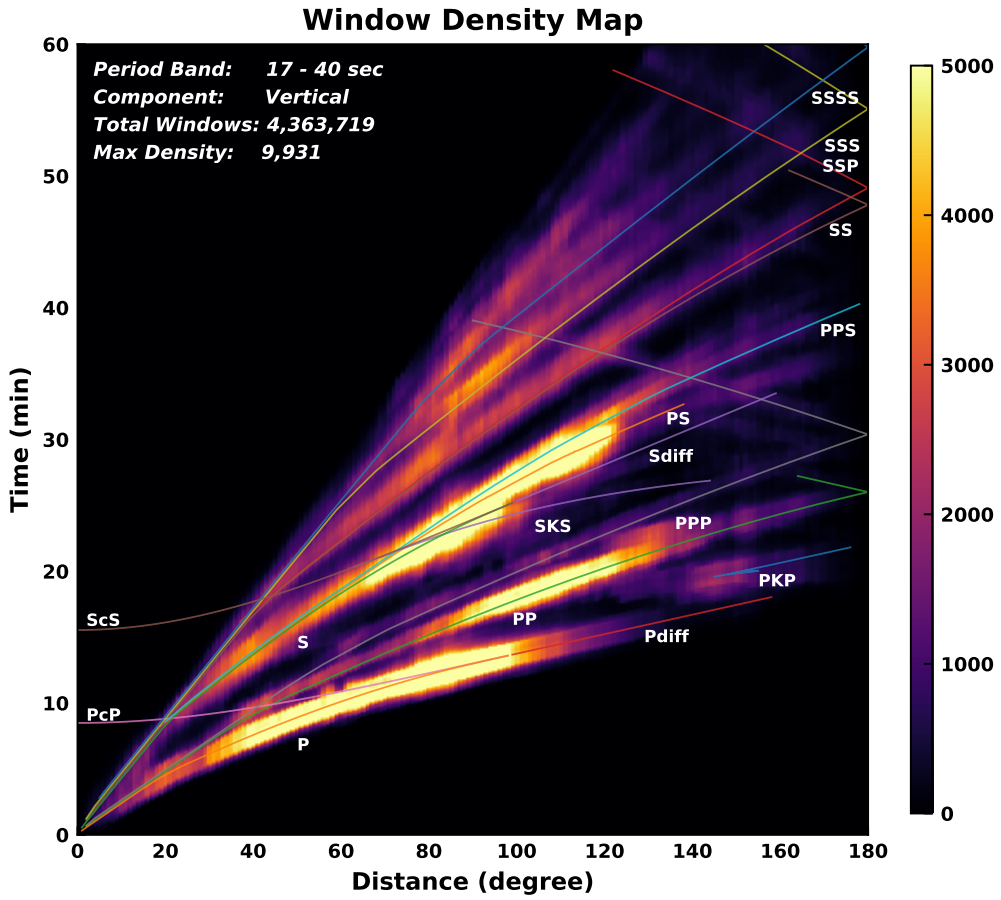


Figure 5.6: Time-distance plot for vertical component 17–40 s body waves showing a measurement window density map. A total of 4,363,719 time windows were discretized into 1 degree epicentral distance and 1 s time bins. The maximum window count is 9,931 in the 85–86° distance and 1,375–1,376 sec time bin. Major traveltime branches are labeled. Note that the plot contains data from events with a wide variety of depths, so the branches are for identification purposes only.

We use millions of seismograms generating tens of millions of measurement windows, making data selection through human interaction impossible. The preprocessing workflow automates this task, most importantly via the time window selection tool FLEXWIN [79]. Every seismogram and potential measurement goes through multiple checks and balances before acceptance or rejection.

As illustrated in Fig. 5.5, the preprocessing workflow includes the following phases.

1. Signal processing to remove the instrument response from observed data to recover ground displacement using ObsPy [8]. Both observed and synthetic data are bandpass filtered, and the horizontal components are rotated to obtain the radial and transverse components of motion.
2. Window selection on a pair of observed and synthetic seismograms. Pyflex (a Python version of FLEXWIN by krischer2015) is used to automatically generate windows where observed and synthetic data are sufficiently close to make measurements based on user defined criteria.
3. Cross-correlation travelttime or multi-taper phase measurements in selected windows.
4. Window sorting and cleaning based on statistical analyses of all measurements to eliminate outliers.
5. Preliminary adjoint source construction based on the sorted windows.
6. Calculation and assignment of weights, as discussed in Section 5.6.
7. Construction of the final, properly weighted, adjoint sources.

To illustrate which seismic phases end up being picked, Figs. 5.6, 5.7, and 5.8 show time-distance plots for vertical, radial, and transverse component 17–40 s body waves, respectively, in which the Pyflex window count is used to identify parts of seismograms being assimilated. The figures nicely highlight all the well known body travelttime branches. Collectively, the numerous compressional wave arrivals identified in Figs. 5.6 and 5.7 are of great importance, because they help constrain the compressional wavespeed structure in the model. The Pyflex window selection algorithm is currently configured not to pick body waves after the arrival of the surface waves, which is why the P_cP and S_cS branches are missing at shorter epicentral distances.

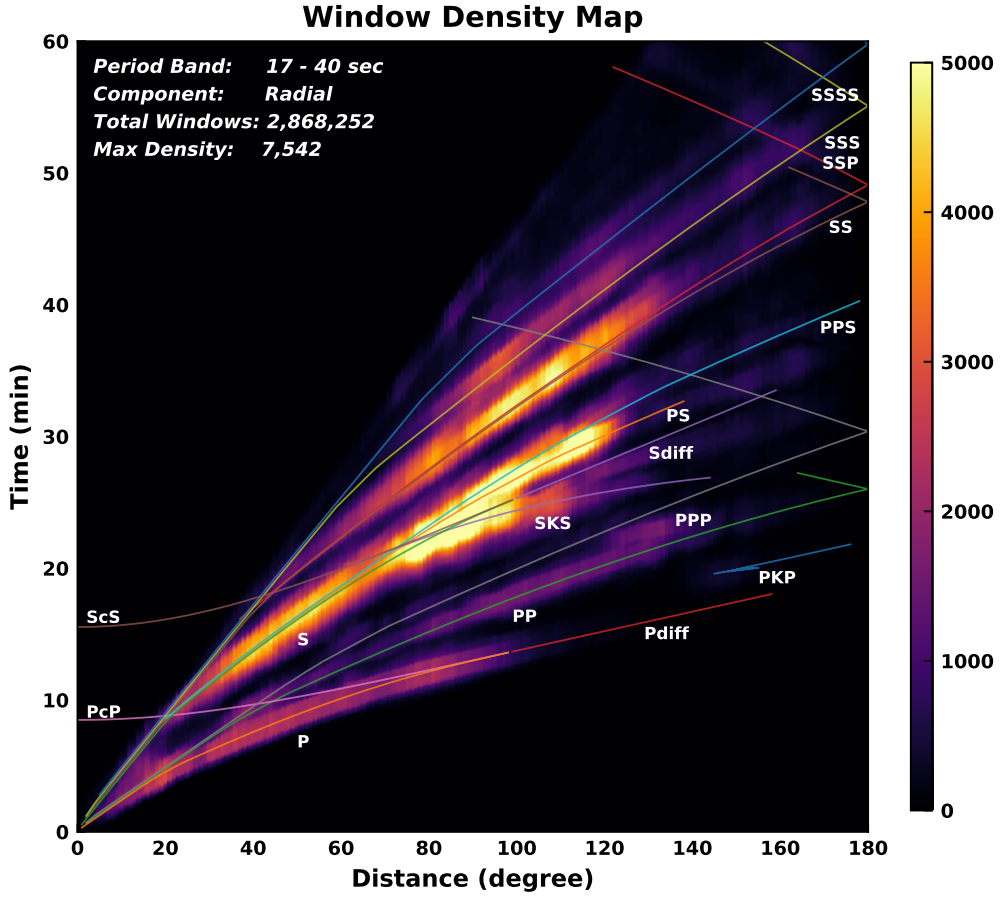


Figure 5.7: Same as Fig. 5.6, except for radial component 17–40 s body waves. A total of 2,868,252 time windows were discretized into 1 degree epicentral distance and 1 s time bins. The maximum window count is 7,542 in the 86–87° distance and 1,378–1,379 s time bin.

This is something we will reconsider in future applications, perhaps by introducing aspects of machine learning.

5.8.3 Adjoint Simulations

Collectively, the adjoint simulations are the most expensive stage of the workflow. Adjoint simulations take the adjoint sources as input, and generate Fréchet derivatives of the four model parameters as output. The computational cost of one adjoint simulation is roughly twice (~ 25 min) that of a forward simulation, since the for-

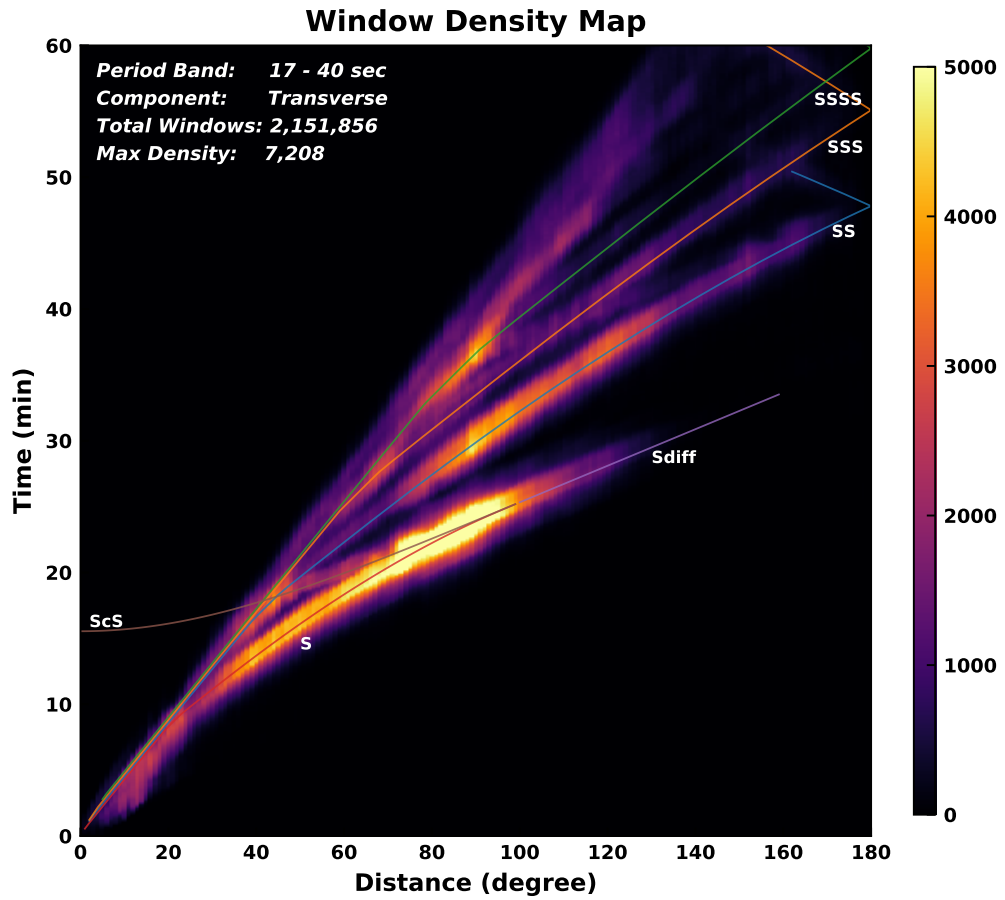


Figure 5.8: Same as Fig. 5.6, except for transverse component 17–40 s body waves. A total of 2,151,856 time windows were discretized into 1 degree epicentral distance and 1 s time bins. The maximum window count is 7,208 in the 89–90° distance and 1,398–1,399 s time bin. Only SH travetime branches are labeled.

ward wavefield is recalculated for convolution with the adjoint wavefield during the adjoint simulation. Using this procedure, both the forward and adjoint wavefield are calculated in forward time, and attenuation is accurately taken into account in both simulations.

5.8.4 Postprocessing

The postprocessing stage of the workflow takes Fréchet derivatives as input and generates a model update as output. It involves the follow steps.

1. Summation of the individual Fréchet derivatives for each earthquake to obtain the overall gradient of the misfit function. The contribution of each source is weighted to balance the uneven distribution of earthquakes based on the weighting strategy discussed in Section 5.6 .
2. Smoothing of the raw misfit gradient using a 3D Gaussian, which serves as a regularization procedure. Instead of using a changing smoothing radius based upon the “ray density” [12], we used a fixed value at a given iteration, following [153].
3. Preconditioning of the smoothed gradient based on a technique proposed by [78].
4. Line search to determine the magnitude of the model update. The search direction is determined using a nonlinear conjugate gradient method [148] (iterations 16–21) or a Limited-memory Broyden- Fletcher-Goldfarb-Shanno (L-BFGS) quasi-Newton method (iterations 22–25). We used a subset of 160 earthquakes to conduct the line search and determine the step length.

5.8.5 Workflow management

There are more than ten stages in the adjoint tomography workflow, and each stage involves thousands of small tasks. For every model iteration, we performed up to 1,480 forward and adjoint simulations, each involving hundreds of compute cores and graphics cards, as well as heavy I/O. The workflow is prone to human error and hardware failure, making it fragile [66]. For these reasons, we hardened the workflow by taking advantage of modern workflow management software. We selected EnTK as our workflow management engine [4], and developed complementary seismic tomography workflow tools. The workflow engine can automatically detect job failures both from the HPC system and via user-defined functions. This enables us to keep track of all tasks and semi-automatically resubmit jobs if necessary. Given that most HPC system time is spent waiting in the job queue, automatic failure detection and relaunching greatly shortens the overall time to solution.

5.9 Misfit evolution

The inversion went through ten iterations in a number of stages, as documented in this section. The evolution of the overall misfit function (5.3) as well as its behavior in the various measurement categories is summarized in Fig. 5.9.

5.9.1 Stage I: Iterations 15–17

Starting model GLAD-M15 was constructed using a database of 253 earthquakes. For iterations 15–17 of the inversion we used an expanded database of 520 events. Our focus was to validate and test our software and workflow before scaling up to a larger database of 1,040 events. For these iterations we used three period bands, namely, 17–40 s, 40–100 s, and 90–250 s, and we used a nonlinear conjugate gradient method to update the model.

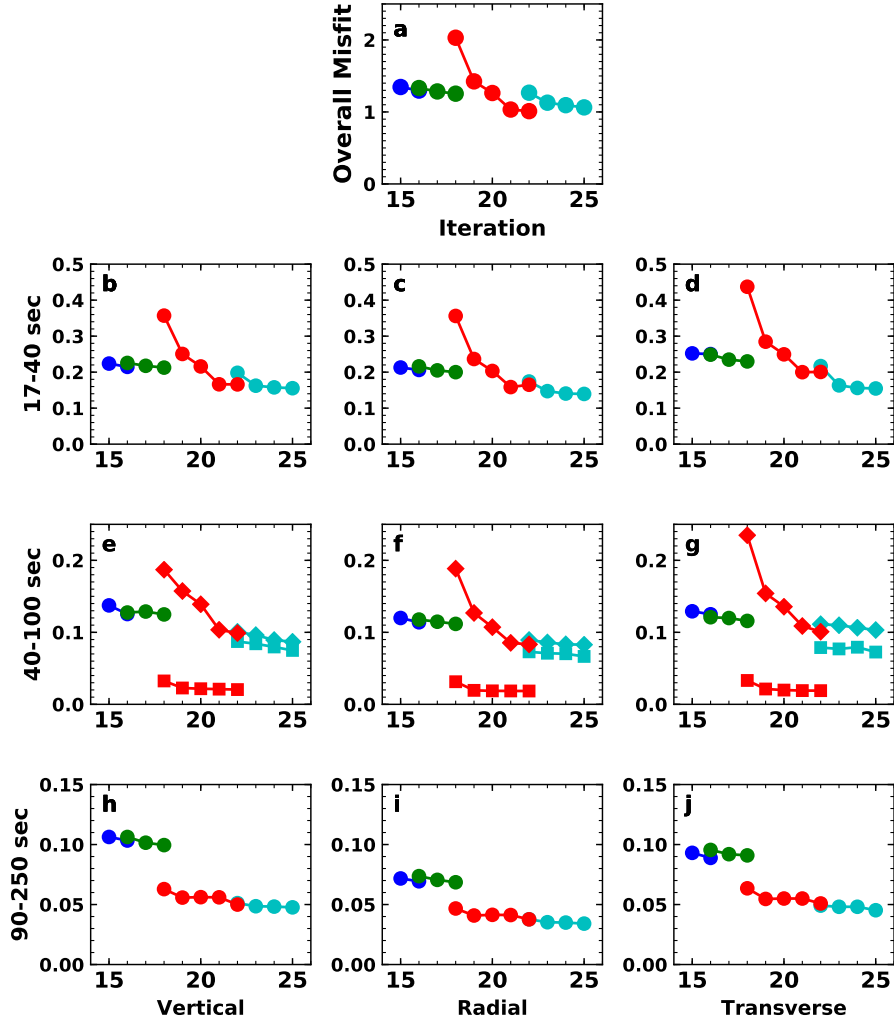


Figure 5.9: Evolution of the misfit function from GLAD-M15 to GLAD-M25. Each color denotes different stages of the inversion, as discussed in Sections 5.9.1–5.9.3. (a) Evolution of the total misfit. (b)–(j) Misfit in each period band (rows) on three components (columns). (e)–(g) Since iteration 18, we split the 40–100 s period band into two measurement categories: body waves (diamonds) and surface waves (squares).

5.9.2 Stage II: Iterations 18–21

We see an abrupt change in the value of the misfit function at iteration 18 in Fig. 5.9, reflecting the addition of 520 events to the inversion database, and a change in the weighting strategy for 40–100 s surface waves. For iterations 18–21 we split the 40–100 s period band into two, separating the body and surface waves (Figs. 5.9e–g). Since body and surface waves sample different parts of the mantle, this split facilitated more control over the spatial distribution of the model update. Because the 17th iteration model explains 40–100 s surface wave data relatively well, we reduced their weight on all three components for iterations 18–21, as indicated by the lower red curves in Figs. 5.9e–g.

The misfit reduction for 17–40 s body waves (Figs. 5.9b–d) tapers off by iteration 21, prompting us to add more earthquakes and change the weighting strategy again by reintroducing 40–100 s surface waves.

5.9.3 Stage III: Iterations 22–25

At iteration 22 we added another 440 earthquakes to the database, bringing the total to 1,480 events, and we changed the 40–100 s surface wave weights back to their setting in Stage I. During this stage we switched from a nonlinear conjugate gradient optimization algorithm to an L-BFGS quasi-Newton method.

5.9.4 Misfit assessment

In the previous sections we discussed the evolution of the misfit through three key stages of the inversion. It is important to note that “the misfit function” is, in fact, a continually moving target, because at every iteration the number of measurements increases as the model improves, and the number of earthquakes increases at iterations 18 and 22.

	Vertical (%)	Radial (%)	Transverse (%)
17–40 s body waves	19.1 (37.3)	23.7 (46.3)	28.2 (54.8)
40–100 s body waves	18.3 (37.5)	24.0 (51.4)	24.5 (54.5)
40–100 s surface waves	33.6 (69.6)	33.3 (71.5)	33.5 (77.2)
90–250 s all waves	15.7 (44.9)	14.4 (49.1)	29.6 (48.7)

Table 5.1: Changes in fit in the twelve measurement categories between the new model, GLAD-M25, and its starting model, GLAD-M15, and, in parentheses, between GLAD-M25 and model S362ANI combined with CRUST2.0, which was the starting model for the GLAD-M15 inversion.

In this section we calculate specific changes in misfit using all 1,480 earthquakes and an identical set of weights and windows for three models, namely, GLAD-M25, GLAD-M15, and S362ANI combined with CRUST2.0. Table 5.1 summarizes the changes in fit in the twelve measurement categories between the new model, GLAD-M25, and its starting model, GLAD-M15, and between GLAD-M25 and model S362ANI combined with CRUST2.0, which was the starting model for the GLAD-M15 inversion.

In all categories we observe significant misfit reductions, with dispersive 40–100 s surface waves exhibiting the largest improvements. The improvements in fit per component are comparable in all period bands, indicating that the various categories are reasonably well balanced in the assessment of misfit.

5.9.5 Histogram comparisons

Another way to evaluate model performance is by assessing the distribution of measurements in the various categories. Again we use all 1,480 events and a set of identical windows on all three components to assess GLAD-M25, GLAD-M15, and S362ANI combined with CRUST2.0. The total number of selected windows, determined using model GLAD-M25, exceeds 18 million. Fig. 5.10 shows histograms of the resulting phase measurements in all twelve measurement categories. We observe that the distributions generally become better centered on zero, and that all standard deviations

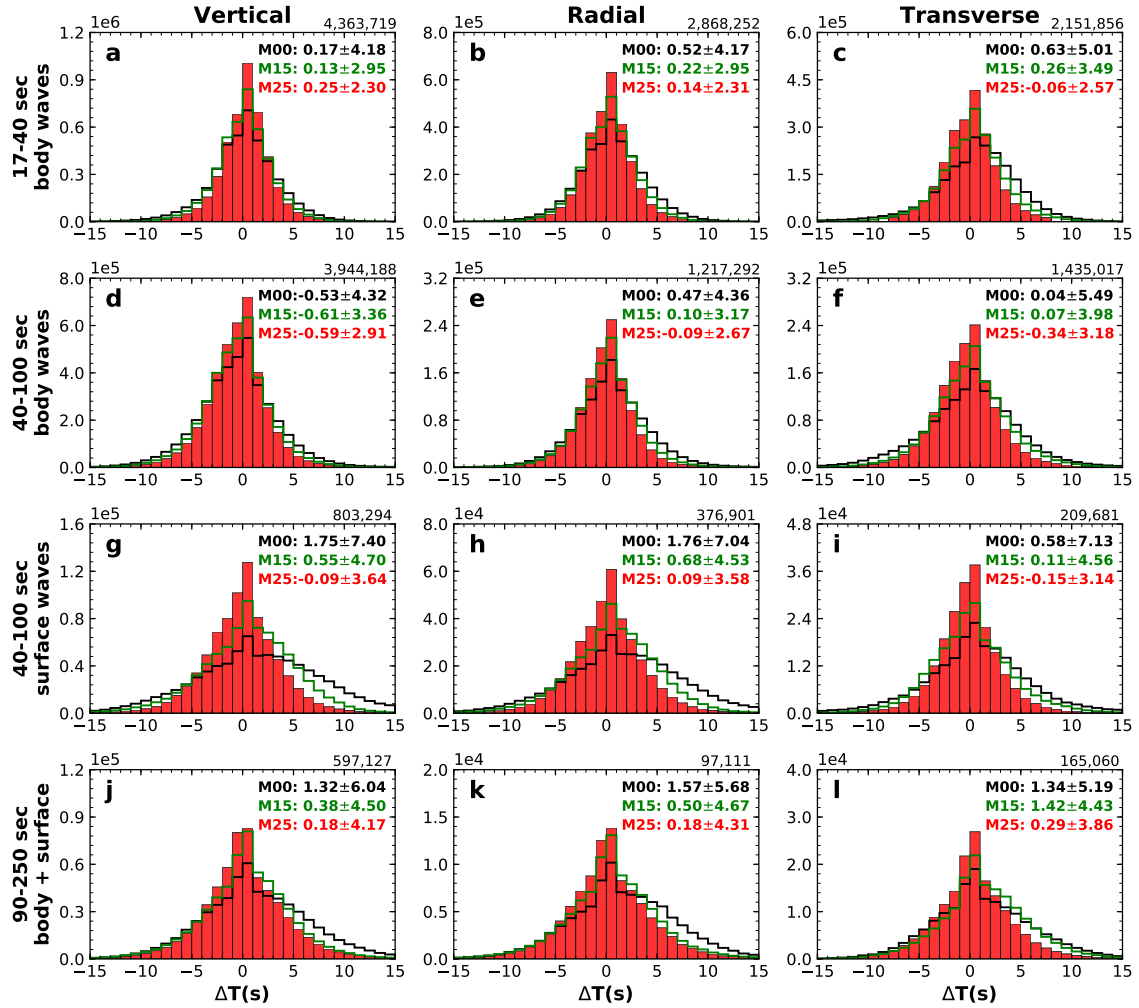


Figure 5.10: Histograms of phase measurements in all twelve measurement categories for S362ANI combined with CRUST2.0 (M00, Black), GLAD-M15 (M15, Green), and GLAD-M25 (M25, Red). Each column represents one component and each row corresponds to a period band. The numbers above the top right of each panel denote the number of measurements in the corresponding category. The total number of measurements is 18.2 million. The mean and standard deviations of the phase measurements for the three models are displayed in the top right corner of each panel.

are steadily reduced. Again we note that the inversion is aimed at reducing the overall misfit, so there are small tradeoffs between different measurement categories.

Fig. 5.11 shows histograms of 17–40 s P-wave traveltimes anomalies on the vertical and radial components, and 17–40 s S-wave traveltimes anomalies on the transverse component. Both P and S waves exhibit consistent reductions in terms of both mean and variance.

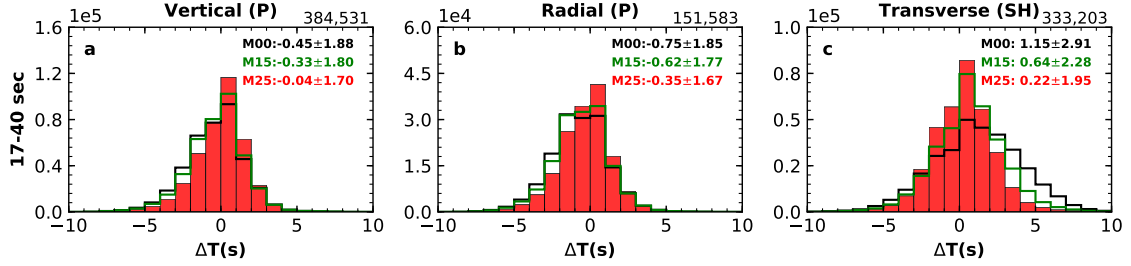


Figure 5.11: Histograms of 17–40 s traveltime anomalies of P (vertical and radial), and SH (Transverse) arrivals for models S362ANI combined with CRUST2.0 (M00, Black), GLAD-M15 (M15, Green), and GLAD-M25 (M25, Red).

Fig. 5.12 shows histograms of the amplitude measurements for all twelve measurement categories, which were not used in the current inversion. Despite this, we observe modest reductions in all standard deviations of the histograms. The histograms are nicely centered, indicating that the moment magnitudes are suitably selected, because the scalar moment affects all measurement categories equally. In the next phase of our ongoing inversion we plan to begin assimilating amplitude measurements while simultaneously adding shear attenuation as a new model parameter.

5.10 Model evaluation

5.10.1 Point-spread function analysis

Checkboard tests or tests involving a chosen known structure, e.g., a plume or slab, are frequently used to evaluate resolution in a tomographic inversion. Such tests are extremely expensive in FWI and adjoint tomography, because they require roughly the same computational resources as the actual inversion. In lieu of such tests, we previously performed two point-spread function (PSF) analyses for model GLAD-M15 [12]. Since GLAD-M25 — like its predecessor GLAD-M15 — uses waves with a shortest period of 17 s but an earthquake database that is six times larger, we can expect improved versions of these already successful PSF tests. In the interest of

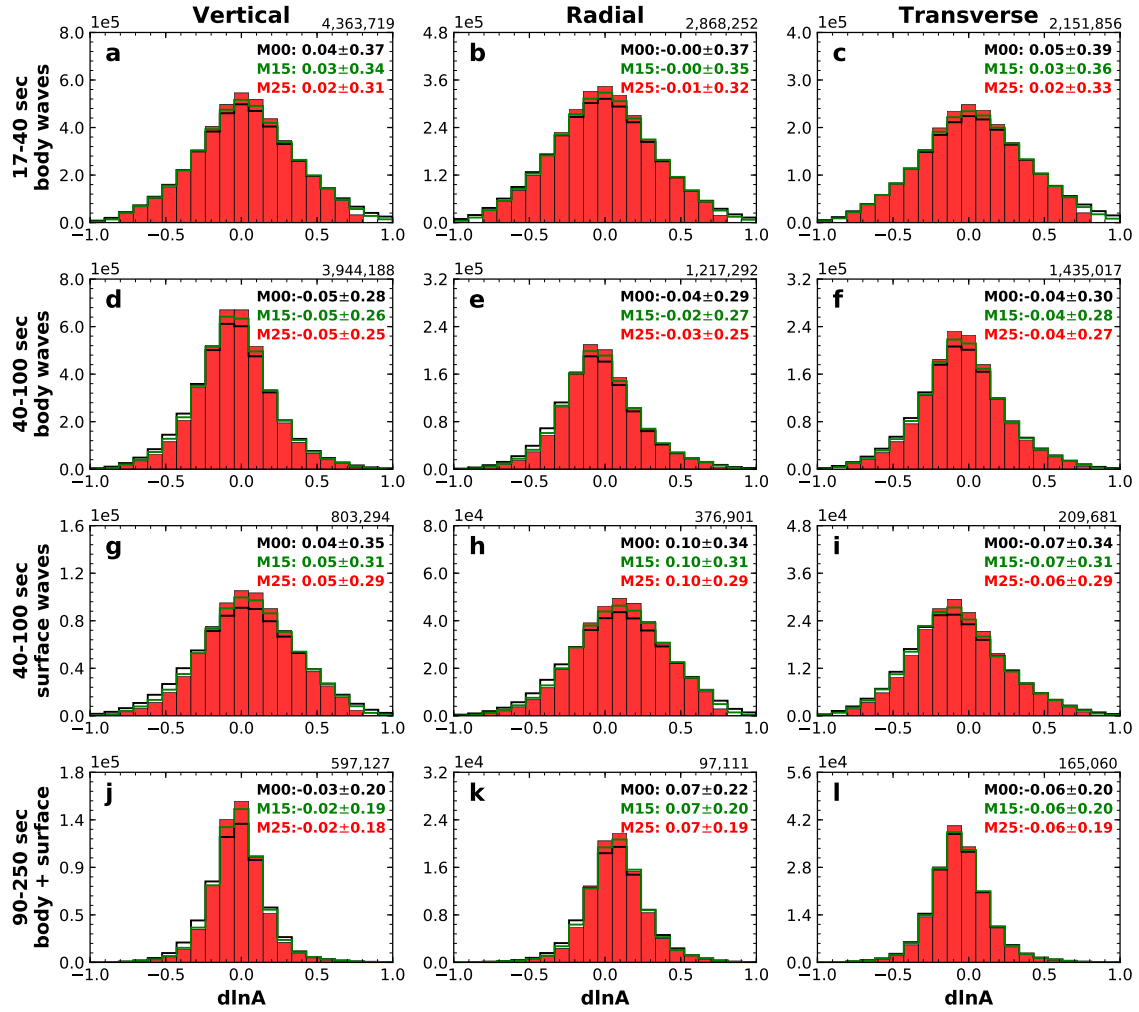


Figure 5.12: Same as Fig. 5.10 except for amplitude measurements. These measurements are currently not used in the inversion.

focusing our efforts on obtaining the new model, we chose to direct our limited OLCF INCITE allocation towards the actual inversion rather than improved PSF tests.

5.10.2 Held-out data set

Following the approach of [121], [20], and [12], we selected 360 earthquakes that were not used in the actual inversion. This held-out data set consists of all magnitude 6.3–7.0 earthquakes in the global CMT catalog that were not used in the inversion. We chose larger events to generate as many measurements as possible. We calibrated the

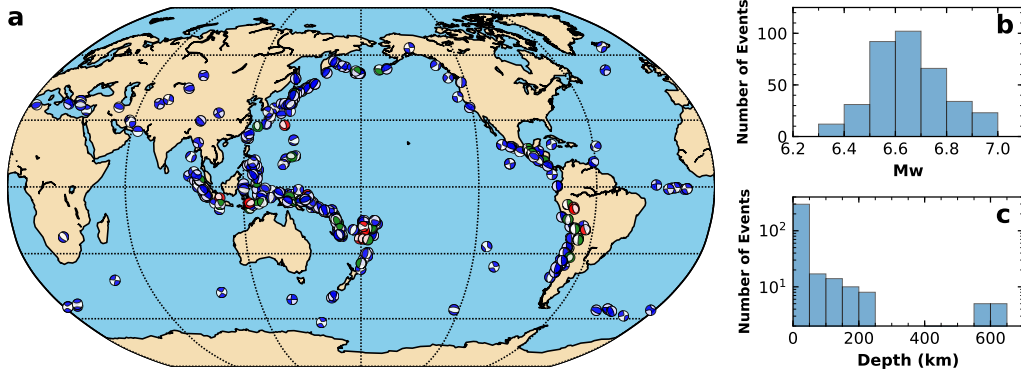


Figure 5.13: Summary of the held-out database containing 360 earthquakes. These events were not used in the structural inversion. (a) Distribution of events color coded by depth range as in Fig. 5.2. (b) & (c) Histograms of moment magnitude and depth.

	Vertical (%)	Radial (%)	Transverse (%)
17–40 s	11.8 (29.2)	14.1 (33.7)	21.5 (43.4)
40–100 s body waves	14.5 (26.2)	12.9 (32.2)	16.9 (39.0)
40–100 s surface waves	29.3 (49.1)	28.1 (49.4)	23.7 (51.2)
90–250 s	10.9 (30.9)	14.3 (34.8)	24.0 (34.9)

Table 5.2: Changes in fit for 360 earthquakes not used in the inversion in the twelve measurement categories between the new model, GLAD-M25, and its starting model, GLAD-M15, and, in parentheses, between GLAD-M25 and model S362ANI combined with CRUST2.0, which was the starting model for the GLAD-M15 inversion.

centroid time and scalar moment using a grid search based on 3D synthetics calculated in GLAD-M25. Fig. 5.13 summarizes the properties of the held-out database.

First, we repeated the misfit assessment discussed in Section 5.9.4 for the held-out database. Table 5.2 summarizes the reductions in misfit for the held-out database for model GLAD-M25 compared to GLAD-M15 as well a S362ANI combined with CRUST2.0. It is a validation of our approach to see that the reductions are comparable to the values tabulated in Table 5.1 for the actual inversion. Overall, the reductions are slightly smaller, partly due to the fact that we did not conduct full CMT inversions for the held-out database.

Second, we repeated the histogram comparisons discussed in Section 5.9.5 for the held-out database. We used a set of identical windows on all three components to assess phase anomalies in models GLAD-M25, GLAD-M15, and S362ANI combined

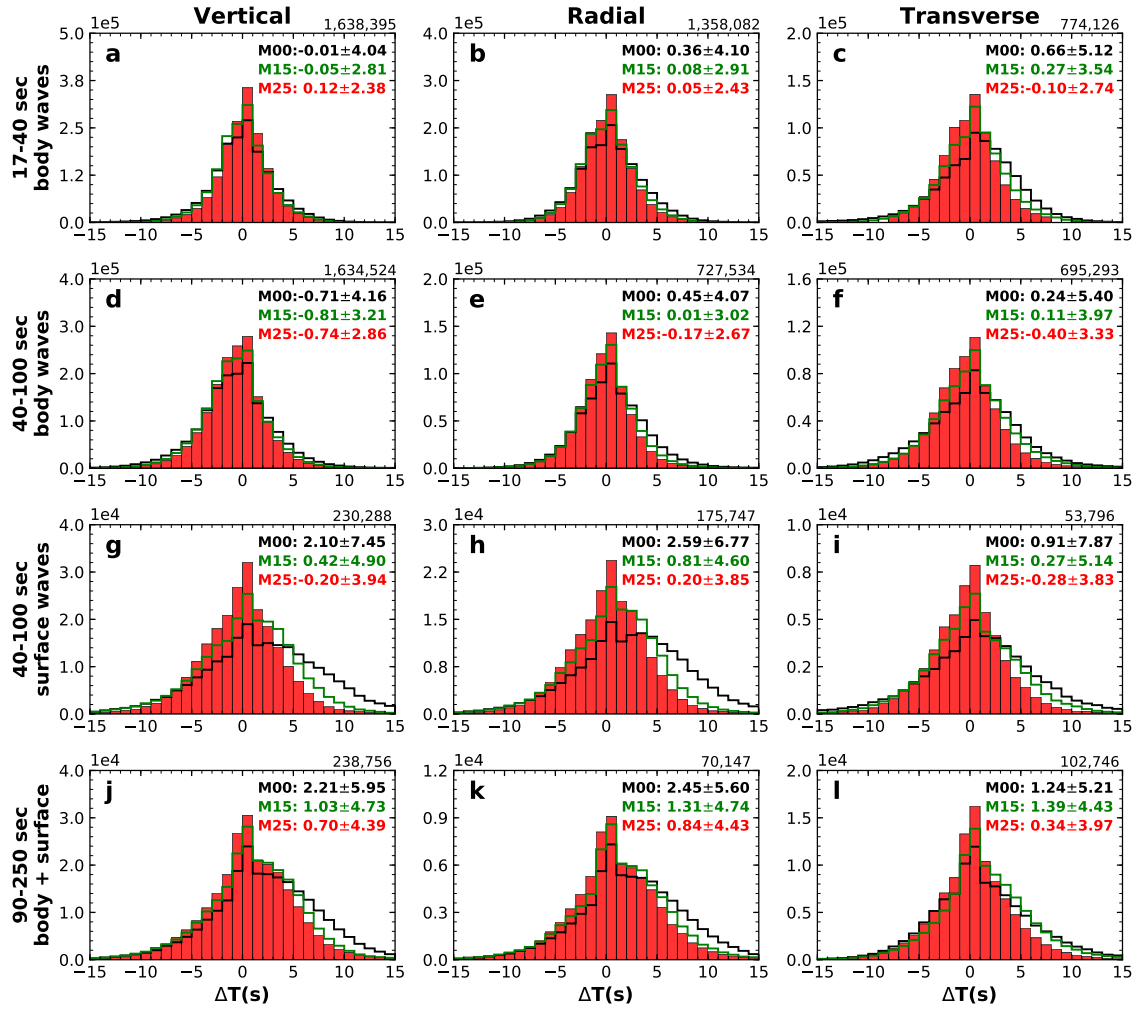


Figure 5.14: Same as Fig. 5.10, except for the held-out database.

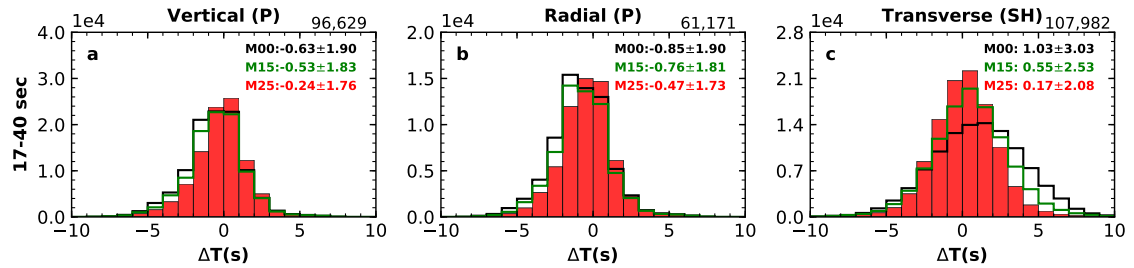


Figure 5.15: Same as Fig. 5.11, except for the held-out database.

with CRUST2.0. Fig. 5.14 shows histograms of the resulting phase measurements in all twelve measurement categories. The total number of measurements exceeds 7.8 million. As in the actual inversion, we observe systematic decreases in all standard deviations in all twelve categories, and we note a sharpening of the distributions centered around zero.

Finally, direct P and S traveltimes anomaly measurements were extracted and compared for three models in Fig. 5.15. Again the histograms are consistent with the actual inversion, as expected.

5.11 Model GLAD-M25

In this section we discuss model GLAD-M25 in some detail. We begin with a global overview of the model, before concentrating on specific geographical regions. We conclude by highlighting various slabs and plumes. The focus is on isotropic shear and compressional wavespeed variations. We provide comparisons with numerous other global and regional tomographic models, but we refrain from detailed tectonic/geodynamic interpretations, which will be the subject of more targeted future investigations. Our goal in the article is to discuss the construction of model GLAD-M25, and to place it into a broader tomographic context.

Vertical cross sections are plotted relative to the spherical average of GLAD-M25, as discussed in Appendix A. For plotting purposes and use in other applications, an expansion of the model in spherical harmonics and radial B-splines is discussed in Appendix B.

5.11.1 Global structure

We first examine model GLAD-M25 in the context of existing global tomographic models. In Fig. 5.16 we compare global maps of the isotropic part of our shear

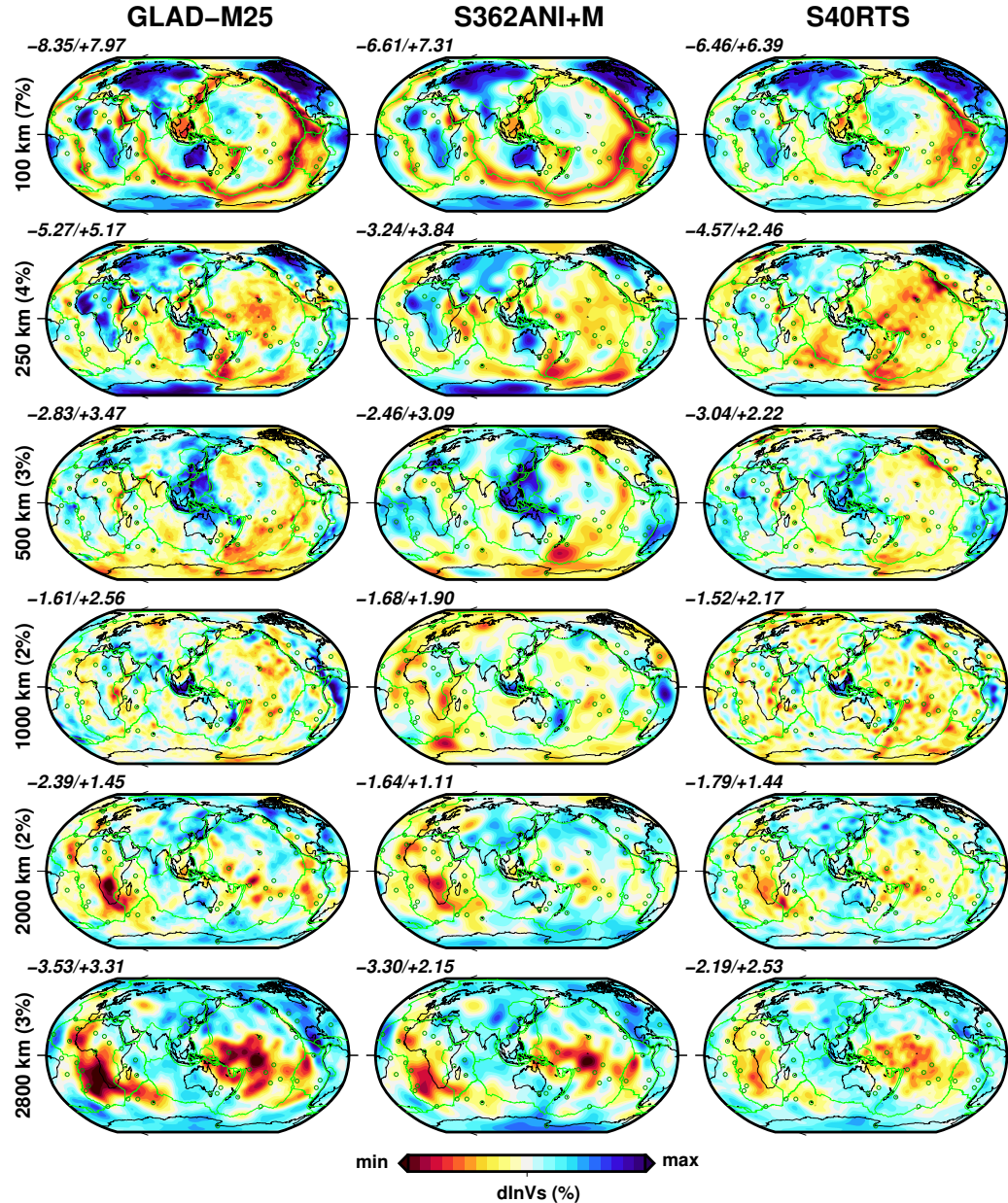


Figure 5.16: Map views of global shear wavespeed perturbations at various depths for model GLAD-M25 (left column), S362ANI+M(middle column) [91], and S40RTS(right column) [108]. At a given radius, perturbations are calculated relative to each model's average. The range of perturbations in shear wavespeed varies from map to map, as indicated in the top left of each panel. The green circles denote locations of various hotspots [90]. The range of the colorbar is the same for each row, and its maximum value is indicated in parentheses on the left, after the depth.

wavespeed model with model S362ANI+M [91], which is an updated version of the starting model for the GLAD-M15 inversion, and model S40RTS [108]. Overall, these models are in good agreement at the longest wavelengths, especially GLAD-M25 and S362ANI+M. The perturbations in GLAD-M25 tend to be larger than in the other models, consistent with observations by [39], whose model is also based on a form of waveform inversion.

An important aspect of our inversion is that it constrains shear and compressional waves simultaneously. In Fig. 5.16 we compare global maps of our compressional wavespeed model with global P models LLNL-G3Dv3 [119] and GAP-P4 [41]. At a depth of 100 km, GLAD-M25 shows prominent mid-oceanic ridges, cooling of the Pacific lithosphere, and the roots of numerous continental cratons. In the upper mantle, LLNL-G3Dv3 exhibits the largest lateral variations, e.g., very slow compressional wavespeeds at 500 km depth below Hawaii, Samoa, and Tahiti. In the midmantle we can see remnants of subduction beneath South America, Indonesia, and Tonga-Kermadec. In the deep mantle, LLNL-G3Dv3 and GAP-P4 begin to fade out, but the long-wavelength patterns, in particular the lowerparts of the Africa and Pacific superplumes, are very similar.

North America

The deployment of USArray has dramatically increased data coverage across the continental United States, and yet despite this tremendous increase in data coverage, there is not as much overlap between different models as one might anticipate. In this section, we compare GLAD-M25 in this region with two global models, S362ANI+M and S40RTS, and two regional models, US22 [155] and SL2013NA [113]. US22 is a radially anisotropic model based on adjoint tomography using USArray data from 180 regional earthquakes using 15–50 s body waves and 25–150 s surface waves. SL2013NA

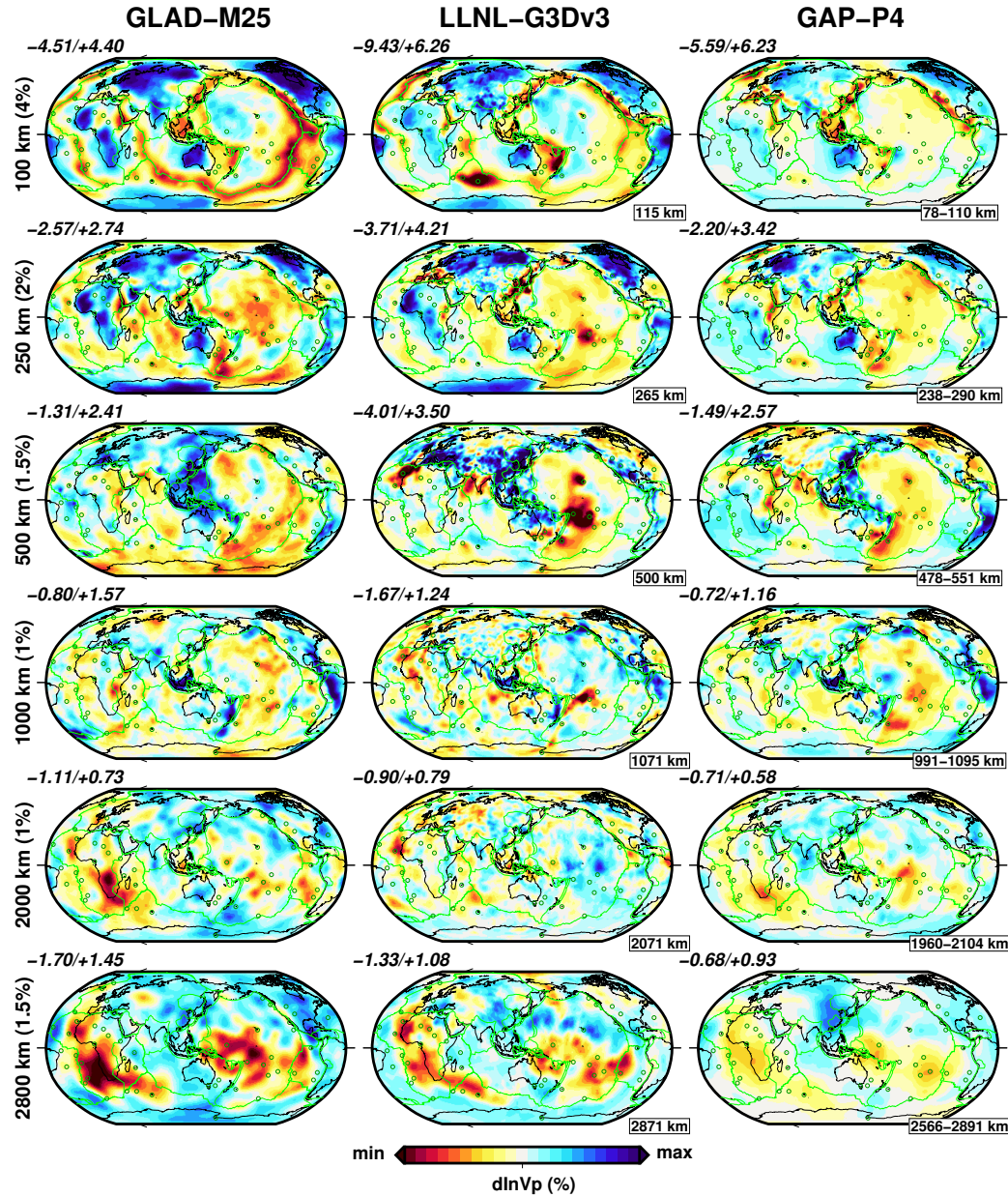


Figure 5.17: Map views of global compressional wavespeed variations at various depths for model GLAD-M25 (left column), LLNL-G3Dv3(middle column)[119], and GAP-P4(right column) [41]. For LLNL-G3Dv3, depth ranges are labeled in the bottom right bottom of each panel. Other plotting conventions are as in Fig. 5.16.

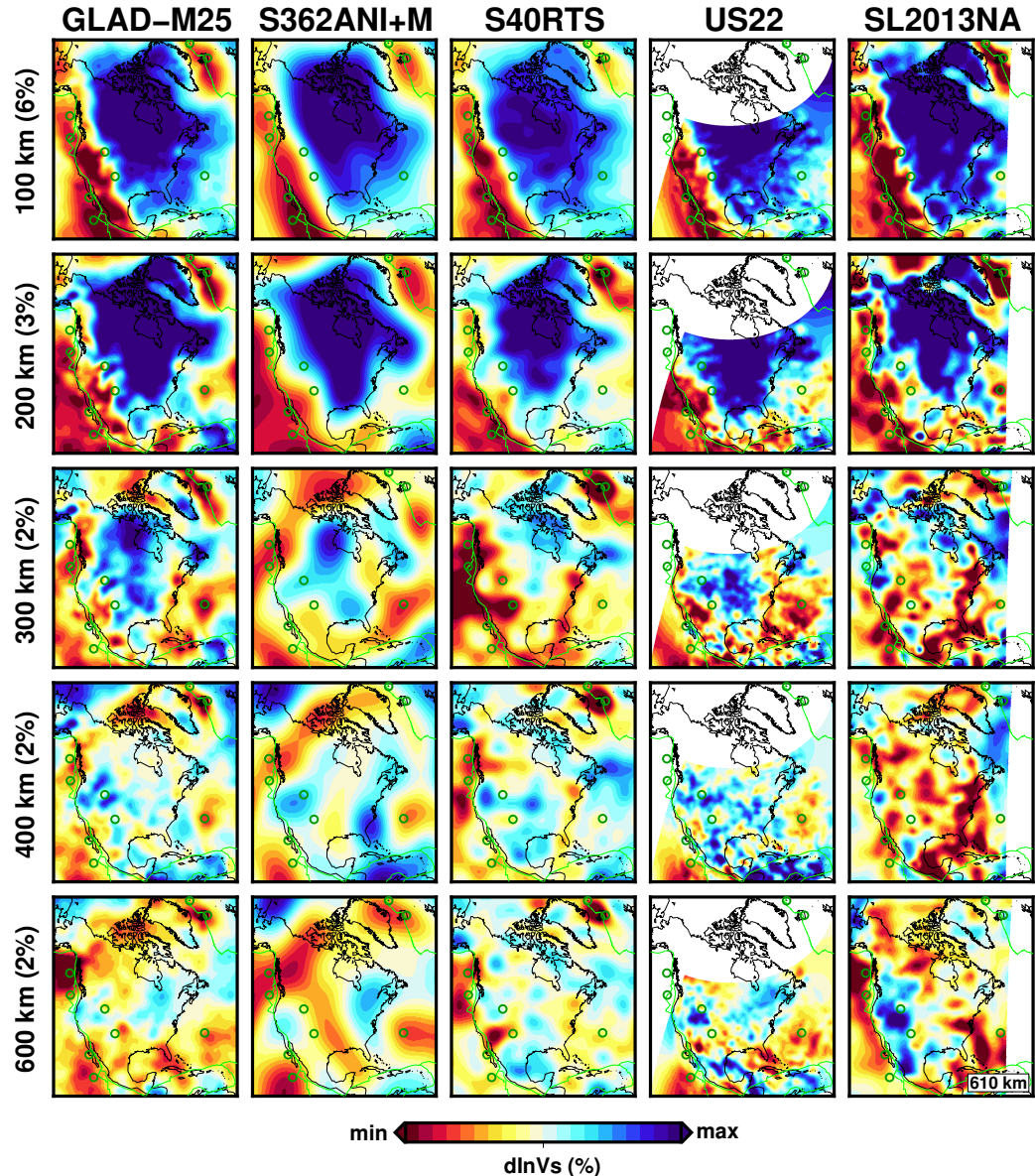


Figure 5.18: Map views of isotropic shear wavespeed variations beneath North America for model GLAD-M25 (first column) and several global (S362ANI+M and S40RTS) and regional US22 [155] and SL2013NA [113] models. Green circles denote the locations of hotspots. For SL2013NA, we show a depth of 610 km instead of 600 km, reflecting its model parametrization.

is a global upper-mantle shear wavespeed model based on multimode surface waveform tomography primarily focused on North America.

North America is characterized by a large, high-wavespeed lithospheric craton, bounded by the Rocky Mountain Front to the West and continental margin to the East [44, 142]. On both sides the lithosphere has been deformed by low wavespeed structures, thus forming sharp tectonic boundaries [81, 45, 85, 47].

At a depth of 100 km, we observe that the edges of the craton are sharper in GLAD-M25 than in the other two global models, and quite similar in shape and sharpness to the two regional models. We can clearly see impressions of the Snake River Plain (with Yellowstone) and the Raton hotspot, which also have distinct slow expressions at depths of 200 km. The core of the craton exhibits fast wavespeeds at depths reaching 300 km Northwest of Hudson Bay. In the regional models the craton has basically faded away at these depths. The Wyoming and Medicine Hat Blocks show a very strong and thick lithospheric root from shallow depths to \sim 400 km, similar to US22 but difficult to discern in SL2013NA. Similar observations can be made for the Yavapai and Mazatzal Blocks, which define the southern boundary of the large craton [113].

In the 200–400 km depth range, we observe a high wavespeed anomaly within the Gulf of Mexico, which coincides spatially with the deepest bathymetry and corresponds to a portion of ancient oceanic lithosphere [94, 113]. A remnant of the Juan de Fuca plate, with a high wavespeed footprint, is visible at depths of 300 km and 400 km, where SL2013NA shows a much stronger anomaly.

In the North, we see a high wavespeed craton beneath Greenland which is partly separated from the North American craton by low wavespeed structures beneath Baffin Bay and the Labrador Sea, where the North American craton nicely follows the coastline [17]. In the Northeast corner of the maps we see that the Iceland hotspot is very prominent in GLAD-M25 in all depth ranges, similar to S40RTS

but largely missing in S362ANI+M. In the Northwest we see a clear imprint of the Aleutian subduction zone in the 200–400 km depth range, comparable to SL2013NA but absent in the other global models.

In the East, at 100 km depth, we see ageing of the Atlantic lithosphere, comparable to the other global models [94, 113]. All models show fast anomalies beneath Newfoundland and Nova Scotia extending to depths of 300 km. The Bermuda hotspot shows a very nice slow wavespeed impression, getting sharper and stronger at depths of 200 km and 300 km (note differences in the scales of the maps). The Caribbean slab, a relatively young subduction zone, is clearly visible in our model in the 200–400 km depth range. At greater depths, GLAD-M25 shows a very distinct image of the Farallon slab, but since it goes well beyond the depth range of this comparison, we return to this feature in Section 5.11.3.

Europe

Fig. 5.19 shows isotropic shear wavespeed perturbations beneath Europe. In addition to models GLAD-M25, S362ANI+M, and S40RTS, we included regional model EU60 [154] for comparison. EU60 is the result of adjoint tomography of the crust and upper mantle beneath the European continent and the North Atlantic based on the assimilation of data from 190 earthquakes recorded by 745 seismographic stations.

A defining tectonic feature of Europe is the Trans-European Suture Zone (TESZ), also known as the Tornquist-Tesisseyre Zone, separating the Precambrian East European Craton (EEC) in the Northeast from Phanerozoic Europe in the Southwest [158]. The TESZ is very consistent across all models, even though is much sharper in GLAD-M25 and EU60.

At depths of 100—250 km we observe high wavespeeds beneath the Central Graben in the North Sea, which is clearly separated from the EEC. The tectonic history of the Mediterranean is complex, involving several regional plates and multiple past and

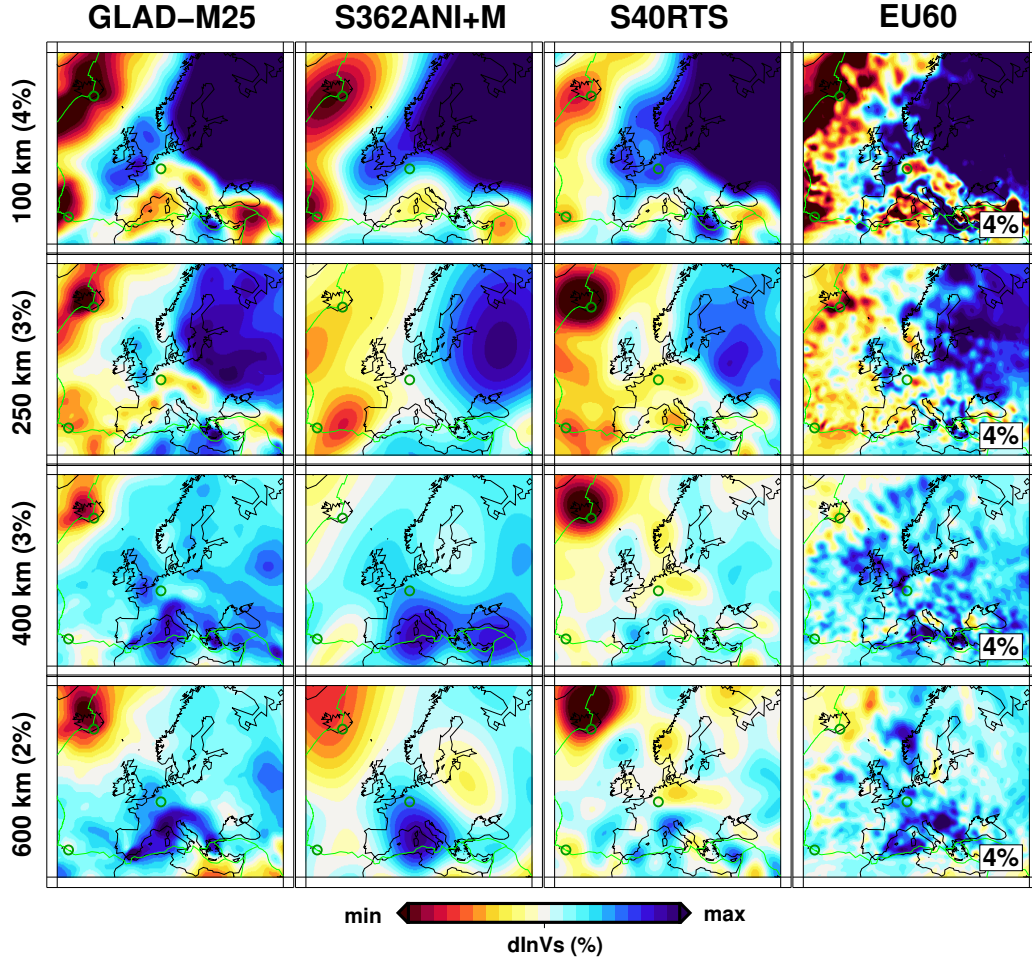


Figure 5.19: Map views of isotropic shear wavespeed variations beneath Europe for model GLAD-M25 (first column), two global model (S362ANI+M and S40RTS), and one regional model EU60 [154]. For EU60, the range of the color bar is 4% at all depths, as indicated in the bottom right bottom of the panels.

present subduction zones [28]. We see slab ponding in the transition zone beneath the western Mediterranean associated with slab roll-back of the Appennines-Maghrebides subduction zone [147, 153]. At shallower depths, we see low wavespeeds along its western border, which are interpreted as back-arc extension associated with roll-back. Compared to S362ANI+M and S40RTS, our model shows much sharper features for these tectonic structures.

In the Eastern Mediterranean, there is a distinct fast anomaly beneath the Dinarides Mountains, separating the Adria plate from the Pannonian Basin, indicating subduction of the Adria plate beneath the Eurasian plate. This anomaly gets sharper

at 600 km depth. Its southern part interacts with the Hellenic slab, which penetrates the mantle transition zone and extends below 1,000 km in our model. We discuss the Hellenic Arc further in Section 5.11.3. The Pannonian Basin is characterized by a low wavespeed anomaly at depths from 100 km to 250 km. In this depth range we also see slow wavespeeds beneath Anatolia, stronger than in the two other global models.

In Central Europe we note the Cenozoic Ridge System [157], characterized by low wavespeeds from the Massif Central to the Eifel. Both EU60 and GLAD-M25 exhibit a slow anomaly beneath the northern part of the Rhine Graben, which is interpreted as the reservoir that fuels the Eifel hotspot [42, 154].

Beneath the Atlantic Ocean, our model enhances slow anomalies beneath the ridges, especially underneath Iceland and the Azores. Compared to S362ANI+M, Iceland becomes much stronger in the upper mantle at depths from 250 km to 400 km, extending all the way to the mantle-transition zone. The Azores represent a much shallower hotspot, with a maximum depth of about 250 km.

Asia

Asia, like Europe, has a complex tectonic history, involving interactions among the Indian, Eurasian, Australian, Pacific, and Philippine plates. Map views of GLAD-M25 centered on Asia are plotted in Fig. 5.20, together with S362ANI+M, SL2013sv [112], and regional model EARA2014 [20]. EARA2014 is a transversely isotropic model based on adjoint tomography, assimilating 1.7 million frequency-dependent travel-time measurements from 227 earthquakes recorded by 1,869 seismographic stations. It has superior data coverage, mainly by incorporating data from the China Array.

The Southwestern part of China is dominated by the Himalayas, expressing the collision between India and Eurasia [65]. GLAD-M25 exhibits strong high wavespeed anomalies in this area, which extend all the way from 100 km to 600 km, narrowing and sharpening with depth, in good agreement with EARA2014. The Tibetan

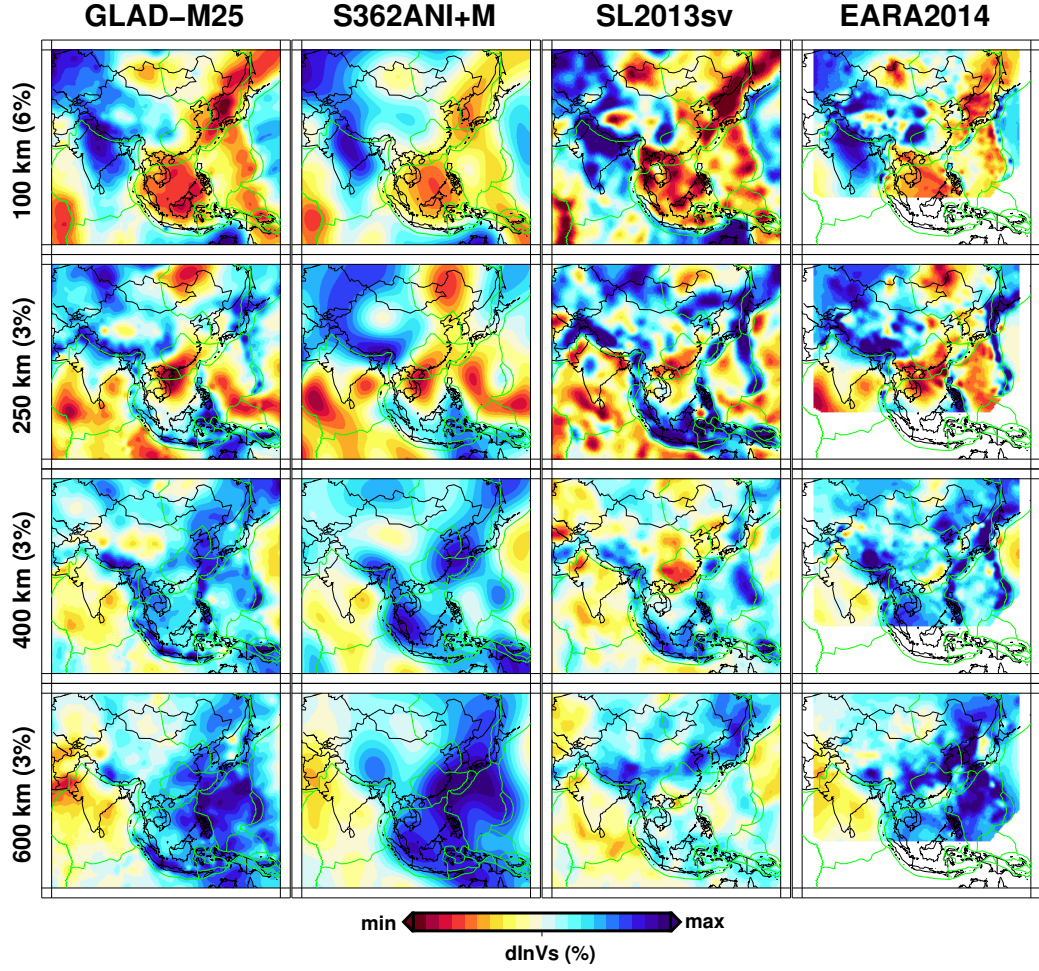


Figure 5.20: Map views of shear wavespeed variations beneath Asia for GLAD-M25 (first column), global models S362ANI+M (second column) and SL2013sv (third column), and regional model EARA2014(last column) [20].

plateau shows relatively low wavespeeds compared to its surroundings, including the Himalayas to its South and the Tianshan Mountains to its North, consistent with the other global and regional studies.

The southern part of Asia shows major tectonic activity between the Philippine, Eurasian, and Australia plates. The Sunda trench is visible as a distinct high wavespeed anomaly below 200 km, nicely following the plate boundary. This feature remains very sharp at 600 km and extends down to 1000 km. We discuss this subducting slab further in Section 5.11.3. The Manila and Philippine trenches are also much sharper in our model between 200 km and 600 km than in the other global

models, and comparable to EARA2014. The eastern edge of the map features a series of trenches following plate boundaries, including Japan, Izu-Bonin, and Mariana. These slabs are absent in the other global model, but feature more prominently in EARA2014. Along the northern edge we see low wavespeeds associated with the Altai-Sayan and Baikal rift systems. In terms of intra-plate activities, at shallow depths we see clear low wavespeed impressions of the Hainan and Changbai volcanoes, suggesting a lithospheric rather than deeper mantle origin [149]. The Sichuan basin, a very localized high-wavespeed structure, extends below 250 km depth. At 600 km, most models show a large region of high wavespeed beneath the Philippine plate, indicating ponding of ancient subducted plates.

South America

Fig. 5.21 shows compressional wavespeed anomalies in model GLAD-M25 in comparison with three global models, namely, S362ANI+M [91], LLNL-G3Dv3 [119], and GAP-P4 [41]; the latter two are V_P models.

At 150 km depth, the northern half of South America is covered by a large lithospheric craton, exhibiting fast anomalies in all models except GAP-P4. The Galapagos, San Felix, and Juan Fernandez hotspots are associated with distinct low wavespeed anomalies in GLAD-M25, but not in the other models. At 300 km depth, we see sharpened subduction of the Nazca plate in GLAD-M25 compared to S362ANI+M, similar in shape to model LLNL-G3Dv3. Moving to greater depths, we see distinct Peru and Chile slabs in GLAD-M25, with the Chile slab ponding in the transition zone and the Peru slab penetrating into the lower mantle and still clearly visible at 1000km depth. These differences in behavior are consistent with GAP-P4 [41].

In the south, Scotia Arc subduction is very distinct in GLAD-M25 at all depths, but barely observable in other models. This is probably a consequence of coverage

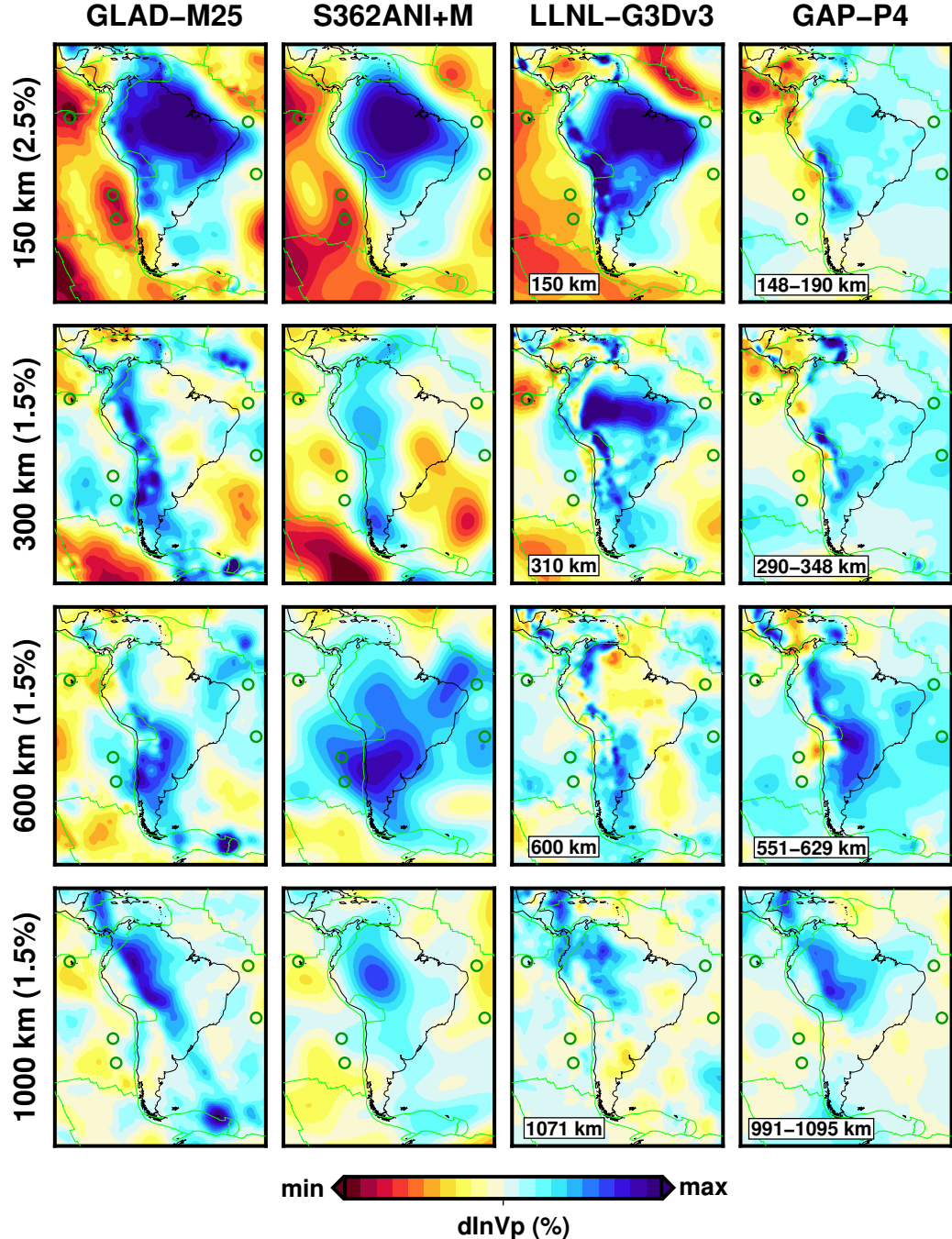


Figure 5.21: Map views of compressional wavespeed variations beneath South America for GLAD-M25 (first column) and global models S362ANI+M [91] (second column), LLNL-G3Dv3 [119] (third column), and GAP-P4 [41] (fourth column).

provided by events in the region (see Fig. 5.2). To the north, Caribbean subduction is clearly discernible in model GLAD-M25 and the two V_p models.

5.11.2 Plumes

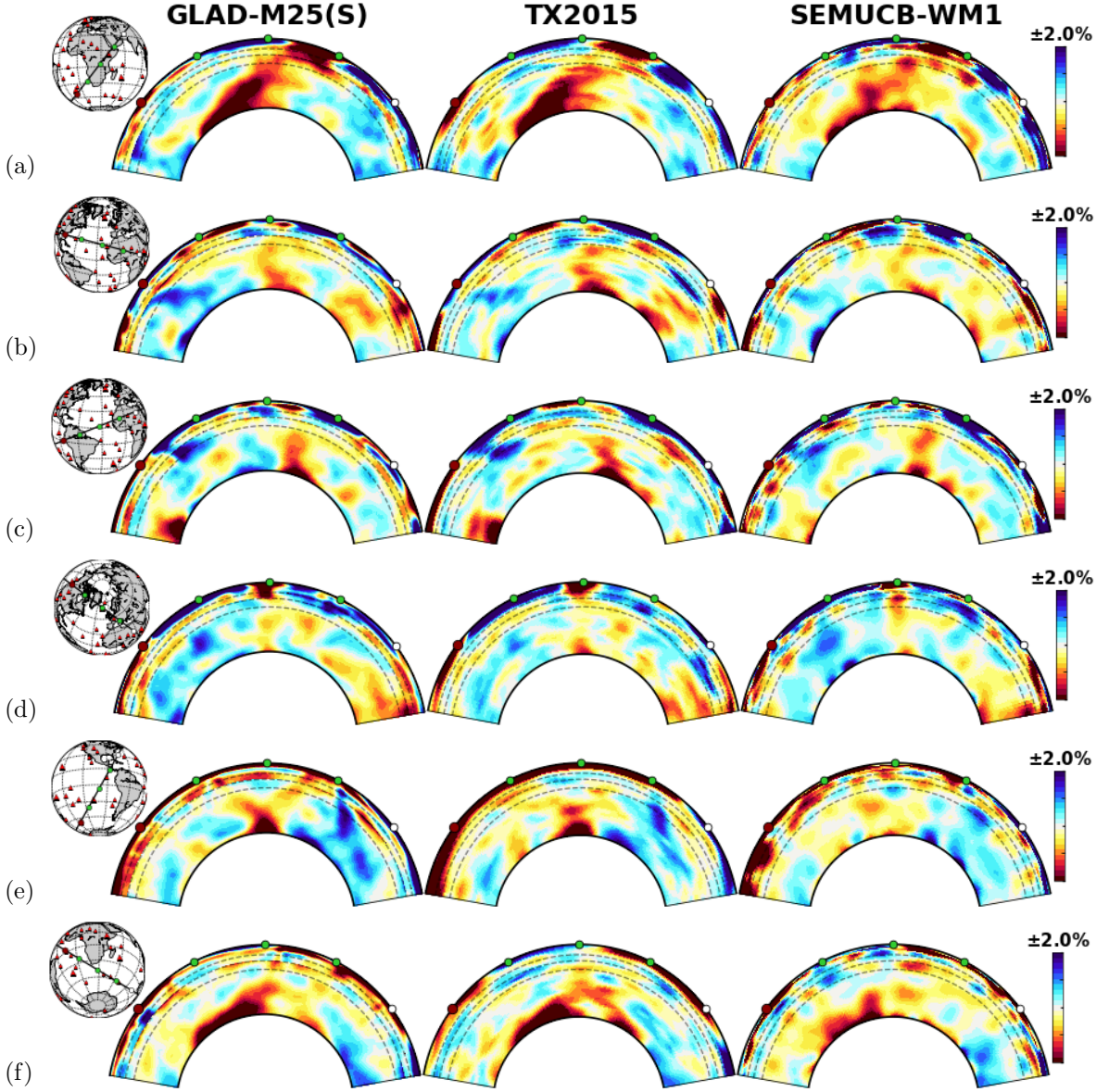


Figure 5.22: Vertical cross sections for various plumes for models GLAD-M25 (V_S ; left column), TX2015 [74] (center column), and SEMUCB-WM1 [38] (right column). The map in the top left corner of each row shows the cross section with color-coded red, green, and white dots for geographical reference; hotspots are denoted by red triangles. The dashed black semicircles in the cross sections denote depths of 410 km, 660 km, and 1000 km. (a) Afar; (b) Bermuda (left) and Canary (middle); (c) Cape Verde (middle) and Hoggar (right); (d) Iceland (middle) and Eifel (right); (e) Easter (left) and Galapagos (right); (f) Marion (middle), and Kerguelen (right).

In this section we highlight various plume systems on Earth. Fig. 5.22 shows cross sections of several plumes, comparing models GLAD-M25 (V_P), TX2015 [74],

and SEMUCB-WM1 [38]. All three models have common plume features, and GLAD-M25 and TX2015 are in overall good agreement.

The three models tend to agree near the CMB, and there is overall good agreement between GLAD-M25 and TX2015, but the models can differ substantially in the mid and upper mantle, with profoundly different implications for mantle convection.

Afar In Fig. 5.22(a), we see that the Afar plume in model GLAD-M25 originates from the CMB, narrows its diameter in the mid mantle, and broadens again above the 660 km discontinuity. It exhibits very similar behavior in TX2015 but differs significantly in SEMUCB-WM1.

Bermuda and Canary In Fig. 5.22(b), from left to right, we see in model GLAD-M25 (i) the Farallon slab; (ii) the Bermuda hotspot above the 660 km discontinuity; (iii) the Canary hotspot originating from the CMT and rising all the way up the Earth's surface; (iv) the Afar hotspot from another angle.

Cape Verde and Hoggar Fig. 5.22(c) features (i) South America subduction; (ii) the Cape Verde hotspot extending from the CMB all the way to the surface; (iii) the Hoggar hotspot from 660 km to the surface.

Iceland and Eifel Fig. 5.22(d) shows a plume which rises from the CMB right below Iceland, reaches 660 km, amplifies, and ascends to the surface. The intensification above 660 km may be an indication of partial melting.

Easter and Galapagos Fig. 5.22(e) contains (i) the Easter hotspot; (ii) the Galapagos hotspot; (iii) the Central America slab. In models GLAD-M25 and TX2015, the Easter and Galapagos hotspots appear to originate from the same underlying plume in the deep mantle, which is the eastern arm of the Pacific superplume.

Marion and Kerguelen Finally, in Fig. 5.22(f) we see the Marion and Kerguelen hotspots, which might be connected to Afar in the lower mantle. Recovering these plumes is challenging due to poor data coverage in the southern hemisphere.

5.11.3 Subduction zones

In this section we highlight various subduction systems on Earth. In Fig. 5.23 we compare GLAD-M25 (V_P) with two compressional wavespeed models, namely, GAP-P4 [41] and UU-P07 [139]. Fig. 5.23(a) features the Aegean subduction zone. All models show a slab penetrating into the lower mantle beyond a depth of 1,000 km. Fig. 5.23(b) shows the South American slab, which, in this cross section, ponds in the shallow lower mantle in all three models, before sinking all the way to the CMB. Figs. 5.23(c) and (d) show cuts across the ancient Farallon slab, which penetrates deeply into the lower mantle, as spectacularly documented by, for instance, grand1994,hilst1997,grand1997high. At depths greater than 1,000 km, we see a very strong expression of the slab in model GLAD-M25, which is much weaker in the two P models. The difference may be attributed to increased data coverage thanks to USArray, as well as the use of finite-frequency Fréchet derivatives. Fig. 5.23(e) shows subduction beneath the Himalayas. All three models show two distinct fast anomalies below 660 km, one above 1,000 km and the other, further to the southwest, below 1,000 km. Finally, Fig. 5.23(f) shows subduction beneath the Java portion of the Sunda Arc. At this location the slab pernetrates into the lower mantle, at which point its spreads out laterally, in agreement with models GAP-P4 and UU-P07. [40] explained this flattening using a model of [107], suggesting that the subducted slab thickened and buckled to form a dense megalith above the 660 km discontinuity before sinking into the lower mantle.

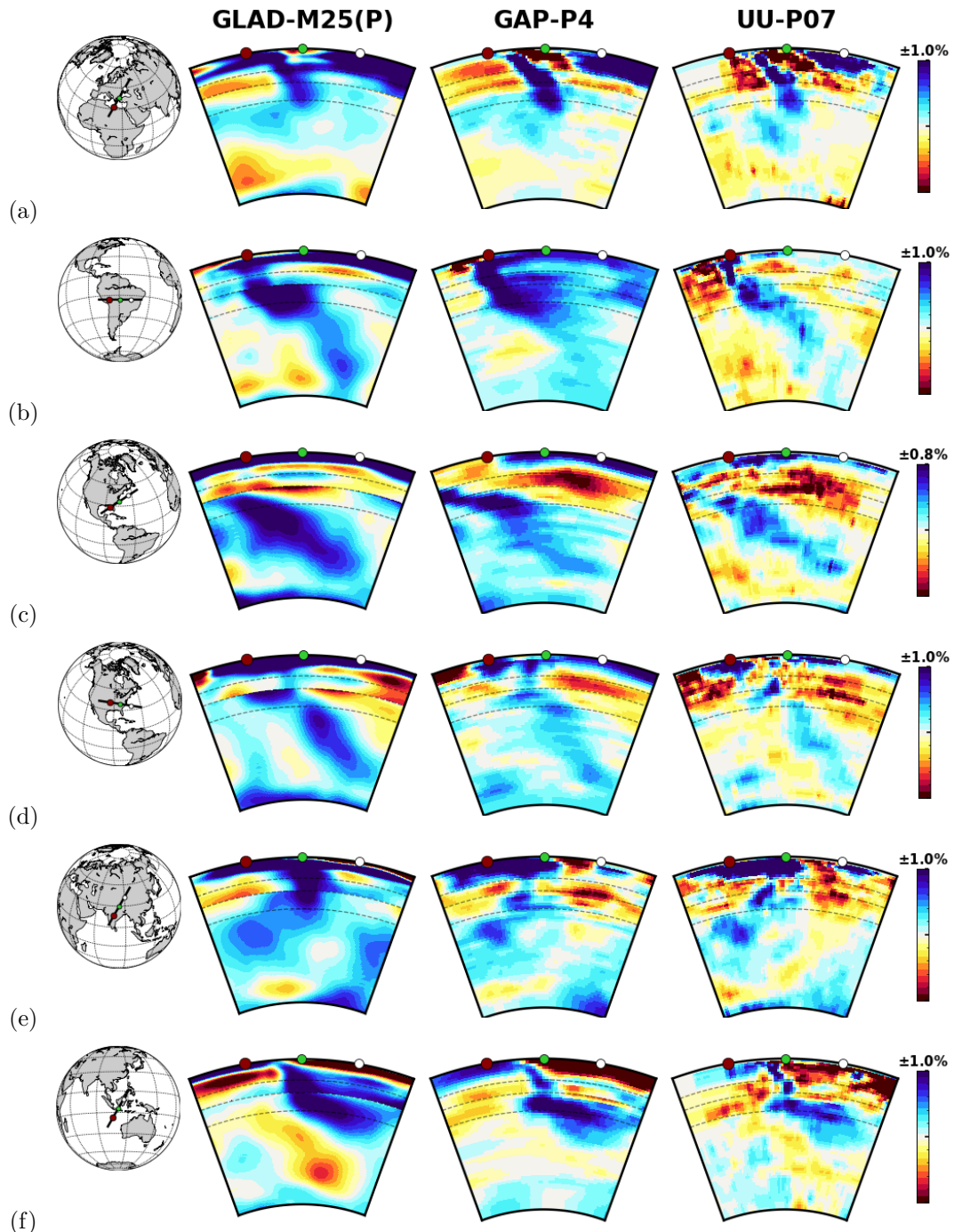


Figure 5.23: Vertical cross sections of compressional wavespeed perturbations in various subduction zones for models GLAD-M25 (V_p ; left column), GAP-P4 [41] (middle column) and UU-P07 [139] (right column). The map in the top left corner of each row shows the cross section with color-coded red, green, and white dots for geographical reference. The dashed black semicircles in the cross sections denote depths of 410 km, 660 km, and 1000 km. (a) Aegean; (b) South America; (c) Hatteras; (d) Wichita. (e) Nepal; (f) Sunda.

Overall, the three models are in reasonably good agreement. At shallow depths, model GLAD-M25 shows more distinct continental crust and cratons, thanks to the inclusion of surface waves. But in the upper and mid mantle, the models share very similar attributes.

5.12 Discussion

Seismology is a science driven by data. There was a time when global seismologists would meticulously inspect single seismograms to glean valuable information from them. Today, we have easy access to data from thousands of earthquakes recorded by tens of thousands of seismographic stations, and individual inspection of all of these records has become impossible. Still, it would be a shame not to utilize as much as possible of the information in this massive seismographic database.

To facilitate fast and effective access to such vast data resources, we use ASDF [61] in the preprocessing stage of the adjoint tomography workflow, and to accommodate massive I/O during the postprocessing stage we use the ADIOS library [70]. For data assimilation, tools such as FLEXWIN, which automatically select data windows suitable for measurements, are indispensable, and we see tremendous opportunities for the use of machine learning algorithms in this context [21]. Without these libraries and tools, the construction of model GLAD-M25 would have been impossible.

Some form of automated parallel workflow management is critical for the global adjoint tomography process, because classical inversion workflows suffer from I/O inefficiencies, lack of fault tolerance, and an inability to work in distributed resource environments [66]. The EnTK workflow management engine [4] largely overcomes these limitations by facilitating tracking of tasks and job failure detection, thereby enabling semi-automatic job resubmission if necessary. These are the attributes re-

quired for bringing global FWI to its full potential, enabling the assimilation of data from thousands of earthquakes on the largest HPC systems.

It should be clear from this discussion that modern seismic tomography requires close collaborations with computational scientists, HPC specialists, and visualization experts, as reflected in the list of authors for this article, in addition to access to the most advanced computational platforms, such as those offered through the DOE INCITE and NSF XSEDE programs.

Although Figs. 5.6–5.8 illustrate that much information in seismograms is being assimilated, we still have a long way to go before explaining every wiggle in hundreds-of-minutes-long seismograms. Currently, we are only fitting the phase in selected time windows, and amplitude information remains completely unused. We accommodate the full physics of seismic wave propagation, but we are not exploiting the most general earth model parameterization. GLAD-M25 is an elastic model with radial anisotropy confined to the upper mantle. It is well known that the upper mantle is azimuthally anisotropic [88, 89], and we also know that amplitude information helps constrain second derivatives in phase speed [146, 132, 133], in addition to lateral variations in attenuation [110, 104, 25]. Thus, the natural next step in global FWI is to use phase and amplitude information simultaneously to jointly constrain the elastic and anelastic structure of the Earth. To accomplish this next step, source parameters need to be constrained more carefully, especially as we push the resolution to shorter periods [138].

The global distribution of earthquakes (Fig. 5.2) and stations (Fig. 5.3) is highly uneven. This problem may be alleviated to some extent by using suitably chosen misfit functions with appropriate geographical weighting of sources and receivers [69, 111]. The ultimate solution may be a dense network of Ocean Bottom Seismometers, but meanwhile an armada of floating seismometers may offer a cheaper and more practical alternative [98].

5.13 Conclusion

Building on our experiences during the construction of our first-generation global adjoint tomography model GLAD-M15 [12], for this study we expanded our earthquake database from 253 to 1,480 events, which were collectively recorded by more than 11,000 seismographic stations. We used three-component seismograms in four period bands, namely 17–40 s body waves, 40–100 s body waves, 40–100 s surface waves, and 90–250 s surface waves, resulting in twelve measurement categories. This culminated in the assimilation of more than 18 million time windows.

GLAD-M25 — like its predecessor GLAD-M15 — invokes no crustal corrections, and constrains crust and mantle shear and compressional wavespeeds simultaneously. Such ubiquitous crustal corrections may affect inferences about upper-mantle anisotropy [13, 100, 33], and are likely the main reason for significant differences between radially anisotropic upper-mantle models [18]. Treating the crust and mantle equally and simultaneously is one of the main strengths of GLAD-M25, accepting the additional computational costs, but thereby avoiding any approximations or corrections. Another strength is the fact that the effects of attenuation are fully accommodated, both in forward and in adjoint simulations. These points highlight the importance of taking the full physics of seismic wave propagation properly into account in seismic imaging.

Another very important attribute of GLAD-M25 is that it constrains shear and compressional wavespeeds simultaneously in the same period range, thereby enabling us to interpret the two wavespeeds together. As illustrated in Figs. 5.6 and 5.7, numerous compressional wave arrivals are assimilated, including P, PP, PPP, PKP, PS, and PPS. In future work we will capitalize on this by using the V_P/V_S ratio to help constrain thermo-chemical and geodynamical processes in the mantle.

GLAD-M25 was quantitatively evaluated in several ways. First, it produces significant misfit reductions in all twelve measurements categories. Second, it produces

nicely-centered Gaussian traveltimes & amplitude anomaly histograms in all measurement categories. Finally, for a held-out data set of 360 events we see similar misfit reductions and traveltimes & amplitude anomaly histograms as in the actual inversion.

When we compare GLAD-M25 with other global models, we find overall good agreement at longer wavelengths. In particular, GLAD-M25 and TX2015 feature very similar plume structures. Unlike other global models, when we compare GLAD-M25 with regional models we also observe generally good agreement at smaller wavelengths, and, in particular, plumes and subduction zones feature prominently. However, it is important to note that GLAD-M25 tends to agree well with regional models based on the same S362ANI + Crust2.0 starting model, numerical wave propagation solver, and quasi-Newton inversion technique (e.g., EU60, US22, and EARA2014). It is also important to point out that even in regions with dense seismographic coverage, such as North America, recent models can differ substantially, especially at greater depths. Nevertheless, our global inversion is bridging the gap between global and regional studies, approaching regional-scale resolution in areas with sufficient data coverage. We can observe this increase in resolution in GLAD-M25 in the normalized power per spherical harmonic degree as a function of radius, which is displayed in Fig. 5.24.

Obvious future directions of research include growing the earthquake database further to the roughly 6,000 earthquakes in the right magnitude range already available via the Global CMT database, and reducing the shortest simulation period further from 17 s to 8.5 s. The most recent machine at OLCF, called “Summit”, uses IBM Power9 CPUs accelerated by NVIDIA Tesla V100 GPU and can readily accommodate such simulations.

Other future directions of research involve inversions for azimuthal anisotropy and attenuation. The feasibility of such inversions on a regional scale has already been demonstrated in studies focused on Europe by [152] and [151].

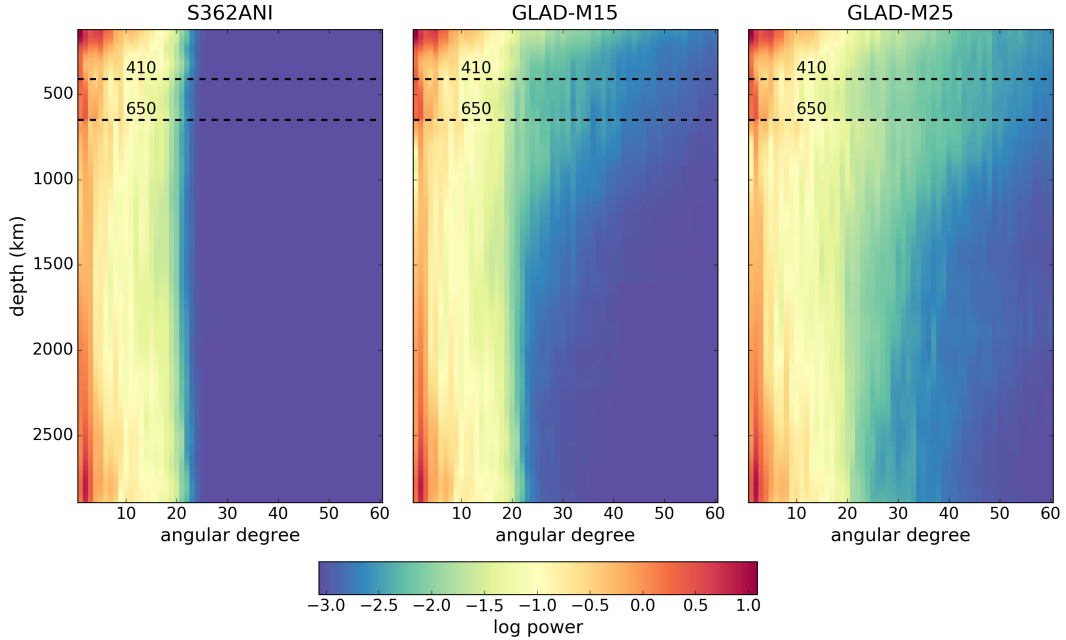


Figure 5.24: Normalized power per degree ℓ as a function of radius, based on Eqn. (B.17), for models S362ANI (left), GLAD-M15 (middle), and GLAD-M25 (right). Shown are depths greater than 120 km. (Courtesy of Caio Ciardelli.)

This research used resources of the Oak Ridge Leadership Computing Facility, which is a DOE Office of Science User Facility supported under contract DE-AC05-00OR22725. Additional computational resources were provided by the Princeton Institute for Computational Science & Engineering (PICSciE). We acknowledge IRIS (iris.edu) and ORFEUS (orfeus-eu.org) for providing the data used in this study. We thank Ryan Modrak, Ridvan Örsvuran, Frederik J. Simons, and James Smith for fruitful discussions, and Caio Ciardelli for implementing the spherical harmonic model expansion. The open source spectral-element software package SPECFEM3D_GLOBE and the seismic measurement software package FLEXWIN used for this article are freely available via the Computational Infrastructure for Geodynamics (CIG; geodynamics.org). This research was supported by NSF grant 1644826.

Appendix A

Spherically symmetric average model

In this appendix we determine the spherically symmetric (radial) average of model GLAD-M25. To accomplish this, we first need to transform the 3D spectral-element mesh — which includes ellipticity, topography/bathymetry and undulations on internal boundaries — into a spherical volume. After these adjustments, we obtain a spectral-element mesh for a perfect cubed sphere [55].

In the spherical mesh, the model may be expressed in the form

$$m(\mathbf{x}) = \sum_{\text{elem}} \sum_{\alpha, \beta, \gamma} m^{\alpha\beta\gamma} h_\alpha(\xi) h_\beta(\eta) h_\gamma(\zeta) , \quad (\text{A.1})$$

where h_α denotes a Lagrange polynomial, and where we have used the invertible mapping

$$\mathbf{x} = \mathbf{x}(\xi, \eta, \zeta) \quad (\text{A.2})$$

between spatial points $\mathbf{x} = \{x, y, z\}$ and Gauss-Lobatto-Legendre (GLL) points in the reference element $\{\xi, \eta, \zeta\}$ [54].

The spherically symmetric part of the model is defined as

$$\overline{m}(r) = \frac{1}{4\pi} \int_{\Omega} m(\mathbf{x}) d\Omega \quad , \quad (\text{A.3})$$

where r denotes the radius and Ω the unit sphere.

Using 2D GLL quadrature [54] in the unit sphere, the radial average may be determined numerically via GLL quadrature:

$$\overline{m}(r) = \frac{1}{4\pi r^2} \sum_{\alpha,\beta} \omega_{\alpha} \omega_{\beta} m^{\alpha\beta}(r) J^{\alpha\beta}(r) \quad . \quad (\text{A.4})$$

Here α and β denote GLL points in the sphere with radius r , ω_{α} denotes a GLL quadrature weight, and $J^{\alpha\beta}(r)$ is the 2D Jacobian of the mapping to the sphere.

Figure A.1 shows the resulting radial averages of the isotropic shear and compressional wavespeeds for model GLAD-M25 compared to 1D starting model STW105 [63] and PREM [30]. The radial average of GLAD-M25 remains very close to the radial starting model STW105. The main difference between these two models and PREM is the absence of the 220 km discontinuity and a lower V_P/V_S ratio in the top 200 km.

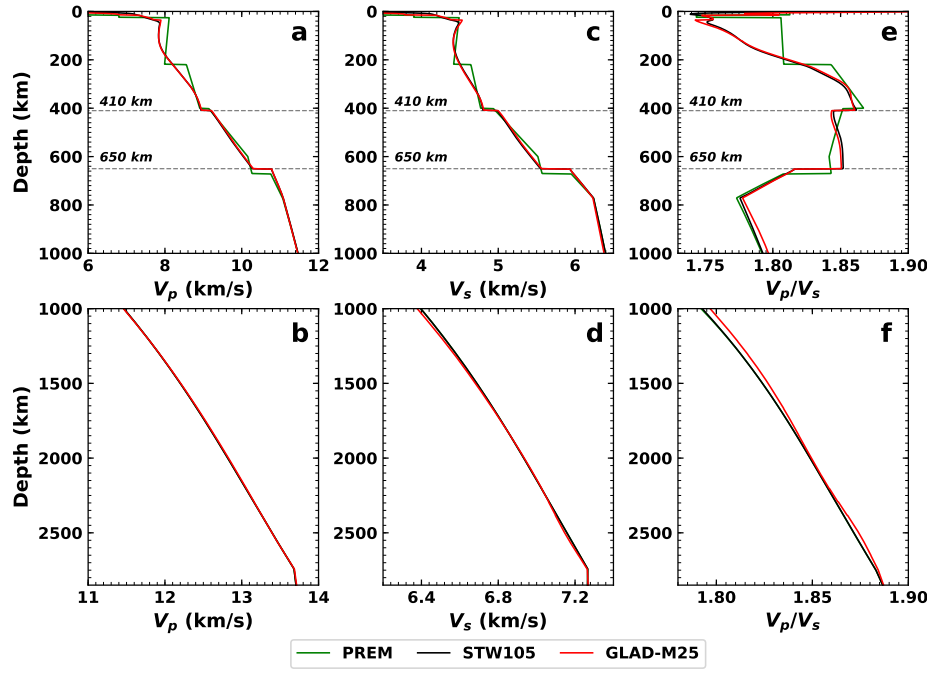


Figure A.1: 1D radial shear and compressional wavespeed profiles for GLAD-M25, STW105, and PREM. The reference frequency for physical dispersion is 7.77 mHz.

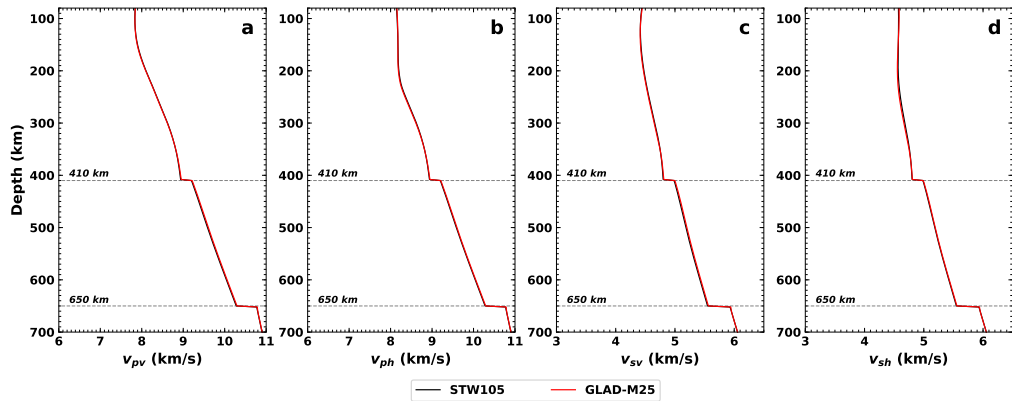


Figure A.2: 1D radial-anisotropic shear and compressional wavespeed profiles for GLAD-M25 and STW105. The reference frequency for physical dispersion is 7.77 mHz.

Appendix B

Spherical harmonic model expansion

In this appendix we express model GLAD-M25 in a spherical harmonic basis to facilitate easy plotting, analysis, and comparisons with other models. The resulting spherical harmonic model should only be used for these purposes, not for numerical simulations, which should always be based on the fully 3D spectral-element mesh.

To accomplish the transformation, we first need to transform the 3D mesh — which includes ellipticity, topography/bathymetry and undulations on internal boundaries — into a spherical volume. After these adjustments, we obtain a spectral element mesh for a perfect sphere, that is, the sort of mesh used for spherically symmetric earth models, such as PREM [30].

In the spherical mesh, the model may be expressed in the form

$$m(\mathbf{x}) = \sum_{\text{elem } \alpha, \beta, \gamma} \sum m^{\alpha\beta\gamma} h_\alpha(\xi) h_\beta(\eta) h_\gamma(\zeta) , \quad (\text{B.1})$$

where h_α denotes a Lagrange polynomial, and where we have used the invertible mapping

$$\mathbf{x} = \mathbf{x}(\xi, \eta, \zeta) \quad (\text{B.2})$$

between spatial points $\mathbf{x} = \{x, y, z\}$ and Gauss-Lobatto-Legendre (GLL) points in the reference element $\{\xi, \eta, \zeta\}$ [54].

Our goal is to expand our spectral-element model in a spherical harmonic basis, i.e.,

$$m(\mathbf{x}) = \sum_{n=0}^N \sum_{\ell=0}^L \sum_{m=-\ell}^{\ell} {}_n C_{\ell m} R_n(r) Y_{\ell m}(\theta, \phi) , \quad (\text{B.3})$$

where r denotes the radius, θ colatitude, and ϕ longitude. We choose a radial basis of the form $R_n(r)$, $n = 0, \dots, N$, e.g., layers or B-splines. These radial basis functions need to be chosen sufficiently dense to mimic the density of the radial spectral element mesh. The radial basis may or may not be orthogonal, i.e.,

$$\int_b^a R_{n'}(r) R_n(r) r^2 dr = A_{n'n} , \quad (\text{B.4})$$

where b denotes the radius of the CMB and a the free surface. The matrix elements $A_{n'n}$ define a positive definite matrix which is invertible. As lateral basis functions we use fully normalized spherical harmonics $Y_{\ell m}(\theta, \phi)$, $\ell = 0, \dots, L$ and $m = -\ell, \dots, \ell$, i.e., [24]

$$\int_0^{2\pi} \int_0^\pi Y_{\ell' m'}^*(\theta, \phi) Y_{\ell m}(\theta, \phi) \sin \theta d\theta d\phi = \delta_{\ell' \ell} \delta_{m' m} , \quad (\text{B.5})$$

where an asterisk denotes complex conjugation. The maximum degree L needs to be chosen to resolve the spectral-element mesh laterally.

To obtain the expansion coefficients ${}_n C_{\ell m}$, we multiply Eqn. (B.3) by $R_{n'}(r) Y_{\ell' m'}^*(\theta, \phi)$ and integrate over the volume of the mantle and crust, V , using Eqns. (B.4 and (B.5)):

$$\int_V m(\mathbf{x}) R_{n'}(r) Y_{\ell' m'}^*(\theta, \phi) d^3 \mathbf{x} = \sum_{n=0}^N {}_n C_{\ell' m'} A_{n'n} , \quad (\text{B.6})$$

We evaluate the integral on the left using GLL quadrature [54]:

$$\sum_{\text{elem}} \sum_{\alpha,\beta,\gamma} \omega_\alpha \omega_\beta \omega_\gamma m^{\alpha\beta\gamma} J^{\alpha\beta\gamma} R_{n'}^{\alpha\beta\gamma} Y_{\ell'm'}^{*\alpha\beta\gamma} = \sum_{n=0}^N {}_n C_{\ell'm'} A_{n'n} . \quad (\text{B.7})$$

Here ω_α denotes a GLL quadrature weight, $J_{\alpha\beta\gamma}$ the Jacobian of the mapping (B.2) evaluated on the GLL points, and $R_{n'}^{\alpha\beta\gamma}$ and $Y_{\ell'm'}^{*\alpha\beta\gamma}$ the values of the radial and spherical harmonic basis functions at a GLL point.

Finally, the desired model coefficients may be obtained —one combination of n , ℓ , and m at a time— via

$${}_n C_{\ell m} = \sum_{n'} A_{nn'}^{-1} \sum_{\text{elem}} \sum_{\alpha,\beta,\gamma} \omega_\alpha \omega_\beta \omega_\gamma m^{\alpha\beta\gamma} J^{\alpha\beta\gamma} R_{n'}^{\alpha\beta\gamma} Y_{\ell m}^{*\alpha\beta\gamma} , \quad (\text{B.8})$$

where A^{-1} denotes the inverse of the $N \times N$ matrix A . Expressions of the form (B.8) are commonplace in spectral-element simulations, and thus easily calculated.

The normalized power per degree ℓ may be calculated via

$$\sigma_\ell^2 = \frac{1}{2\ell+1} \sum_{n'=0}^N \sum_{n=0}^N \sum_{m=-\ell}^{\ell} A_{n'n'n'} C_{\ell m}^* {}_n C_{\ell m} . \quad (\text{B.9})$$

Alternatively, one may wish to calculate the power per degree as a function of radius, which is determined via

$$\Sigma_\ell^2(r) = \frac{1}{2\ell+1} \sum_{n'=0}^N \sum_{n=0}^N \sum_{m=-\ell}^{\ell} R_{n'}(r) R_n(r) {}_{n'} C_{\ell m}^* {}_n C_{\ell m} . \quad (\text{B.10})$$

Instead of the complex spherical harmonic model expansion (B.3), we may wish to use a real spherical harmonic expansion of the form [24]

$$m(\mathbf{x}) = \sum_{n=0}^N \sum_{\ell=0}^L \left[{}_n a_{\ell 0} R_n(r) X_{\ell 0}(\theta) + \sqrt{2} \sum_{m=1}^{\ell} R_n(r) ({}_n a_{\ell m} \cos m\phi + {}_n b_{\ell m} \sin m\phi) X_{\ell m}(\theta) \right] , \quad (\text{B.11})$$

where Eqn. B.30 [24]

$$Y_{\ell m}(\theta, \phi) = X_{\ell m}(\theta) \exp(im\phi) , \quad (\text{B.12})$$

and where

$${}_n a_{\ell 0} = \sum_{n'} A_{nn'}^{-1} \sum_{\text{elem}} \sum_{\alpha, \beta, \gamma} \omega_{\alpha} \omega_{\beta} \omega_{\gamma} m^{\alpha \beta \gamma} J^{\alpha \beta \gamma} R_{n'}^{\alpha \beta \gamma} X_{\ell 0}^{\alpha \beta \gamma} , \quad (\text{B.13})$$

and for $1 \leq m \leq \ell$

$${}_n a_{\ell m} = \sqrt{2} \sum_{n'} A_{nn'}^{-1} \sum_{\text{elem}} \sum_{\alpha, \beta, \gamma} \omega_{\alpha} \omega_{\beta} \omega_{\gamma} m^{\alpha \beta \gamma} J^{\alpha \beta \gamma} R_{n'}^{\alpha \beta \gamma} X_{\ell m}^{\alpha \beta \gamma} (\cos m\phi)^{\alpha \beta \gamma} , \quad (\text{B.14})$$

$${}_n b_{\ell m} = \sqrt{2} \sum_{n'} A_{nn'}^{-1} \sum_{\text{elem}} \sum_{\alpha, \beta, \gamma} \omega_{\alpha} \omega_{\beta} \omega_{\gamma} m^{\alpha \beta \gamma} J^{\alpha \beta \gamma} R_{n'}^{\alpha \beta \gamma} X_{\ell m}^{\alpha \beta \gamma} (\sin m\phi)^{\alpha \beta \gamma} . \quad (\text{B.15})$$

The normalized power per degree ℓ may then be calculated via

$$\sigma_{\ell}^2 = \frac{1}{2\ell + 1} \sum_{n'=0}^N \sum_{n=0}^N A_{n'n} \left[{}_{n'} a_{\ell 0} {}_n a_{\ell 0} + \sum_{m=1}^{\ell} ({}_{n'} a_{\ell m} {}_n a_{\ell m} + {}_{n'} b_{\ell m} {}_n b_{\ell m}) \right] , \quad (\text{B.16})$$

and the normalized power per degree as a function of radius is determined via

$$\Sigma_{\ell}^2(r) = \frac{1}{2\ell + 1} \sum_{n'=0}^N \sum_{n=0}^N R_{n'}(r) R_n(r) \left[{}_{n'} a_{\ell 0} {}_n a_{\ell 0} + \sum_{m=1}^{\ell} ({}_{n'} a_{\ell m} {}_n a_{\ell m} + {}_{n'} b_{\ell m} {}_n b_{\ell m}) \right] . \quad (\text{B.17})$$

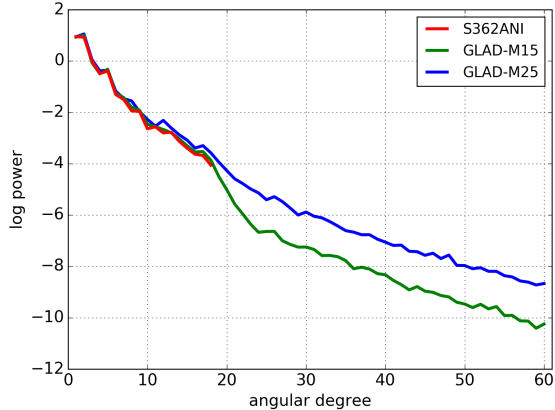


Figure B.1: Normalized power per degree ℓ , based on Eqn. (B.16), for models S362ANI (red), GLAD-M15 (green), and GLAD-M25 (blue). The calculation includes depths greater than 120 km. Model S362ANI has no power beyond degree 18, and model S40RTS has no power beyond degree 40. (Courtesy of Caio Ciardelli.)

In Fig. B.1 we plot the normalized power per degree ℓ for models S362ANI, GLAD-M15, and GLAD-M25, and Fig. 5.24 shows the normalized power per degree as a function of radius for the same set of models.

Bibliography

- [1] K. Aki, A. Christoffersson, and E. S. Husebye. Determination of the three-dimensional seismic structure of the lithosphere. *J. Geophys. Res.*, 82:277–296, 1977.
- [2] Ilkay Altintas, Chad Berkley, Efrat Jaeger, Matthew Jones, Bertram Ludascher, and Steve Mock. Kepler: An extensible system for design and execution of scientific workflows. In *Proceedings of the 16th International Conference on Scientific and Statistical Database Management*, SSDBM ’04, pages 423–, Washington, DC, USA, 2004. IEEE Computer Society.
- [3] Michael Antolik, Yu J. Gu, Göran Ekström, and Adam M. Dziewoński. J362D28: A new joint model of compressional and shear velocity in the Earth’s mantle. *Geophys. J. Roy. Astron. Soc.*, 153(2):443–466, 2003.
- [4] V. Balasubramanian, M. Turilli, W. Huy, M. Lefebvre, W. Lei, G. Cervone, J. Tromp, and S. Jha. Harnessing the power of many: Extensible Toolkit for scalable ensemble applications. 2017. *Int. Parallel and Distributed Processing Symp.*
- [5] A. Bamberger, G. Chavent, and P. Lailly. Une application de la théorie du contrôle à un problème inverse sismique. *Ann. Geophys.*, 33:183–200, 1977.
- [6] C Bassin, G Laske, and G Masters. The current limits of resolution for surface wave tomography in North America. *EOS*, 81, 2000.
- [7] T. W. Becker and L. Boschi. A comparison of tomographic and geodynamic mantle models. *Geochem. Geophy. Geosyst.*, 3(1):1003, 2002.
- [8] M. Beyreuther, R. Barsch, L. Krischer, T. Megies, Y. Behr, and J. Wassermann. ObsPy: A Python toolbox for seismology. *Seism. Res. Lett.*, 81:530–533, 2010.
- [9] Ian Bird, Predrag Buncic, Federico Carminati, Marco Cattaneo, Peter Clarke, Ian Fisk, Maria Girone, John Harvey, Borut Kersevan, Pere Mato, Richard Mount, and Bernd Panzer-Steindel. Update of the Computing Models of the WLCG and the LHC Experiments. Technical Report CERN-LHCC-2014-014 / LCG-TDR-002, CERN, Geneva, 2014.

- [10] P. Bormann. *New Manual of Seismological Observatory Practice (NMSOP-2)*. IASPEI, GFZ German Research Centre for Geosciences, Potsdam, 2012. <http://nmsop.gfz-potsdam.de/>.
- [11] Lapo Boschi and Adam M. Dziewoński. High- and low-resolution images of the Earth's mantle: Implications of different approaches to tomographic modeling. *J. Geophys. Res.*, 104(B11):25567–25594, 1999.
- [12] Ebru Bozdag, Daniel Peter, Matthieu Lefebvre, Dimitri Komatitsch, Jeroen Tromp, Judith Hill, Norbert Podhorszki, and David Pugmire. Global adjoint tomography: first-generation model. *Geophys. J. Int.*, 207(3):1739–1766, 2016.
- [13] E. Bozdag and J. Trampert. On crustal corrections in surface wave tomography. *Geophys. J. Int.*, pages 1066–1082, 2008. doi: 10.1111/j.1365-246X.2007.03690.x.
- [14] Tim Bray, Jean Paoli, C.M. Sperberg-McQueen, Eve Maler, and Franois Yergeau. Extensible Markup Language (XML) 1.0 (Fifth Edition), 2008. accessed 7-October-2015, <https://www.w3.org/TR/2008/REC-xml-20081126/>.
- [15] Scott Callaghan, Ewa Deelman, Dan Gunter, Gideon Juve, Philip Maechling, Christopher Brooks, Karan Vahi, Kevin Milner, Robert Graves, Edward Field, David Okaya, and Thomas Jordan. Scaling up workflow-based applications. *Journal of Computer and System Sciences*, 76(6):428–446, 2010.
- [16] Franck Cappello, Al Geist, Bill Gropp, Laxmikant Kale, Bill Kramer, and Marc Snir. Toward exascale resilience. *International Journal of High Performance Computing Applications*, 23(4):374–388, 2009.
- [17] James A Chalmers and TCR Pulvertaft. Development of the continental margins of the labrador sea: a review. *Geological Society, London, Special Publications*, 187(1):77–105, 2001.
- [18] S. J. Chang, A. M. G. Ferreira, J. Ritsema, H. J. Van Heijst, and J. H. Woodhouse. Global radially anisotropic mantle structure from multiple datasets: A review, current challenges, and outlook. *Tectonophysics*, 617:1–19, 2014.
- [19] G. Chavent. Identification of function parameters in partial differential equations. In *R.E. Goodson and Polis, eds., Identification of parameter distributed systems*. New York, American Society Of Mechanical Engineers 1974, 1974.
- [20] Min Chen, Fenglin Niu, Qinya Liu, Jeroen Tromp, and Xiufen Zheng. Multiparameter adjoint tomography of the crust and upper mantle beneath East Asia: 1. Model construction and comparisons. *J. Geophys. Res.*, 120(3):1762–1786, 2015.
- [21] Y. Chen, J. Hill, W. Lei, M. Lefebvre, J. Tromp, E. Bozdag, and D Komatitsch. Automated time-window selection based on machine learning for full-waveform inversion. *SEG Technical Program Expanded Abstracts*, pages 1,604–1,609, 2017.

- [22] J. Cronsioe, B. Videau, and V. Marangozova-Martin. Boast: Bringing optimization through automatic source-to-source transformations. In *Embedded Multicore SoCs (MCSoC), 2013 IEEE 7th International Symposium on*, pages 129–134, Sept 2013.
- [23] V Curcin and M Ghanem. Scientific workflow systems - can one size fit all? *2008 Cairo Int. Biomed. Eng. Conf.*, pages 1–9, 2008.
- [24] F. A. Dahlen and J. Tromp. *Theoretical Global Seismology*. Princeton U. Press, New Jersey, 1998.
- [25] C. A. Dalton, G. Ekström, and A. M. Dziewoński. The global attenuation structure of the upper mantle. *J. Geophys. Res.*, 113:B05317, 2008.
- [26] Dante. *Divine Comedy (Italian: Divina Commedia)*. 1320.
- [27] Ewa Deelman, Karan Vahi, Gideon Juve, Mats Rynge, Scott Callaghan, Philip J. Maechling, Rajiv Mayani, Weiwei Chen, Rafael Ferreira da Silva, Miron Livny, and Kent Wenger. Pegasus, a workflow management system for science automation. *Future Generation Computer Systems*, 46:17–35, 2015.
- [28] JF Dewey, ML Helman, SD Knott, E Turco, and DHW Hutton. Kinematics of the western mediterranean. *Geological Society, London, Special Publications*, 45(1):265–283, 1989.
- [29] Qiang Du, Vance Faber, and Max Gunzburger. Centroidal voronoi tessellations: Applications and algorithms. *SIAM review*, 41(4):637–676, 1999.
- [30] A. Dziewoński and D. Anderson. Preliminary reference Earth model. *Phys. Earth Planet. Inter.*, 25:297–356, 1981.
- [31] A. M. Dziewoński, B. H. Hager, and R. J. O’Connell. Large-scale heterogeneities in the lower mantle. *J. Geophys. Res.*, 82:239–255, 1977.
- [32] Göran Ekström, Meredith Nettles, and A.M. Dziewoński. The global CMT project 2004–2010: Centroid-moment tensors for 13,017 earthquakes. *Phys. Earth Planet. Inter.*, 200:1–9, 2012.
- [33] A. M. G. Ferreira, J. H. Woodhouse, K. Visser, and J. Trampert. On the robustness of global radially anisotropic surface wave tomography. *J. Geophys. Res.*, 115(B4):1–16, 2010.
- [34] A. Fichtner, B. L. N. Kennett, H. Igel, and H.-P. Bunge. Full seismic waveform tomography for upper-mantle structure in the Australasian region using adjoint methods. *Geophys. J. Int.*, 179:1703–1725, 2009.
- [35] Andreas Fichtner, Hans-Peter Bunge, and Heiner Igel. The adjoint method in seismology I. – Theory. *Physics of the Earth and Planetary Interiors*, 157(1-2):86–104, aug 2006.

- [36] Sergey Fomel and G. Hennenfent. Reproducible Computational Experiments using Scons. In *2007 IEEE International Conference on Acoustics, Speech and Signal Processing - ICASSP '07*, pages 1520–6149, 2007.
- [37] Sergey Fomel, Paul Sava, Ioan Vlad, Yang Liu, and Vladimir Bashkardin. Madagascar: open-source software project for multidimensional data analysis and reproducible computational experiments. *Journal of Open Research Software*, 1(1):e8, 2013.
- [38] Scott W French and Barbara Romanowicz. Broad plumes rooted at the base of the Earth’s mantle beneath major hotspots. *Nature*, 525(7567):95, 2015.
- [39] SW French and BA Romanowicz. Whole-mantle radially anisotropic shear velocity structure from spectral-element waveform tomography. *Geophys. J. Int.*, 199(3):1303–1327, 2014.
- [40] Y. Fukao, M. Obayashi, H. Inoue, and M. Nenbai. Subducting slabs stagnant in the mantle transition zone. *J. Geophys. Res.*, 97:4809–4822, 1992.
- [41] Yoshio Fukao and Masayuki Obayashi. Subducted slabs stagnant above, penetrating through, and trapped below the 660 km discontinuity. *J. Geophys. Res.*, 118(11):5920–5938, 2013.
- [42] Saskia Goes, Wim Spakman, and Harmen Bijwaard. A lower mantle source for central european volcanism. *Science*, 286(5446):1928–1931, 1999.
- [43] S. P. Grand. Mantle shear structure beneath the Americas and surrounding oceans. *J. Geophys. Res.*, 99:11,591–11,621, 1994.
- [44] S. P. Grand and D. V. Helmberger. Upper mantle shear structure of North America. *Geophys. J. Int.*, 76(2):399–438, 1984.
- [45] Stephen P Grand, Rob D Van der Hilst, and Sri Widjiantoro. High resolution global tomography: a snapshot of convection in the earth. *Geological Society of America Today*, 7(4), 1997.
- [46] Robert Graves, Thomas H. Jordan, Scott Callaghan, Ewa Deelman, Edward Field, Gideon Juve, Carl Kesselman, Philip Maechling, Gaurang Mehta, Kevin Milner, David Okaya, Patrick Small, and Karan Vahi. CyberShake: A Physics-Based Seismic Hazard Model for Southern California. *Pure and Applied Geophysics*, 168(3-4):367–381, 2011.
- [47] Yu J Gu, Adam M Dziewoński, Weijia Su, and Göran Ekström. Models of the mantle shear velocity and discontinuities in the pattern of lateral heterogeneities. *J. Geophys. Res.*, 106(B6):11169–11199, 2001.
- [48] J Havskov. *Routine data processing in earthquake seismology with sample data, exercises and software*. Springer, Dordrecht New York, 2010. ISBN: 978-90-481-8696-9.

- [49] George Helffrich, James Wookey, and Ian Bastow. *The Seismic Analysis Code: A Primer and User's Guide*. Cambridge University Press, 1 edition, 11 2013.
- [50] A.B.a.J.v. Hemert. Scientific Workflow: A Survey and Research Directions. *Parallel Processing and Applied Mathematics*, pages 746–753, 2008.
- [51] Vala Hjörleifsdóttir and Göran Ekström. Effects of three-dimensional earth structure on CMT earthquake parameters. *Phys. Earth Planet. Inter.*, 179(3-4):178–190, 2010.
- [52] Mark Howison, Quincey Koziol, David Knaak, John Mainzer, and John Shalf. Tuning HDF5 for Lustre File Systems. In *Proceedings of Workshop on Interfaces and Abstractions for Scientific Data*, 2010.
- [53] IRIS/PASSCAL Data Group. *Introduction to Active Source Data Archiving Utilizing PH5 as the Archive Format*. IRIS/PASSCAL Instrument Center, 2012. Version: 2012336.
- [54] D. Komatitsch and J. Tromp. Introduction to the spectral-element method for 3-D seismic wave propagation. *Geophys. J. Int.*, 139(3):806–822, 1999.
- [55] D. Komatitsch and J. Tromp. Spectral-element simulations of global seismic wave propagation-I. Validation. *Geophys. J. Int.*, 149(2):390–412, 2002.
- [56] D. Komatitsch and J. Tromp. Spectral-element simulations of global seismic wave propagation-II. 3-D models, oceans, rotation, and self-gravitation. *Geophys. J. Int.*, 150(1):303–318, 2002.
- [57] Dimitri Komatitsch, Gordon Erlebacher, Dominik Gddeke, and David Micha. High-order finite-element seismic wave propagation modeling with MPI on a large GPU cluster. *Journal of Computational Physics*, 229(20):7692 – 7714, 2010.
- [58] Dimitri Komatitsch, David Michéa, and Gordon Erlebacher. Porting a high-order finite-element earthquake modeling application to NVIDIA graphics cards using CUDA. *Journal of Parallel and Distributed Computing*, 69(5):451–460, 2009.
- [59] Dimitri Komatitsch, Zhinan Xie, Ebru Bozdağ, Elliott Sales de Andrade, Daniel Peter, Qinya Liu, and Jeroen Tromp. Anelastic sensitivity kernels with parsimonious storage for adjoint tomography and full waveform inversion. *Geophys. J. Int.*, 206(3):1467–1478, 2016.
- [60] Lion Krischer and Emanuele Casarotti. Pyflex: 0.1.4, September 2015.
- [61] Lion Krischer, James Smith, Wenjie Lei, Matthieu Lefebvre, Youyi Ruan, Elliott Sales de Andrade, Norbert Podhorszki, Ebru Bozdağ, and Jeroen Tromp. An adaptable seismic data format. *Geophys. J. Int.*, 207(2):1003–1011, 2016.

- [62] B. Kustowski, G. Ekström, and A. M. Dziewoński. Anisotropic shear-wave velocity structure of the Earth's mantle: A global model. *J. Geophys. Res.*, 113:B06306, doi:10.1029/2007JB005169, 2008.
- [63] B Kustowski, G Ekström, and AM Dziewoński. Anisotropic shear-wave velocity structure of the Earth's mantle: A global model. *J. Geophys. Res.*, 113(B6), 2008.
- [64] P. Lailly. The seismic inverse problem as a sequence of before stack migration. In *J. Bednar, ed., Conference on Inverse Scattering: Theory and Application*, pages 206–220. Society for Industrial and Applied Mathematics, 1983.
- [65] Sergei Lebedev and Guust Nolet. Upper mantle beneath southeast asia from s velocity tomography. *J. Geophys. Res.*, 108(B1), 2003.
- [66] M. Lefebvre, Y. Chen, W. Lei, D. Luet, Y. Ruan, E. Bozdağ, J. Hill, D. Komatitsch, L. Krisher, D. Peter, N. Podhorszki, J. Smith, and J. Tromp. Data and workflow management for exascale global adjoint tomography. In T.P. Straatsma, K.B. Antypas, and T.J. Williams, editors, *Exascale Scientific Applications — Scalability and Performance Portability*. CRC Press, 2018.
- [67] Wenjie Lei, Youyi Ruan, Ebru Bozdağ, Daniel Peter, Matthieu Lefebvre, Dimitri Komatitsch, Jeroen Tromp, Judith Hill, Norbert Podhorszki, and David Pugmire. Global adjoint tomography – Model GLAD-M25. *Geophys. J. Int.*, submitted, 2019.
- [68] Jianwei Li, Michael Zingale, Wei-keng Liao, Alok Choudhary, Robert Ross, Rajeev Thakur, William Gropp, Rob Latham, Andrew Siegel, and Brad Gallagher. Parallel netCDF: A High-Performance Scientific I/O Interface. In *Proceedings of the 2003 ACM/IEEE conference on Supercomputing - SC '03*, page 39, New York, New York, USA, November 2003. ACM Press.
- [69] Xiang-Dong Li and Barbara Romanowicz. Global mantle shear velocity model developed using nonlinear asymptotic coupling theory. *J. Geophys. Res.*, 101(B10):22245–22272, 1996.
- [70] Qing Liu, Jeremy Logan, Yuan Tian, Hasan Abbasi, Norbert Podhorszki, Jong Youl Choi, Scott Klasky, Roselyne Tchoua, Jay Lofstead, Ron Oldfield, et al. Hello ADIOS: the challenges and lessons of developing leadership class I/O frameworks. *Concurrency and Computation: Practice and Experience*, 26(7):1453–1473, 2014.
- [71] Qing Liu, Jeremy Logan, Yuan Tian, Hasan Abbasi, Norbert Podhorszki, Jong Youl Choi, Scott Klasky, Roselyne Tchoua, Jay Lofstead, Ron Oldfield, Manish Parashar, Nagiza Samatova, Karsten Schwan, Arie Shoshani, Matthew Wolf, Kesheng Wu, and Weikuan Yu. Hello ADIOS: the challenges and lessons of developing leadership class I/O frameworks. *Concurrency and Computation: Practice and Experience*, August 2013.

- [72] Qinya Liu, Jascha Polet, Dimitri Komatitsch, and Jeroen Tromp. Spectral-element moment tensor inversions for earthquakes in southern California. *Bull. Seism. Soc. Am.*, 94(5):1748–1761, 2004.
- [73] A. E. H. Love. *A Treatise on the Mathematical Theory of Elasticity*. Cambridge U. Press, Cambridge, 4 edition, 1927.
- [74] C. Lu and S.P. Grand. The effect of subducting slabs in global shear wave tomography. *Geophys. J. Int.*, 205:1,074–1,085, 2016.
- [75] A Luckow, P Mantha, and S Jha. Pilot-Abstraction: A Valid Abstraction for Data-Intensive Applications on HPC, Hadoop and Cloud Infrastructures? *arXiv preprint arXiv:1501.05041*, 2015.
- [76] Bertram Ludascher, Mathias Weske, Timothy McPhillips, and Shawn Bowers. Scientific Workflows: Business as Usual? *Business Process Management*, 5701:31–47, 2009.
- [77] Y Luo, J Tromp, B Denel, and H Calandra. 3D coupled acoustic-elastic migration with topography and bathymetry based on spectral-element and adjoint methods. *GEOPHYSICS*, 78(4):S193–S202, 2013.
- [78] Yang Luo, Ryan Modrak, and Jeroen Tromp. Strategies in adjoint tomography. *Handbook of Geomathematics*, pages 1–52, 2013.
- [79] Alessia Maggi, Carl Tape, Min Chen, Daniel Chao, and Jeroen Tromp. An automated time-window selection algorithm for seismic tomography. *Geophys. J. Int.*, 178(1):257–281, 2009.
- [80] Guy Masters, Stuart Johnson, Gabi Laske, Harold Bolton, and J. H. Davies. A shear-velocity model of the mantle. *Philosophical Transactions of the Royal Society of London A: Mathematical, Physical and Engineering Sciences*, 354(1711):1385–1411, 1996.
- [81] Thomas Guy Masters, Stuart Johnson, Gabi Laske, and Harold Bolton. A shear-velocity model of the mantle. *Phil. Trans. R. Soc. Lond. A*, 354(1711):1385–1411, 1996.
- [82] Incorporated Research Institutions for Seismology (IRIS). *SEED Reference Manual - Standard for the Exchange of Earthquake Data*, August 2012. https://www.fdsn.org/seed_manual/SEEDManual_V2.4.pdf.
- [83] Daniel E McNamara and Raymond P Buland. Ambient Noise Levels in the Continental United States. *Bulletin of the Seismological Society of America*, 94(4):1517–1527, 2004.
- [84] Tobias Megies, Moritz Beyreuther, Robert Barsch, Lion Krischer, and Joachim Wassermann. ObsPy – What can it do for data centers and observatories? *Annals Of Geophysics*, 54(1):47–58, 2011.

- [85] Charles Mégnin and Barbara Romanowicz. The three-dimensional shear velocity structure of the mantle from the inversion of body, surface and higher-mode waveforms. *Geophys. J. Int.*, 143(3):709–728, 2000.
- [86] Ryan Modrak and Jeroen Tromp. Seismic waveform inversion best practices: regional, global and exploration test cases. *Geophys. J. Int.*, 206(3):1864–1889, 2016.
- [87] Ryan T. Modrak, Dmitry Borisov, Matthieu Lefebvre, and Jeroen Tromp. Seisflows – flexible waveform inversion software. *Computers & Geosciences*, 115:88 – 95, 2018.
- [88] Jean-Paul Montagner and Don L Anderson. Petrological constraints on seismic anisotropy. *Phys. Earth Planet. Inter.*, 54(1-2):82–105, 1989.
- [89] Jean-Paul Montagner and T. Tanimoto. Global upper mantle tomography of seismic velocities and anisotropies. *J. Geophys. Res.*, 96(B12):20,337–20,351, 1991.
- [90] Raffaella Montelli, Guust Nolet, FA Dahlen, and G Masters. A catalogue of deep mantle plumes: New results from finite-frequency tomography. *Geochem. Geophy. Geosyst.*, 7(11), 2006.
- [91] P Moulik and G Ekström. An anisotropic shear velocity model of the Earth’s mantle using normal modes, body waves, surface waves and long-period waveforms. *Geophys. J. Int.*, 199(3):1713–1738, 2014.
- [92] P. Moulik and G. Ekström. The relationships between large-scale variations in shear velocity, density, and compressional velocity in the Earth’s mantle. *J. Geophys. Res.*, 121(4):2737–2771, 2016.
- [93] MPI Forum. Message Passing Interface (MPI) Forum Home Page. <http://www mpi-forum.org/>, 12 2009.
- [94] R Dietmar Müller, Maria Sdrolias, Carmen Gaina, and Walter R Roest. Age, spreading rates, and spreading asymmetry of the world’s ocean crust. *Geochemistry, Geophysics, Geosystems*, 9(4), 2008.
- [95] H.-C. Nataf, I. Nakanishi, and D. L. Anderson. Anisotropy and shear velocity heterogeneities in the upper mantle. *Geophys. Res. Lett.*, 11:109–112, 1984.
- [96] J. Nieplocha, I. Foster, and R. A. Kendall. ChemIo: High Performance Parallel I/o for Computational Chemistry Applications. *International Journal of High Performance Computing Applications*, 12(3):345–363, September 1998.
- [97] J Nocedal. Updating Quasi-Newton Matrices with Limited Storage. *Mathematics of Computation*, 35(151):773–782, 1980.

- [98] G. Nolet, Y. Hello, S. Van der Lee, S. Bonnieux, M. C. Ruiz, N. A. Pazmino, A. Deschamps, M. M. Regnier, Y. Font, Y. J. Chen, and F. J. Simons. Imaging the Galápagos mantle plume with an unconventional application of floating seismometers. *Scientific Reports*, 9:1326, 2019.
- [99] Ridvan Örsvuran, Ebru Bozdağ, Ryan Modrak, Wenjie Lei, and Youyi Ruan. Towards double-difference global adjoint tomography. *Geophys. J. Int.*, 2019. submitted.
- [100] M. P. Panning, V. Lekić, and B. Romanowicz. Importance of crustal corrections in the development of a new global model of radial anisotropy. *J. Geophys. Res.*, 115:B12325, 2010.
- [101] Daniel Peter, Dimitri Komatitsch, Yang Luo, Roland Martin, Nicolas Le Goff, Emanuele Casarotti, Pieyre Le Loher, Federica Magnoni, Qinya Liu, Céline Blitz, Tarje Nissen-Meyer, Piero Basini, and Jeroen Tromp. Forward and adjoint simulations of seismic wave propagation on fully unstructured hexahedral meshes. *Geophysical Journal International*, 186(2):721–739, August 2011.
- [102] Daniel Peter, Dimitri Komatitsch, Yang Luo, Roland Martin, Nicolas Le Goff, Emanuele Casarotti, Pieyre Le Loher, Federica Magnoni, Qinya Liu, Céline Blitz, Tarje Nissen-Meyer, Piero Basini, and Jeroen Tromp. Forward and adjoint simulations of seismic wave propagation on fully unstructured hexahedral meshes. *Geophys. J. Int.*, 186(2):721–739, 2011.
- [103] R. E. Plessix. A review of the adjoint-state method for computing the gradient of a functional with geophysical applications. *Geophys. J. Int.*, 167(2):495–503, 2006.
- [104] F. J. L. Reid, J. H. Woodhouse, and H. J. Van Heijst. Upper mantle attenuation and velocity structure from measurements of differential s phases. *Geophys. J. Int.*, 145:615–630, 2001.
- [105] R. Rew and G. Davis. NetCDF: an interface for scientific data access. *Computer Graphics and Applications, IEEE*, 10(4):76–82, July 1990.
- [106] Max Rietmann, Peter Messmer, Tarje Nissen-Meyer, Daniel Peter, Piero Basini, Dimitri Komatitsch, Olaf Schenk, Jeroen Tromp, Lapo Boschi, and Domenico Giardini. Forward and adjoint simulations of seismic wave propagation on emerging large-scale GPU architectures. In *Proceedings of the International Conference on High Performance Computing, Networking, Storage and Analysis*, SC ’12, pages 38:1—38:11, Los Alamitos, CA, USA, 2012. IEEE Computer Society Press.
- [107] A.E. Ringwood and T. Irifune. Subducting slabs stagnant in the mantle transition zone. *Nature*, 331:131–136, 1988.

- [108] J Ritsema, A. Deuss, H.J. Van Heijst, and J.H. Woodhouse. S40RTS: a degree-40 shear-velocity model for the mantle from new Rayleigh wave dispersion, teleseismic traveltimes and normal-mode splitting function measurements. *Geophys. J. Int.*, 184(3):1223–1236, 2011.
- [109] M. H. Ritzwoller and E. M. Lavelle. Three-dimensional models of the Earth’s mantle. *Reviews of Geophysics*, 33:1–66, 1995.
- [110] B. Romanowicz. Attenuation tomography of the Earth’s mantle: a review of current status. *Pure Appl. Geophys.*, 153:257–272, 1998.
- [111] Youyi Ruan, Wenjie Lei, Ryan Modrak, Ridvan Örsşur, Ebru Bozdağ, and Jeroen Tromp. Balancing unevenly distributed data in seismic tomography: A global adjoint tomography example. *Geophys. J. Int.*, 2019. Submitted.
- [112] A. J. Schaeffer and S. Lebedev. Global shear speed structure of the upper mantle and transition zone. *Geophys. J. Int.*, 194:417–449, 2013.
- [113] AJ Schaeffer and S Lebedev. Imaging the North American continent using waveform inversion of global and USAArray data. *Earth Planet. Sci. Lett.*, 402:26–41, 2014.
- [114] Erich Schikuta and Helmut Vanek. Parallel I/O. *International Journal of High Performance Computing Applications*, 15(2):162–168, May 2001.
- [115] Danijel Schorlemmer, Fabian Euchner, Philipp Kästli, Joachim Saul, and QuakeML Working Group. QuakeML: Status of the XML-based seismological data exchange format. *Annals of Geophysics*, 54(1):59–65, 2011.
- [116] Danijel Schorlemmer, Adrian Wyss, Silvio Maraini, Stefan Wiemer, and Manfred Baer. Orfeus Newsletter 6(2): QuakeML - An XML schema for seismology, 2004. accessed 7-October-2015, <http://www.orfeus-eu.org/organization/Organization/Newsletter/vol6no2/quakeml.shtml>.
- [117] SEG Technical Standards Committee. *SEG Y rev 1 Data Exchange format*. Society of Exploration Geophysicists, 2002.
- [118] M. Sengupta and N. Toksöz. Three-dimensional model of seismic velocity variation in the Earth’s mantle. *Geophys. Res. Lett.*, 3:84–86, 1977.
- [119] Nathan A Simmons, Steve C Myers, Gardar Johannesson, and Eric Matzel. LLNL-G3Dv3: Global P wave tomography model for improved regional and teleseismic travel time prediction. *J. Geophys. Res.*, 117(B10), 2012.
- [120] Zachary D. Stephens, Skylar Y. Lee, Faraz Faghri, Roy H. Campbell, Chengxiang Zhai, Miles J. Efron, Ravishankar Iyer, Michael C. Schatz, Saurabh Sinha, and Gene E. Robinson. Big data: Astronomical or genomic? *PLoS Biol*, 13(7):e1002195, 07 2015.

- [121] Carl Tape, Qinya Liu, Alessia Maggi, and Jeroen Tromp. Adjoint tomography of the southern California crust. *Science*, 325(5943):988–992, 2009.
- [122] Carl Tape, Qinya Liu, Alessia Maggi, and Jeroen Tromp. Seismic tomography of the southern California crust based on spectral-element and adjoint methods. *Geophysical Journal International*, 180(1):433–462, jan 2010.
- [123] A. Tarantola. Inversion of seismic reflection data in the acoustic approximation. *Geophysics*, 49:1259–1266, 1984.
- [124] Ian Taylor, Matthew Shields, Ian Wang, and Andrew Harrison. *The Triana Workflow Environment: Architecture and Applications*, pages 320–339. Springer London, London, 2007.
- [125] Douglas Thain, Todd Tannenbaum, and Miron Livny. Distributed computing in practice: the condor experience. *Concurrency - Practice and Experience*, 17(2-4):323–356, 2005.
- [126] R. Thakur, W. Gropp, and E. Lusk. An abstract-device interface for implementing portable parallel-I/O interfaces. *Proceedings of 6th Symposium on the Frontiers of Massively Parallel Computation (Frontiers '96)*, 1996.
- [127] R. Thakur, W. Gropp, and E. Lusk. Data sieving and collective I/O in ROMIO. *Proceedings. Frontiers '99. Seventh Symposium on the Frontiers of Massively Parallel Computation*, 1999.
- [128] The HDF Group. Hierarchical Data Format, version 5, 1997–2015. <https://www.hdfgroup.org/HDF5/>.
- [129] Sivan Toledo and Fred G Gustavson. The Design and Implementation of SOLAR, a Portable Library for Scalable Out-of-Core Linear Algebra Computations. In *Workshop on I/O in Parallel and Distributed Systems*, pages 28–40. ACM, 1996.
- [130] J. Trampert and J. H. Woodhouse. Assessment of global phase velocity models. *Geophys. J. Int.*, 144:165–174, 2001.
- [131] Jeannot Trampert and John H. Woodhouse. Global anisotropic phase velocity maps for fundamental mode surface waves between 40 and 150 s. *Geophys. J. Int.*, 154(1):154–165, 2003.
- [132] J. Tromp and F. A. Dahlen. Variational principles for surface wave propagation on a laterally heterogeneous Earth—I. Time-domain JWKB theory. *Geophys. J. Int.*, 109:581–598, 1992.
- [133] J. Tromp and F. A. Dahlen. Variational principles for surface wave propagation on a laterally heterogeneous Earth—II. Frequency-domain JWKB theory. *Geophys. J. Int.*, 109:599–619, 1992.

- [134] J. Tromp, D. Komatitsch, V. Hjörleifsdóttir, Q. Liu, H. Zhu, D. Peter, E. Bozdağ, D. McRitchie, P. Friberg, C. Trabant, and A. Hutko. Near real-time simulations of global CMT earthquakes. *Geophys. J. Int.*, 183:381–389, 2010.
- [135] J. Tromp, C. Tape, and Q. Y. Liu. Seismic tomography, adjoint methods, time reversal and banana-doughnut kernels. *Geophys. J. Int.*, 160:195–216, 2005.
- [136] Seiji Tsuboi, Kazuto Ando, Takayuki Miyoshi, Daniel Peter, Dimitri Komatitsch, and Jeroen Tromp. A 1.8 trillion degrees-of-freedom, 1.24 petaflops global seismic wave simulation on the k computer. *International Journal of High Performance Computing Applications*, 2016.
- [137] Matteo Turilli, Mark Santcroos, and Shantenu Jha. A Comprehensive Perspective on Pilot-Jobs, 2016.
- [138] Andrew P. Valentine and John H. Woodhouse. Reducing errors in seismic tomography: combined inversion for sources and structure. *Geophys. J. Int.*, 180:847–857, 2010.
- [139] Douwe G. Van der Meer, Douwe J.J. Van Hinsbergen, and Wim Spakman. Atlas of the underworld: Slab remnants in the mantle, their sinking history, and a new outlook on lower mantle viscosity. *Tectonophysics*, 723:309–448, 2018.
- [140] Jules Vernes. *The Journey to the Center of the Earth (French: Voyage au centre de la Terre)*. Pierre-Jules Hetzel, 1864.
- [141] M. Vilayannur, S. Lang, R. Ross, R. Klundt, and L. Ward. Extending the POSIX I/O Interface: A Parallel File System Perspective. Technical report, Argonne National Laboratory, 2008.
- [142] Steven J Whitmeyer and Karl E Karlstrom. Tectonic model for the proterozoic growth of north america. *Geosphere*, 3(4):220–259, 2007.
- [143] Michael Wilde, Ian Foster, Kamil Iskra, Pete Beckman, Zhao Zhang, Allan Espinosa, Mihael Hategan, Ben Clifford, and Ioan Raicu. Parallel Scripting for Applications at the Petascale and Beyond. *Computer*, 42(11):50–60, 2009.
- [144] Katherine Wolstencroft, Robert Haines, Donal Fellows, Alan Williams, David Withers, Stuart Owen, Stian Soiland-Reyes, Ian Dunlop, Aleksandra Nenadic, Paul Fisher, Jiten Bhagat, Khalid Belhajjame, Finn Bacall, Alex Hardisty, Abraham Nieva de la Hidalga, Maria P. Balcazar Vargas, Shoaib Sufi, and Carole Goble. The Taverna workflow suite: designing and executing workflows of Web Services on the desktop, web or in the cloud. *Nucleic Acids Research*, 41(Web Server issue):gkt328–W561, May 2013.
- [145] J. H. Woodhouse and A. M. Dziewoński. Mapping the upper mantle: Three-dimensional modeling of Earth structure by inversion of seismic waveforms. *J. Geophys. Res.*, 89:5953–5986, 1984.

- [146] J. H. Woodhouse and Y. K. Wong. Amplitude, phase and path anomalies of mantle waves. *Geophys. J. R. Astron. Soc.*, 87:753–773, 1986.
- [147] MJR Wortel and Wim Spakman. Subduction and slab detachment in the mediterranean-carpathian region. *Science*, 290(5498):1910–1917, 2000.
- [148] Stephen Wright and Jorge Nocedal. Numerical optimization. *Springer Science*, 35(67-68):7, 1999.
- [149] An Yin and T Mark Harrison. Geologic evolution of the himalayan-tibetan orogen. *Annual Review of Earth and Planetary Sciences*, 28(1):211–280, 2000.
- [150] Jia Yu and Rajkumar Buyya. A taxonomy of scientific workflow systems for grid computing. *ACM SIGMOD Record*, pages 44–49, 2005.
- [151] H. Zhu, E. Bozdağ, T. Duffy, and J. Tromp. Seismic attenuation beneath Europe and the North Atlantic: Implications for water in the mantle. *Earth and Planetary Science Letters*, 381:1–11, 2013.
- [152] H. Zhu and J. Tromp. Mapping tectonic deformation in the crust and upper mantle beneath Europe and the North Atlantic Ocean. *Science*, 341:871–875, 2013.
- [153] Hejun Zhu, Ebru Bozdağ, Daniel Peter, and Jeroen Tromp. Structure of the European upper mantle revealed by adjoint tomography. *Nature Geoscience*, 5(7):493, 2012.
- [154] Hejun Zhu, Ebru Bozdağ, and Jeroen Tromp. Seismic structure of the European upper mantle based on adjoint tomography. *Geophys. J. Int.*, 201(1):18–52, 2015.
- [155] Hejun Zhu, Dimitri Komatitsch, and Jeroen Tromp. Radial anisotropy of the North American upper mantle based on adjoint tomography with USArray. *Geophys. J. Int.*, 211(1):349–377, 2017.
- [156] Hejun Zhu, Yang Luo, Tarje Nissen-Meyer, Christina Morency, and Jeroen Tromp. Elastic imaging and time-lapse migration based on adjoint methods. *Geophysics*, 74(6):WCA167, 2009.
- [157] Peter A Ziegler. European cenozoic rift system. *Tectonophysics*, 208(1-3):91–111, 1992.
- [158] Alet Zielhuis and Guust Nolet. Deep seismic expression of an ancient plate boundary in europe. *Science*, 265(5168):79–81, 1994.